Doctoral Dissertation
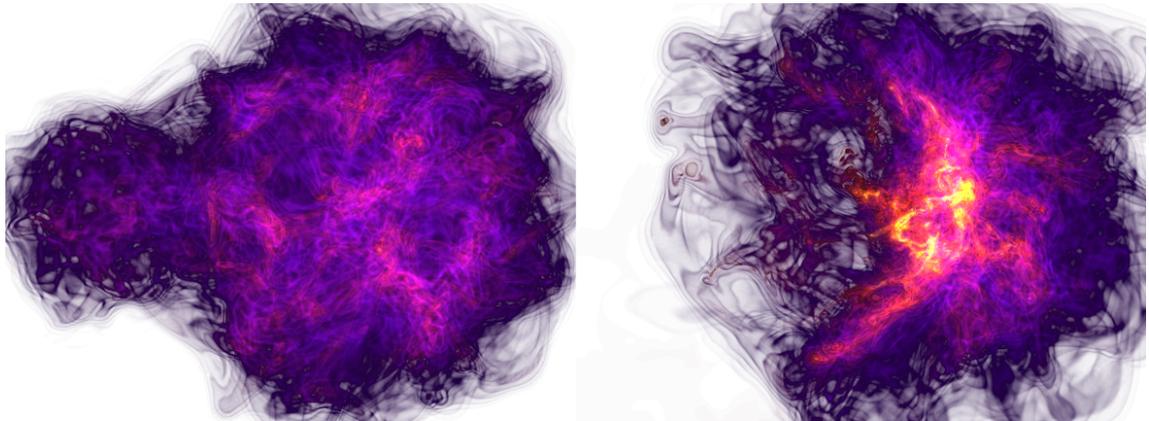
**Massive core/star formation triggered by cloud-cloud collision:
Effects of magnetic fields and collision speeds
(分子雲衝突によって引き起こされる大質量コアおよび大質量星形成:
磁場と衝突速度の影響)**

Nirmit Deepak Sakre

Graduate School of Science, Hokkaido University
Department of Cosmosciences

March, 2022

ii

Abstract

Massive stars are important in astrophysics, since they strongly impact the inter-stellar medium and evolution of galaxies. Despite their importance, their formation process is not well understood. Cloud-cloud collision is proposed as a strong candidate for massive star formation. We study the effects of magnetic fields and collision speeds on massive star formation triggered by cloud-cloud collision. We describe our study in two parts as follows.

In the first part, we study the effects of magnetic fields by performing magnetohydrodynamic simulations with sub-parsec resolution (0.015 pc) that can resolve the molecular cores. Initial clouds with the typical gas density of the molecular clouds are immersed in various uniform magnetic fields of three different directions, parallel, perpendicular, and oblique to collision axis. The turbulent magnetic fields are generated in the clouds by the internal turbulent gas motion before the collision to be consistent with the observation by Crutcher et al. (2010), if the uniform magnetic field strength is 4.0 µG. The collision speed of 10 km s^{-1} is adopted, which is much larger than the sound speeds and the Alfvén speeds of gas in the clouds. We identify gas clumps with gas densities greater than 5×10^{-20} g cm^{-3} as the dense cores and trace them throughout the simulations to investigate their mass evolution. We analyze their gravitational boundness for judging massive star formation. We show that a greater number of massive cores greater than 10 $M_\odot$ and massive, gravitationally bound cores are mostly formed in the strong magnetic field (4.0 µG) models than the weak magnetic field (0.1 µG) models and isolated, non-colliding cloud models. This is partly because the strong magnetic field suppresses the spatial shifts of the shocked layer that can be caused by the nonlinear thin shell instability in no magnetic field case. The spatial shifts promote the formation of low-mass dense cores in the weak magnetic field models. The numerical results of massive core formation in the strong magnetic field models with various magnetic field directions show that the magnetic field direction is not so important for the massive core numbers, although detailed structures of shocked gas region and spatial distribution of dense cores depend on the magnetic field direction. We discuss the implications of our numerical results on massive star formation.

In the second part, we study the effects of collision speeds on massive core formation. We assume two combinations of colliding clouds, Small (7 pc) and Medium (14 pc) clouds, and Small and Large (20 pc) clouds, and collision speeds in the range between 10 and 40 km s^{-1}. The clouds are initially immersed in a uniform magnetic field of 4.0 µG, and turbulence is generated in them, as in the first part. In the collision of Small and Medium clouds with 20 km s^{-1}, massive bound cores are hard to form than the 10 km s^{-1} case. In the collision of Small and Large clouds, a greater number of massive bound cores form than that in Small and Medium clouds with 20 km s^{-1}. These results indicate that longer duration of the collision in this model than that in Small and Medium clouds can explain

such massive bound core formation by mass growth due to gas accretion to the dense cores. In the same colliding clouds with higher collision speeds, 30 and 40 km s^{-1}, massive bound core formation is more suppressed with increasing collision speed. Our numerical results show that the collision speed controls massive dense core formation and an upper limit of collision speed for massive bound core formation exists. This upper limit increases with sizes of colliding clouds. We discuss a relation between collision speed and column density of magnetized, colliding clouds for massive bound core formation and the observed relation by Enokiya, Torii, and Fukui (2021) about the collision speeds and number of massive stars in observed colliding clouds.

Finally, we discuss future works based on this study.

Acknowledgements

Contents

viii

Chapter 1

Introduction

Massive stars are highly important for the evolution of our universe. However, their formation process is not well understood. Cloud-cloud collision, i.e., a supersonic collision of molecular clouds, is a strong candidate for massive star formation. This thesis focuses on this scenario, and we study the effects of magnetic fields and collision speeds on massive star formation triggered by cloud-cloud collision.

The outline of this chapter is as follows. We first address star formation process, specifically describing our lack of understanding of massive star formation and possible scenarios for massive star formation in Section 1.1. We then introduce cloud-cloud collision, which is one of the strong candidates of massive star formation in Section 1.2. In Section 1.3, we review current understanding of effects of magnetic fields and collision speeds on massive star formation triggered by cloud-cloud collision. Finally, in Sections 1.4 and 1.5, we mention the aim and outline of this thesis, respectively.

1.1 Current theory of star formation

1.1.1 Molecular clouds

Stars form in dense regions (also called molecular cores) of molecular clouds in interstellar medium (ISM). The ISM is composed of gas and dust. The gas in the ISM exists in various characteristic phases, depending on ionization and chemical state of hydrogen. The density of the ISM varies from 10^{-4} atoms cm^{-3} in hot ionised medium to 10^6 atoms cm^{-3} in dense regions within molecular clouds with temperatures ranging from 10^7 K in hot ionised medium to 10 K in molecular clouds.

The molecular clouds primarily consist of molecular hydrogen. Their typical temperature is 10 K, and the number density is 10^2 hydrogen molecules cm^{-3}. Molecular clouds gravitationally collapse to form stars. Magnetic fields and turbulence are present in molecular clouds, which can resist this collapse. Next, we describe the dynamical importance of magnetic fields and turbulence in molecular clouds. Then, in Section 1.1.2, we describe the interplay between self-gravity,

magnetic fields, and turbulence for gravitational collapse of molecular clouds, which lead to formation of stars.

Magnetic field

There is evidence that magnetic fields are dynamically important in molecular clouds. Crutcher et al. (2010) surveyed Zeeman measurements of HI regions and molecular clouds and found that a relation exists between maximum line-of-sight magnetic field strength, B_{upper} and hydrogen number density, n_H, given as,

$$B_{upper} = \begin{cases} 10\ \mu G \left(\frac{n_H}{300\ cm^{-3}} \right)^{2/3}, & \text{for } n_H > 300\ cm^{-3} \\ 10\ \mu G, & \text{for } n_H < 300\ cm^{-3}. \end{cases} \quad (1.1)$$

For magnetized clouds with negligible thermal pressure support, Tomisaka (1998) calculated critical mass, M_Φ, above which magnetic field cannot prevent gravitational collapse, given by

$$M_\Phi = 0.012 \frac{\Phi_B}{\sqrt{G}}, \quad (1.2)$$

where Φ_B is magnetic field flux passing through the cloud. For typical molecular clouds, it has been pointed out that magnetic forces can have a significant influence. Due to the strong coupling of ions with neutral gas on a molecular cloud scale, the magnetic forces allow gas flow along the magnetic field than across it and can lead to highly anisotropic turbulence patterns. At smaller scales less than ~ 0.05 pc, this coupling becomes weaker and can allow gas flow across magnetic field, also called ambipolar diffusion.

Turbulence

Turbulence is created by the instability of laminar flows that develop as soon as the inertial forces greatly exceed the viscous forces. This instability leads to velocity dispersion at various scales in ISM. The power spectrum of velocity dispersion is similar to Kolmonogov's spectrum. Larson (1981) found that typically velocity dispersion varies with the size of molecular clouds as

$$\sigma\ (km\ s^{-1}) = 1.1L\ (pc)^{0.38}, \quad (1.3)$$

where σ is velocity dispersion of molecular gas, and L is the size of the cloud. The velocity dispersion of a typical molecular cloud of few to tens of parsecs and 10 K temperature is significantly greater than its isothermal sound speed. This supersonic velocity dispersion can generate turbulent density structures in molecular clouds. More specifically, past studies have highlighted that log normal probability density function is created by this supersonic turbulence (e.g.,

Vazquez-Semadeni ([1994]) and Passot and Vázquez-Semadeni ([1998])). Such lognormal profile of density has significant implications on initial mass function (IMF). Some studies have pointed out that IMF is a direct consequence of turbulence (e.g., Padoan and Nordlund ([2002])).

1.1.2 Gravitational collapse

Self-gravity is a major reason for the collapse of the molecular clouds. We show the method to evaluate the importance of self-gravity, turbulence, and magnetic field for collapse. This is done using a powerful and general theorem about the behavior of the fluid, known as a virial theorem. The double time derivative of moment of Inertia $\ddot{I}$ gives the virial theorem (McKee and Zweibel, [1992]) as

$$\frac{1}{2}\ddot{I} = 2\left(\mathcal{T} - \mathcal{T}_S\right) + \mathcal{B} + \mathcal{W} - \frac{1}{2}\frac{d}{dt}\int_S \left(\rho\mathbf{v}r^2\right)\cdot d\mathbf{S}, \tag{1.4}$$

where

$$\mathcal{T} = \int_V \left(\frac{1}{2}\rho v^2 + \frac{3}{2}P\right)dV, \tag{1.5}$$

$$\mathcal{T}_S = \int_S \mathbf{r}\cdot\Pi\cdot d\mathbf{S}, \tag{1.6}$$

$$\mathcal{B} = \frac{1}{8\pi}\int_V B^2 dV + \int_S \mathbf{r}\cdot\mathbf{T}_M\cdot d\mathbf{S}, \text{ and} \tag{1.7}$$

$$\mathcal{W} = -\int_V \rho\mathbf{r}\cdot\nabla\phi dV. \tag{1.8}$$

$\mathcal{T}$ is the total kinetic and thermal energies of the cloud. $\mathcal{T}_S$ is the pressure on the cloud surface, which includes the thermal pressure and the ram pressure of gas flowing across the cloud surface. $\mathcal{B}$ is the difference between the magnetic pressure in the cloud interior and the magnetic pressure and tension at the cloud surface. The magnetic pressure in interior supports the cloud, whereas the magnetic pressure and tension at the cloud surface confines the cloud. $\mathcal{W}$ is the gravitational energy of the cloud. The last term in the right-hand side shows the rate of change of the momentum flux across the cloud surface. For a cloud of fixed shape, $\ddot{I}$ shows the rate of change of the cloud's expansion or contraction. Negative $\ddot{I}$ implies that the terms that help contraction of cloud (the magnetic pressure and tension at the surface and surface pressure, and gravity) are larger, and the cloud begins to shrink. Positive $\ddot{I}$ implies that the terms that help expansion (ram pressure, thermal pressure, magnetic pressure and ram pressure) are larger, and the cloud begins to expand.

In simulations, gravitational boundness is used to judge gravitational stability of gas regions. This is done by simply comparing gravitational (E_{grav}) with thermal (E_{ther}), turbulent (E_{turb}), and magnetic field energies (E_{mag}). E_{grav} helps contraction, whereas E_{ther}, E_{turb}, and E_{mag} helps expansion of the gas region. We

calculated gravitational boundness of dense cores in our simulations to judge the gravitational instability of those dense cores, as described in Chapters 2 and 3.

If only thermal pressure supports the dense gas against gravitational collapse, the threshold mass above which a dense gas will undergo such collapse is called the Jeans mass, which is determined by Jeans instability. Jeans instability occurs for length

$$\lambda > \lambda_{\mathrm{J}} = \frac{\pi c_s^2}{G\rho}, \tag{1.9}$$

where c_s is isothermal sound speed, G is the gravitational constant, and ρ is density and the mass scale associated, i.e., Jeans mass, for a spherical gas region is

$$M_{\mathrm{J}} = \frac{4\pi}{3}\rho \left(\frac{\lambda_{\mathrm{J}}}{2}\right)^3. \tag{1.10}$$

A pressureless gas sphere of uniform density with no initial velocity field will collapse in a finite free-fall time (Spitzer, 1978),

$$\tau_{\mathrm{ff}} = \sqrt{\frac{3\pi}{32G\rho}}. \tag{1.11}$$

This free-fall time is typical timescale for gravitational collapse of gravitationally bound region to formation of a star.

1.1.3   Low-mass star formation and difficulty in massive star formation

Our current understanding of low-mass star formation is as follows. Low-mass stars form by accreting gas from a molecular core of which self-gravity is dominant than thermal and non-thermal (magnetic and turbulent) pressures. Shu (1977) analysed the collapse of a singular isothermal sphere and deduced the accretion rate as

$$\dot{M} \sim \frac{c_s^3}{G} = 10^{-6} \left(\frac{T}{10\,\mathrm{K}}\right)^{3/2} M_\odot \mathrm{yr}^{-1}, \tag{1.12}$$

where c_s is the isothermal sound speed. The accretion rate with observed temperature of 10 K is consistent with the formation times of low-mass stars (Lada, 1999).

This low-mass star formation theory cannot be simply applied for massive star formation. The reason is as follows. Protostars of low-mass and massive stars evolve differently. Protostar changes on Kelvin-Helmholtz timescale,

$$t_{\mathrm{KH}} = \frac{GM_*^2}{2R_*L_*}, \tag{1.13}$$

where M_*, R_*, and L_* are mass, radius, and luminosity of the star. This timescale shows the time required to radiate gravitational binding energy of protostar. For massive protostars, the Kelvin-Helmholtz timescale is shorter than infall timescale, and star will contract to main sequence while still gaining mass by accretion. Radiation pressure is exerted from the main sequence star onto surrounding gas and dust. This radiation pressure from massive stars could be strong enough to stop further accretion (Wolfire and Cassinelli, 1987) and the accretion rate in equation (1.12) is not sufficient to overcome this radiation pressure. This can set an upper limit on stellar masses of massive stars and this upper limit is inconsistent with observed stellar masses of massive stars. Other processes in the protostar like the disk wind can also limit the mass of the massive star (Tanaka, Tan, and Zhang, 2017). This raises an interesting question of how massive stars are able to keep accreting. This is the major difficulty in applying low-mass star formation theory for massive stars. Next, we describe importance of massive stars and possible scenarios for massive star formation.

1.1.4 Massive stars and their importance

Stars with masses greater than around 8 $M_\odot$ are defined as massive stars. This 8 $M_\odot$ lower limit is not entirely fixed, and this limit arises from stars that are just able to combine carbon with other elements and also end up in supernova explosion at the end of their lifetime.

Massive stars use up their fuel faster than low- to intermediate-mass stars. Roughly, a solar-mass star's estimated lifetime is ~ 300 times longer than a 10 $M_\odot$ star. Massive stars also are very luminous. Roughly, a 10 $M_\odot$ star has estimated luminosity similar to ~ 3500 Suns. They are one the most luminous stellar objects in our universe.

However, massive stars are extremely rare. Salpeter (1955) estimated that the number of massive stars formed per unit mass interval scales as $M^{-2.35}$, where M is stellar mass. This imply that massive stars constitute less than 1% of total stars. For example, for each 20 $M_\odot$ star in the Milky Way, there are roughly a hundred thousand solar-type stars.

Despite their rarity, massive stars are important in astrophysics. They strongly impact the ISM and galaxy formation. This is due their huge energetic output. They also supply heavy metals which are used in the formation of next-generation stars. They also regulate next-generation star formation, affect evolution of galaxies, and may have re-ionized the universe.

1.1.5 Possible scenarios for massive star formation

For massive star formation, two major scenarios, monolithic collapse and competitive accretion, are proposed (e.g. Zinnecker and Yorke (2007)). For the monolithic collapse scenario, the mass required for massive star formation is associated

with the final product. The protostellar core participates in this mass. For competitive accretion scenario, the material that makes up a particular star can come from various parts of the parent cloud. The only gas that is associated with any particular protostar is in its circumstellar disk and envelope. Since multiple protostars are often formed together simultaneously, each protostar competes for the available molecular material.

Both scenarios require a massive molecular core or massive gas region for massive star formation. It has been pointed out that a large gas accretion rate is needed to overcome the radiation pressure from embedded protostar in its dense core in the monolithic collapse scenario of massive star formation (McKee and Tan, 2002). They proposed that in a massive dense core with sufficient internal turbulent motion, a high accretion rate flow can persist, and its ram pressure can exceed the radiation pressure from a protostar. Magnetic fields act as a support mechanism against gravitational collapse and can increase the Jeans mass, thus increasing the mass of the dense core by preventing its fragmentation (Offner et al., 2014). A large accretion rate flow onto a protostar can be realized in such a dense core. In this way, sufficient turbulence and magnetic fields can play an important role in massive star formation in such massive cores. However, formation of such a massive core is still unclear. External triggering mechanisms are proposed for the formation of massive star formation (Elmegreen, 1998). In next Section 1.2, we describe one such external trigger, cloud-cloud collision, which our whole thesis focuses on.

1.2   Cloud-cloud collision (CCC)

Figure 1.1: Schmematic view of massive star formation triggered by CCC
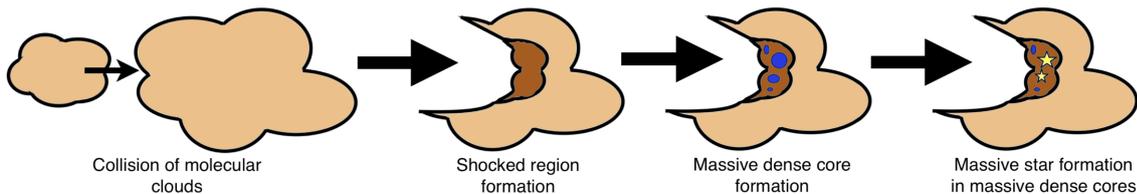
CCCs are one of the most important candidates for triggering massive star formation (see recent review by Fukui et al. (2021)). In Section, we describe the theoretical studies of CCCs. In the Sections 1.2.2 and 1.2.3, we describe the observational evidence which support this CCC mechanism and the galaxy-scale simulations which highlight the frequency of CCCs.

1.2.1   Theoretical studies

Stone ([1970](#)) performed the first numerical simulation of colliding interstellar clouds, assuming two identical interstellar clouds of neutral hydrogen with densities of 5–10 atomic hydrogen cm^{-3}, colliding at a speed of 10 km s^{-1}. This was one-dimensional study of atomic gas clouds not molecular clouds. Stone ([1970](#)) showed that both atomic gas, colliding clouds are destroyed in the collision, since the collision speed is highly supersonic, and the duration of the collision is too short for the growth of self-gravitational instability.

As an extension to formation of molecular clouds, Smith ([1980](#)) simulated one-dimensional colliding flows, including radiative gas cooling, formation, and dissociation of molecules. He showed that a dense molecular gas layer is formed in collision of atomic gas clouds. He also discussed the gravitational instability of this layer and showed that a slower collision speed is favorable for gravitational instability of the layer.

Two-dimensional numerical simulations of collisions between two dense molecular clumps were performed by Gilden ([1984](#)) and they showed that dense, gravitationally unstable gas layers are formed by these collisions. Habe and Ohta ([1992](#)) extended these simulations to head-on collisions between non-identical clouds, since collisions of non-identical clouds are more realistic than those of identical clouds. They showed successfully that non-identical clouds helps form gravitationally unstable massive core than identical clouds.

Due to these studies, we got mechanism for massive star formation triggered by CCC. Figure [1.1](#) shows the schematic view of this mechanism. The collision of molecular clouds at a supersonic speed creates a shocked region at the interface of those colliding clouds. The radiative cooling further increases the density in the shocked region. Dense clumps can be formed in the dense shocked region due to the enhanced self-gravity of the shocked region (Gilden, [1984](#)). The collision of clouds with different sizes leads to a converging flow in the shocked region, and it can increase the mass of the dense clumps (Habe and Ohta, [1992](#)). We can expect massive star formation in those massive clumps/cores. Subsequently, based on this picture, many three-dimensional numerical simulations of colliding clouds were performed.

1.2.2   Observational evidence

From the velocity separations of the clouds, Oort ([1954](#)) estimated that such clouds often undergo collisions. This was the first observational evidence of the important role of CCCs. Recent observational studies have provided evidence that CCCs trigger high-mass star formation in the Milky Way (e.g., Hasegawa et al. ([1994](#)), Furukawa et al. ([2009](#)), Ohama et al. ([2010](#)), Dewangan et al. ([2016](#)), Torii et al. ([2017](#)), Fukui et al. ([2018b](#)), Fukui et al. ([2018a](#)), and Fujita et al. ([2021](#))).

Enokiya, Torii, and Fukui (2021) lists more than 50 high-mass star-forming regions for which observational evidence of massive star formation triggered by a CCC is found.

To suggest occurrence of CCC, observational researchers have relied on three typical features of CCC, namely, 1) U-shaped cavity, 2) complementary distribution, and 3) bridge connecting colliding clouds. The U-shaped cavity can be present due to the collision of dissimilar clouds, as shown in the schematic view in Figure 1.1. We show other two features taking evidence of CCC in Trifid Nebula, M20, of Milky Way. Torii et al. (2017) identified these features in two colliding clouds, 2 km s^{-1} cloud and cloud C, of the galactic HII region M20. First is a complementary distribution where cloud C coincides with the gas at the center of 2 km s^{-1} cloud, as shown in Figure 1.2. Second is three bridge features that connect the two clouds in velocity space, as shown in Figure 1.3.
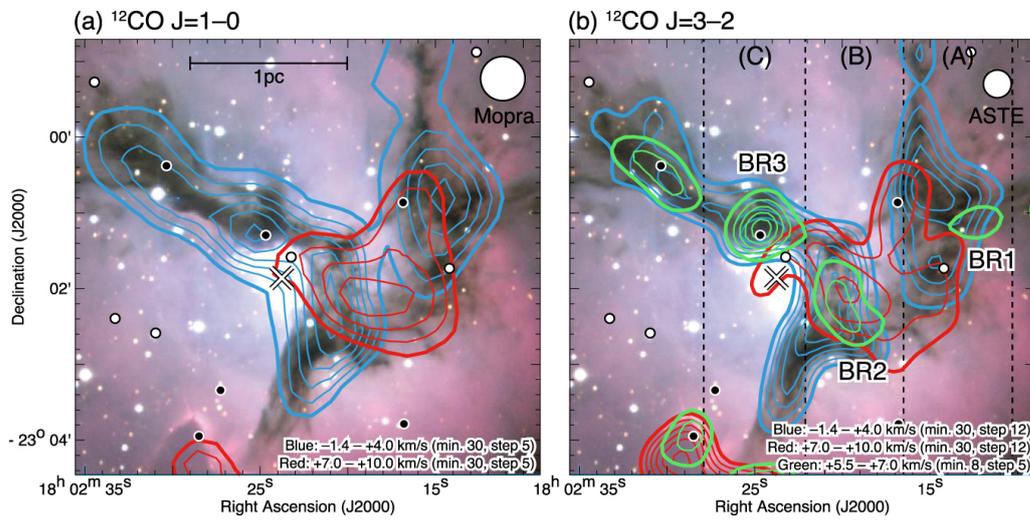
Figure 1.2: (From Torii et al. (2017)) The contour maps of the two colliding clouds are shown superimposed on the optical image of M20, where the ^{12}CO J=1–0 emission is shown in (a) and ^{12}CO J=3–2 is in (b). 2 km s^{-1} cloud and cloud C are plotted in blue contours and red contours, respectively. In (b) the bridge features BR1, BR2, and BR3 are added with green contours. The velocity range and the contour levels are shown in the right-bottom of each panel.

1.2.3   Frequency of CCCs

Few hydrodynamics simulations of galaxy dynamics have been carried. Tasker and Tan (2009) simulated galaxies with no spiral potential and found frequency of 1 collision per $1/4^{th}$ orbit. Fujimoto, Tasker, and Habe (2014) simulated galaxies with an imposed spiral and bar potential and found merger rates as high as 1 collision per $1/40^{th}$ orbit. In galaxy simulations of Dobbs, Pringle, and Duarte-Cabral (2015), they found that the frequency of mergers or collisions of clouds > $10^4 M_\odot$ is about one per 8-10 Myr, or 1 per 15th of an orbit (typically one merger
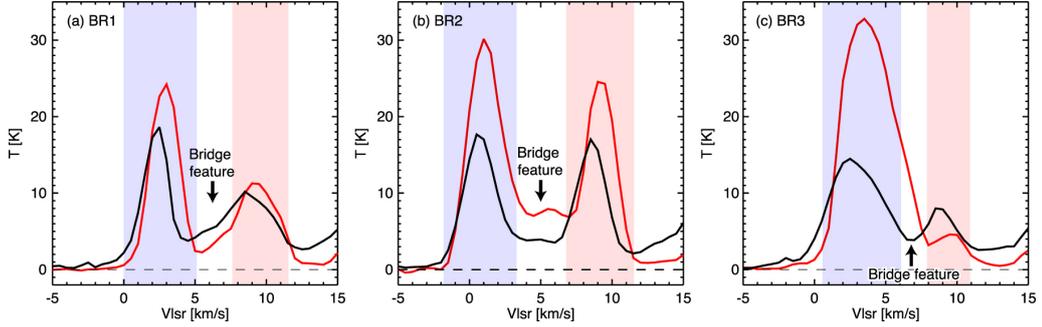
Figure 1.3: (From Torii et al. (2017)) ^{12}CO J=1–0 (black) and ^{12}CO J=3–2 (red) spectra toward the bridge features BR1, BR2, and BR3. The velocity ranges of the 2 km s^{-1} cloud and cloud C are shaded in blue and red, respectively.

per cloud lifetime). Overall, these studies indicate a significant frequency of collisions.

Fujimoto, Tasker, and Habe (2014) found higher merger raters in the bar region than the spiral part of their simulated galaxy. They demonstrated that variation of star formation efficiency in the galaxy could be a result of variation in CCC speeds in different parts of the galaxy. Although Dobbs, Pringle, and Duarte-Cabral (2015) found high frequency of CCCs, their results demonstrated that collisions are either mere interactions that don't affect the colliding clouds or mergers which still retain the initial properties of the colliding clouds. However, further high-resolution galaxy-scale simulations should be carried out to sufficiently resolve these colliding clouds to study their interactions.

1.3   Important parameters in CCC

For massive star formation in CCC, magnetic field and collision speed should be important parameters. These parameters depend on the galactic environment. For example, observed magnetic field strength is typically 6 μG in molecular clouds near Sun and can be high as 1 mG near the galactic center. Observed cloud collision speeds are typically in the range of 10 to 20 km s^{-1}. We describe these important parameters in the following Sections 1.3.1 and 1.3.2.

1.3.1   Effect of magnetic field in CCC

Many studies in the recent decade have carried out three-dimensional cloud-scale magnetohydrodynamic simulations to study effect of magnetic field on the formation of dense filaments, dense cores, stars, and clusters in colliding clouds or colliding atomic gas flows (Inoue and Fukui, 2013; Chen and Ostriker, 2014; Chen and Ostriker, 2015; Wu et al., 2017b; Wu et al., 2017a; Inoue et al., 2018; Wu et al., 2020; Dobbs and Wurster, 2021). Chen and Ostriker (2014) has shown

that the typical mass of pre-stellar cores formed in the colliding clumps in a large molecular cloud is unaffected by the magnetic fields. They found the formation of low-mass cores of masses $\sim$ 0.04 - 2.5 $M_\odot$ in their simulations. They assumed collision speed of $\sim$ 4 km s^{-1}, which is as large as the typical turbulent velocity observed in molecular clouds. Since the typical turbulent velocity is much smaller than the observed collision speeds of CCCs, CCC simulations with more higher collision speeds than their simulations should be done to understand the collision of magnetized clouds with the observed collision speeds. Wu et al. (2017a) and Wu et al. (2017b) have shown that the star formation in the CCC in their numerical simulations with the typical collision speed is unaffected by magnetic fields. Wu et al. (2020) studied the effect of various magnetic field strengths on star formation in colliding clouds. In their strongest critically magnetized, colliding clouds model (50 µG), which is near the magnetically critical case, they found a reduced number of newly formed stars due to high magnetic pressure. They used a spatial resolution of 0.1 pc which is comparable to sizes of dense cores of which typical scale is 0.1 pc (Bergin and Tafalla, 2007). Internal properties of dense cores (e.g., their internal turbulent energies, magnetic field energies and self-gravitational energies) are important for evolution of dense cores. A higher spatial resolution is required to well resolve the dense cores than their simulations for such a study. Inoue and Fukui (2013) carried out colliding flow simulations and found that massive cores are formed due to MHD shock. Inoue et al. (2018) developed this study with sink particles. They simulated collision of a dense clump with uniform dense region with a typical collision speed with high spatial resolution of 0.0015 pc which is much smaller than the typical size of the molecular core. Their results are in favor of massive star formation due to the effect of magnetic fields. Figure 1.4 shows the illustration of the physical mechanism of the filament formation proposed by Inoue and Fukui (2013), where the evolution of a dense clump after shock compression is considered. A filament perpendicular to the plane of the paper is created at the stage 3. Here the dense clump under consideration is created by the initial turbulence before the collision. Thus, in the simulation, many dense clumps exist before the shock sweeps the small cloud, and the existence of many clumps leads to the formation of many filaments in the shock crushed cloud. This can lead to formation of massive filaments which can ultimately lead to massive star formation. These studies indicate that the role of magnetic field on massive star formation in CCC is quite important.

1.3.2   Effect of collision speed in CCC

Collision speed can play an important role in massive dense core formation in CCCs (Takahira, Tasker, and Habe, 2014; Takahira et al., 2018). Takahira, Tasker, and Habe (2014) and Takahira et al. (2018) have shown that high collision speeds can suppress massive core formation in CCCs using hydrodynamic simulations. Figure 1.5 shows that massive core formation takes place in their 3 and 5 km s^{-1}
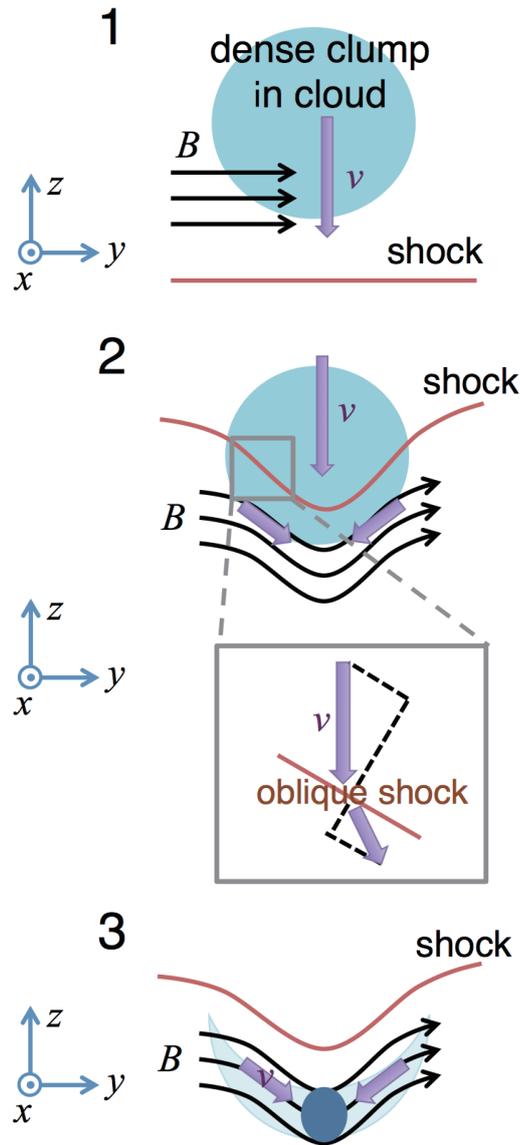
Figure 1.4: (From Inoue et al. (2018)) Illustration of the physical mechanism of the filament formation proposed by Inoue and Fukui (2013), where the evolution of a dense clump after shock compression is shown.

collisions, whereas mass growth of dense core is highly suppressed in their 10 km s^{-1} collision. They suggested that duration of collision controls this, with more duration favorable for massive star formation. Since the duration of collision is important for core mass evolution as demonstrated by Takahira, Tasker, and Habe (2014) and Takahira et al. (2018), larger-sized clouds would be favorable for massive bound dense core formation in high-speed CCCs. Enokiya, Torii, and Fukui (2021) have surveyed many observational candidates of CCCs and have shown evidence that massive star formation is more active in higher speed CCCs
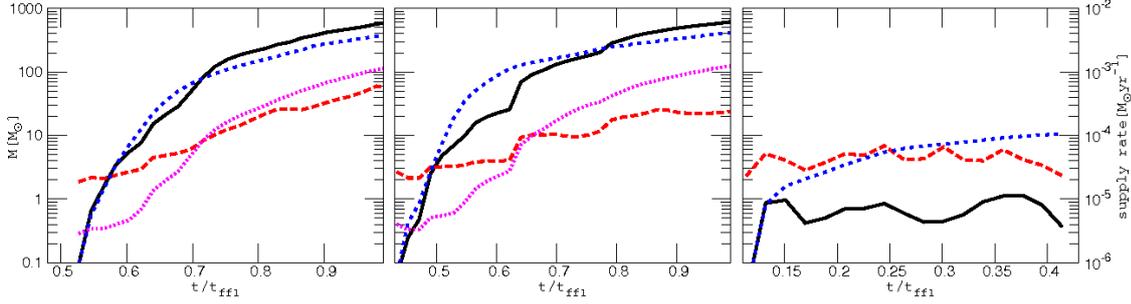
Figure 1.5: (From Takahira, Tasker, and Habe (2014)) Mass evolution of the bound core. Left to right shows the core formed in simulations in 3, 5 and 10 km s^{-1} speed collisions. Since no bound core is formed in the 10 km s^{-1} case, the evolution of the most massive core is shown. The black line marks the core mass, the blue dotted line is the accreted mass, the red dashed line is the effective Jeans mass and the pink dashed line shows the supply rate; the ratio of the core's collapsing mass to its free-fall time, $\max(0.5 M_{\text{core}}, M_{\text{J,eff}})/t_{\text{ff}}$ whose axis is on the right.
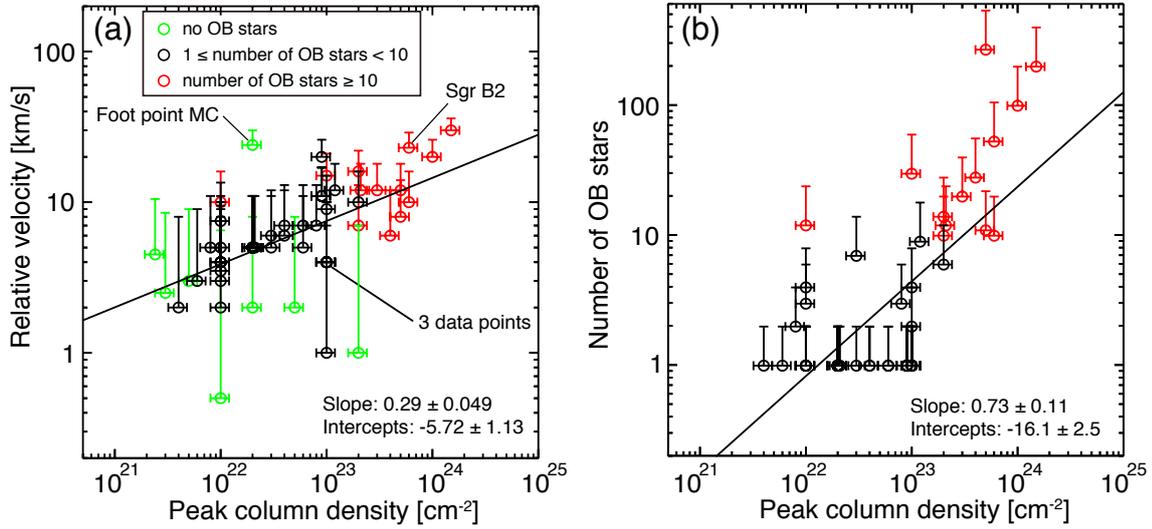
Figure 1.6: (From Enokiya, Torii, and Fukui (2021)) (a) Scatter plot of the peak column density and relative velocity of colliding clouds of the Galactic sources on a double-logarithmic scale. The black, red, and light green symbols, respectively, indicate CCCs associated with clusters having less than ten O- and early B-type stars, more than ten O- and early B-type stars, and without O- and early B-type stars. The black line indicates the best-fit result of black and red symbols using a least-squares method. (b) Scatter plot of the peak column density and the number of O- and early B- type stars of colliding clouds of the Galactic sources on a double-logarithmic scale. The black line indicates the best-fit result of black and red symbols using a least-squares method.

with higher column density, as shown in Figure 1.6. We discuss our results by comparing with this observed result in Chapter 3.

These studies indicate that precise role of magnetic fields and collision speeds

on massive bound core formation in magnetized, colliding clouds is of key interest in pursuit of the the wider goal of better understanding massive star formation.

1.4 Motivation and Aim of this thesis

Previous studies mentioned in Sections 1.3.1 and 1.3.2 indicate that precise role of magnetic fields and collision speeds on massive bound core formation in magnetized, colliding clouds is of key interest in pursuit of the the wider goal of better understanding massive star formation. This motivated us to continue this pursuit to understand the physical conditions for massive star formation in CCCs. We majorly concentrated on important parameters of magnetic field and collision speed. For this, we carried out a series of numerical studies utilizing magnetohydrodynamics (MHD) simulations with adaptive mesh refinement (AMR) and sufficient resolution to create increasingly more detailed models of CCCs and study massive core/star formation in them.

1.5 Outline of next chapters

In Chapter 2, we study effects of magnetic fields on massive dense core formation in colliding unequal molecular clouds by performing MHD simulations with sub-parsec resolution (0.015 pc) that can resolve the molecular cores.

In Chapter 3, we study the effects of high collision speeds on massive dense core formation in colliding unequal molecular clouds by performing MHD simulations of colliding clouds.

In Chapter 4, we summarize our results on effects of magnetic fields and collision speeds on massive core/star formation triggered by CCC. We also discuss future works based on our current results and our ongoing works in this chapter.

Chapter 2

Effect of magnetic field on massive core/star formation by CCC

2.1 Chapter highlight

Aim: We study the effects of magnetic fields on massive dense core formation in colliding unequal molecular clouds by performing magnetohydrodynamic simulations with sub-parsec resolution (0.015 pc) that can resolve the molecular cores.

Models: Initial clouds with the typical gas density of the molecular clouds are immersed in various uniform magnetic fields. The turbulent magnetic fields in the clouds consistent with the observation by Crutcher et al. (2010) are generated by the internal turbulent gas motion before the collision, if the uniform magnetic field strength is 4.0 μG. The collision speed of 10 km s^{-1} is adopted, which is much larger than the sound speeds and the Alfvén speeds of the clouds. We identify gas clumps with gas densities greater than 5×10^{-20} g cm^{-3} as the dense cores and trace them throughout the simulations to investigate their mass evolution and gravitational boundness.

Results: We show that a greater number of massive cores ($> 10 \, M_\odot$) and massive, gravitationally bound cores are mostly formed in the strong magnetic field (4.0 μG) models than the weak magnetic field (0.1 μG) models. This is partly because the strong magnetic field suppresses the spatial shifts of the shocked layer that should be caused by the nonlinear thin shell instability. The spatial shifts promote the formation of low-mass dense cores in the weak magnetic field models. The strong magnetic fields also support low-mass dense cores against gravitational collapse. We show that the numbers of massive, gravitationally bound cores formed in the strong magnetic field models are much larger than in the isolated, non-colliding cloud models, which are simulated for comparison.

Discussion: We discuss the implications of our numerical results on massive star formation.

2.2 Numerical method and models

2.2.1 Numerical method

We use simulation code ENZO, a three-dimensional MHD adaptive mesh refinement (AMR) code (Bryan et al., 2014). We assume ideal MHD in our simulations. The code solves the MHD equations using the MUSCL 2nd-order Runge-Kutta temporal update of the conserved variables with the Harten-Lax-van Leer (HLL) method and a piecewise linear reconstruction method (PLM). The hyperbolic divergence cleaning method of Dedner et al. (2002) is adopted to ensure the solenoidal constraint on the magnetic field.

We describe numerical methods of the cooling, the pressure floor, and the Alfvén speed limiter used in our simulations. Radiative cooling of gas is calculated down to 10 K by using the cooling table made by the CLOUDY cooling code (Ferlandf et al., 1998) with the solar metallicity and a density $n_H = 100$ cm^{-3}. For example, the cooling time of gas with a density $n_H = 100$ cm^{-3} from 100 K to 10 K is estimated to be less than 0.1 Myr by using the cooling table. Due to this rapid cooling of molecular gas, the dense gas reaches the typical cloud temperature of GMC, 10 K. Photoelectric heating with the rate of 1.2×10^{-25} $(n_H/1$ cm$^{-3})$ erg s^{-1} cm^{-3} is applied to gas (Tasker and Bryan, 2008). Self-gravity in the gas is included in our simulations. The pressure floor is applied for the cell in the finest grid level in which absolute value of self-gravitational energy of gas is greater than its internal energy (Machacek, Bryan, and Abel, 2001). The pressure floor kicks in at a gas density of $\sim 10^{-15}$ g cm^{-3} for a cell at gas temperature of 10 K in the finest grid level. Tests with a higher (lower) value of the pressure floor parameter by a factor of 10 (1/3) resulted in a very similar core population and probability density functions, and so our simulation results are unlikely to be influenced by any numerical effects of our default pressure floor parameter. The Alfvén speed, v_A, is given by

$$v_A = \frac{B}{\sqrt{4\pi\rho}},$$

(2.1)

where B is magnetic field strength, ρ is density, and the CGS system of units are used in all equations related to magnetic field in this paper. The maximum Alfvén speed is set to be 20 km s^{-1} to avoid very short time-steps created due to high Alfvén speeds in low gas density regions, which is effectively limited by increasing the gas density in such regions. We find that the Alfvén speed limiter works in very small regions with much lower gas density than the initial density of our model clouds. The minimum density in our simulations is selected as the initial density of the ambient medium of 1.69×10^{-23} g cm^{-3}, as given in Section 2.2.2. Tests with a highe r value of the maximum Alfvén speed by a factor of 5 and with a lower value of the minimum density by a factor of 1/10 resulted in a very similar core population and probability density functions to our simulation results with our default values of the maximum Alfvén speed and the minimum

Table 2.1: Initial cloud model parameters.

Parameter[*]	Isolated cloud	Small cloud	Large cloud	Units
R	7.3	3.5	7	pc
M	8746	972	7774	$M_\odot$
ρ_0	3.67×10^{-22}	3.67×10^{-22}	3.67×10^{-22}	g cm^{-3}
t_{ff}	3.5	3.5	3.5	Myr
σ_v	2.1	1.0	2.0	km s^{-1}
v_{coll}	—	10	0	km s^{-1}

[*] R—cloud radius, M—cloud mass, ρ_0—cloud initial density, t_{ff}—free-fall time of the cloud, σ_v—the velocity dispersion of the cloud, v_{coll}—the collision speed of the cloud.

density. We use yt, a multi-code analysis toolkit for astrophysical simulation data, (Turk et al., 2011) to analyze our numerical results. The yt is very powerful to analyze numerical results given by ENZO code.

2.2.2 Cloud models

Initial cloud structure and collision setup

We adopt initial conditions for clouds based on properties of observed GMCs (Heyer et al., 2009; Murray, 2011). Two uniform molecular clouds, a small cloud and a large cloud, are initialized with density 3.67×10^{-22} g cm^{-3} of which free-fall time is 3.5 Myr and with masses 972 $M_\odot$ and 7774 $M_\odot$, respectively. We stop our simulations at $t = 3.0$ Myr, which is earlier than the free-fall time. These cloud masses are rather small in comparison to observed GMCs in the Milky Way of which the mass range is 10^3-10^6 $M_\odot$ (Murray, 2011). We select small clouds to achieve high spatial resolution needed to study the effect of the magnetic field on the formation of massive dense cores in the colliding clouds with a rather small simulation box that we describe in the next paragraph. We adopt initial temperatures of the clouds as 68 K and 273 K for the small cloud and the large cloud, respectively. While such temperatures are sufficient to provide initial pressure support, the dense gas in the clouds rapidly cools down to 10 K due to the radiative cooling during evolution. We adopt turbulence in clouds (see Section 2.2.2). Parameters for each cloud are summarized in Table 2.1. A typical collision speed of 10 km s^{-1} is used. The ambient medium has a density of 1.69×10^{-23} g cm^{-3} and a temperature of 800 K. This high density of the ambient medium is used to avoid high Alfvén speeds in the ambient medium.

Six different colliding clouds models are considered, each with differing initial magnetic field strength and direction (see Section 2.2.2 and Table 2.2). Our

Table 2.2: Simulation models.

Model no.	Model name	B_0 (µG)[*]	θ[†]
1	Xweak	0.1	0°
2	Yweak	0.1	90°
3	XYweak	0.1	45°
4	Xstrong	4.0	0°
5	Ystrong	4.0	90°
6	XYstrong	4.0	45°
7	ISweak	0.1	90°
8	ISstrong	4.0	90°

[*] The initial magnetic field strength,
[†] The angle between the initial magnetic field, B_0, and the collision axis (x-axis).

simulation domain encompasses (32 pc)^3 with root grids 128^3, and we use four refinement levels based on the condition of minimum baryon mass of 0.05 $M_\odot$ for refinement. This gives the minimum cell size of 0.015 pc at the maximum refinement level. We have tested our simulations with additional higher refinement levels; level five and level six. The minimum cell size is 0.0075 pc for the refinement level five and 0.0037 pc for the refinement level six. The minimum cell size of 0.0037 pc satisfies the minimum resolution criterion in hydrodynamic simulations of self-gravitating gas proposed by Federrath et al. (2011) for the typical core size of 0.1 pc. We find that core mass functions and core properties in simulations with these higher refinement levels are very similar to the simulation results with our default refinement levels.

Additionally, two different isolated, non-colliding cloud models are used for comparison with the results of colliding clouds models (e.g., the population of dense cores). This isolated cloud has a sum of the masses of both the small and the large clouds, and it also includes turbulent motion (see Table 2.1). Two different initial magnetic field strengths are selected similarly to the colliding clouds (see Section 2.2.2). We summarize the simulation results of the isolated cloud models in the Appendix A.

Magnetic field and turbulence in clouds

The clouds are immersed in an initial uniform magnetic field, B_0, and turbulent motions develop inside them from $t = 0$ to 0.5 Myr. A turbulent magnetic field is generated inside clouds before the small cloud begins to move towards the

large cloud at $t = 0.5$ Myr along the collision axis (positive x-axis of the simulation box). We select two strengths of B_0, $B_0 = 0.1$ µG (weak) and $B_0 = 4.0$ µG (strong) and three directions of B_0, which are parallel to the collision axis, perpendicular (along positive y-axis) to the collision axis, and oblique to the collision axis. The angle, θ, between B_0 direction and collision axis for oblique B_0 model is $45°$. Additional isolated cloud models have B_0 with magnetic field strengths $B_0 = 0.1$ µG (weak) and 4.0 µG (strong) similar to those selected for colliding cloud models. The direction of B_0 is taken along the positive y-axis of the simulation box. We name the simulation models as shown in Table 2.2.

Turbulent velocities are generated to be consistent with the Larson relation (Larson, 1981; Heyer et al., 2009) at $t = 0$ Myr, by imposing a velocity field with power spectrum $v_k^2 \propto k^{-4}$. We define $k = (2\pi)(n_x e_x + n_y e_y + n_z e_z)/(aR)$, where e_x, e_y, and e_z are unit vectors in x-direction, y-direction, and z-direction, respectively, R is the radius of each cloud, and $a \sim 4$. We use integers for n_x, n_y, and n_z as $n_{\min}^2 \leq n_x^2 + n_y^2 + n_z^2 \leq n_{\max}^2$, where $n_{\min}$ and $n_{\max}$ are 6 and 12 for the small cloud and 8 and 15 for both the large cloud and isolated cloud, respectively. If the initial kinetic energy of turbulence is in virial equilibrium with the self-gravitational energy, the velocity dispersion, σ_v, of clouds due to the turbulent motion is σ_v = 0.86 km s^{-1} for the small cloud and $\sigma_v = 1.72$ km s^{-1} for the large cloud. We slightly increase these values to $\sigma_v = 1.0$ km s^{-1} for the small cloud and $\sigma_v = 2.0$ km s^{-1} for the large cloud to be consistent with the observational results by Heyer et al. (2009).
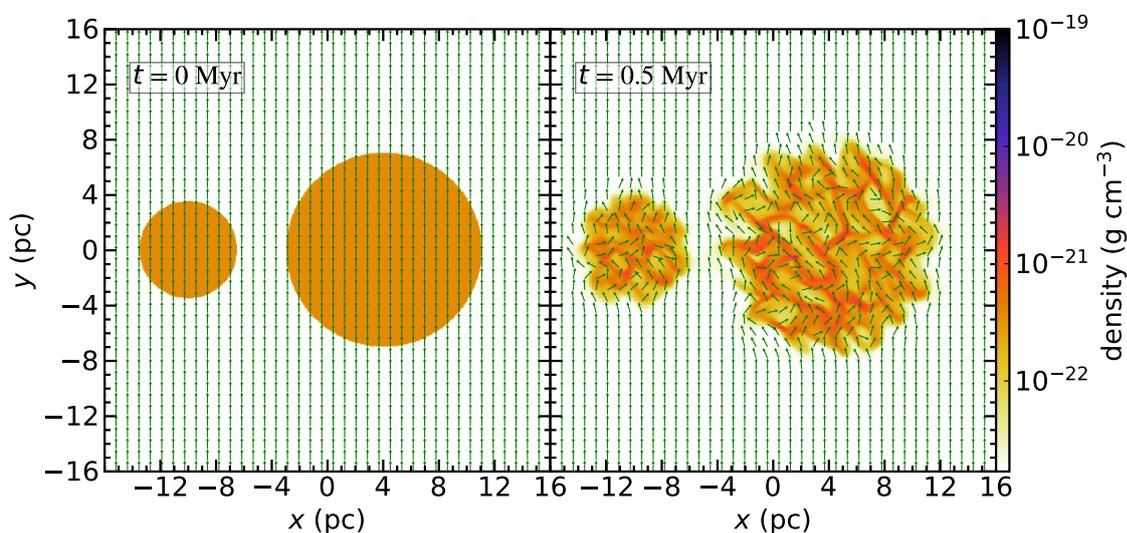

Figure 2.1: Slice plots of the gas density in $z = 0$ pc at $t = 0$ Myr (left) and 0.5 Myr (right) for the Ystrong model. The arrows show normalized vectors, $[B_x/(B_x^2 + B_y^2)^{1/2}, B_y/(B_x^2 + B_y^2)^{1/2}]$. Color bar of the gas density is shown on the right edge.
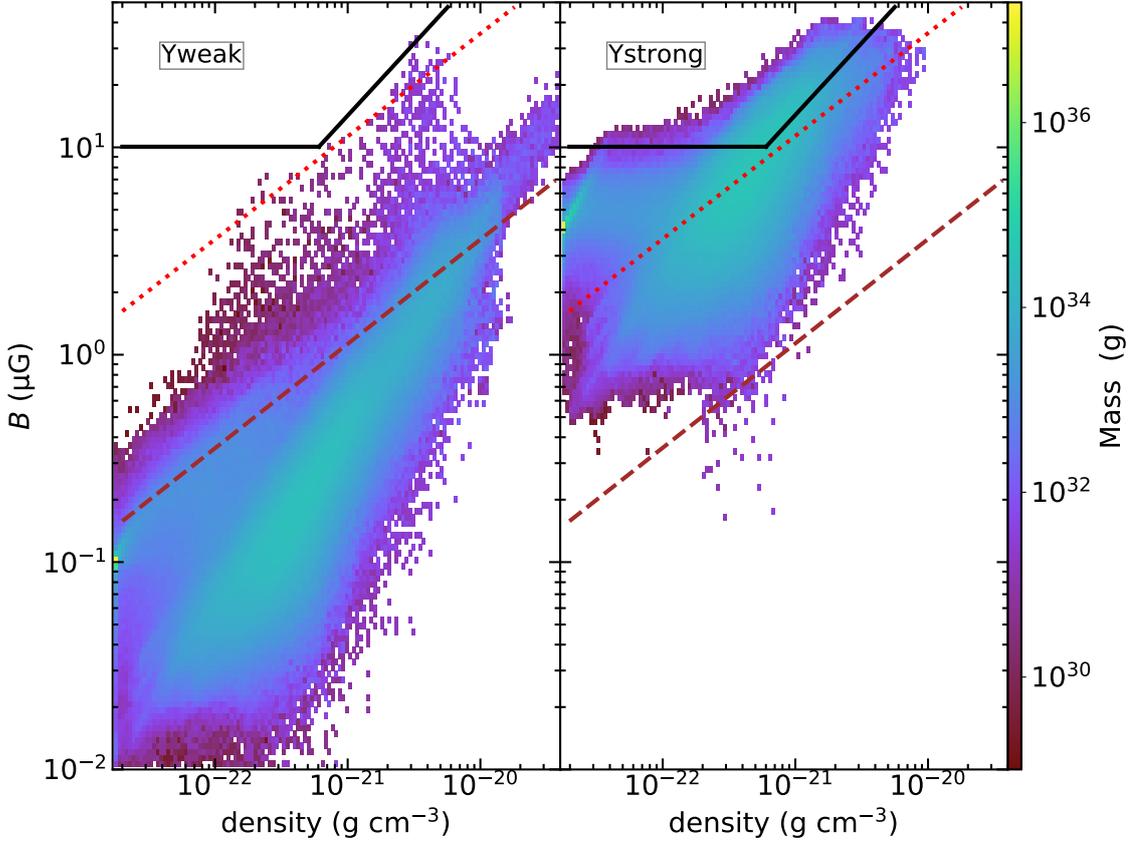
Figure 2.2: Phase plot of the magnetic field strength and the gas density in the Yweak (left) and Ystrong (right) models at $t = 0.5$ Myr. Solid lines show the observed relation by Crutcher et al. (2010). Dotted lines show Alfvén speed, $v_A = 1$ km s^{-1} and dashed lines show Alfvén speed, $v_A = 0.1$ km s^{-1}. The colors show total mass of the simulation cells with density, ρ, and magnetic field strength, B, in the range from ρ to $\rho(1 + \Delta_1)$ in x-axis and B to $B(1 + \Delta_2)$ in y-axis, where $\Delta_1 = 0.063$ and $\Delta_2 = 0.069$, and the color bar is shown on the right edge.

We show the effect of turbulence on the initial magnetic field before the collision starts. Figure 2.1 shows turbulent density structures and turbulent magnetic fields of the small and large clouds at $t = 0$ and 0.5 Myr in the Ystrong model. In Figure 2.1, B_0 is perpendicular to the collision axis. The arrows in Figure 2.1 show normalized vectors, $[B_x/(B_x^2 + B_y^2)^{1/2}, B_y/(B_x^2 + B_y^2)^{1/2}]$. The variation of the magnetic field direction in the clouds seen at $t = 0.5$ Myr is due to the effect of turbulence. We show the magnetic field and density relation in the simulation box of the Yweak (weak B_0) and the Ystrong (strong B_0) models at $t = 0.5$ Myr in Figure 2.2. In the Yweak model (left-hand panel of Figure 2.2), the turbulent magnetic fields in clouds are weaker than the observed relation between the magnetic field and gas density given by Crutcher et al. (2010), indicated by a solid line in Figure 2.2. In the Ystrong model (right-hand panel of Figure 2.2), the turbulent magnetic fields in the clouds are consistent with the observed relation. Figure

2.2 shows that the magnetic fields in both clouds are dominated by the turbulent magnetic fields that are much stronger than B_0. We also show the constant Alfvén velocities of 1 km s^{-1} (dotted lines) and 0.1 km s^{-1} (dashed line) in Figure 2.2 for comparison with the turbulent velocities in clouds and the collision speed of the clouds, 10 km s^{-1}. The magnetic field and density relation before the collision are independent of the direction of $\boldsymbol{B}_0$. Hence, the pre-collision results of only the Ystrong and Yweak models are shown in this section.
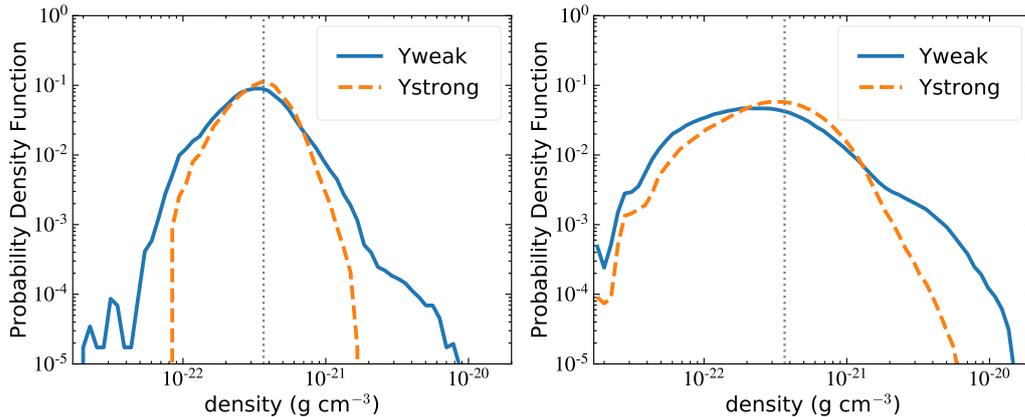
Figure 2.3: Probability density functions (PDFs) of the small cloud (left) and the large cloud (right) at $t = 0.5$ Myr for the Yweak (solid line) and Ystrong (dashed line) models. The vertical dotted line indicates the initial density of clouds. In order to neglect the effect of gas motion near each cloud surface, we select spheres of radii equal to 85 % of the initial cloud radii centered at the initial cloud centers for PDFs.

The probability density functions (PDFs) of the small cloud and the large cloud at $t = 0.5$ Myr before collision are shown in Figure 2.3. The initial density of both clouds is indicated by the vertical dotted lines in Figure 2.3. The PDFs of both the clouds are log-normal shaped due to the effect of turbulence generated, and the extended tail is due to the effect of self-gravity (Kritsuk, Norman, and Wagner, 2011; Takahira, Tasker, and Habe, 2014). The log-normal part is narrower in the Ystrong model than the Yweak model. This result is qualitatively consistent with Padoan and Nordlund (2011), who simulated supersonic, self-gravitating, MHD turbulence. In the Ystrong model, the extended tail is much narrower than that in the Yweak model. This is due to the higher magnetic field pressure that suppresses density enhancement of gas in the Ystrong model compared to that in the Yweak model.

2.3   Numerical results

We show numerical simulation results of colliding cloud models. Isolated cloud numerical simulation results are used for comparison. Numerical simulation results of isolated cloud models are given in Appendix A.

2.3.1 Weak B_0 models

Collision induced structure
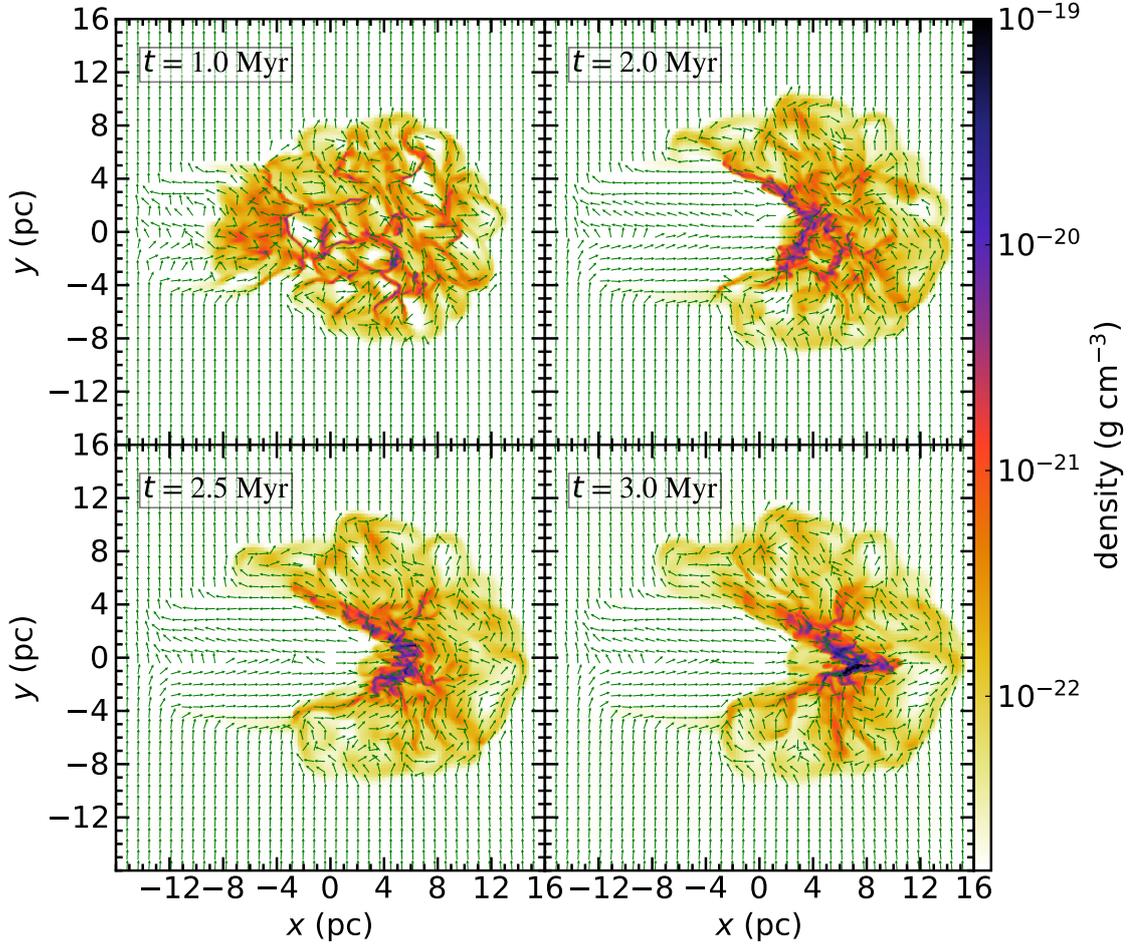
Figure 2.4: Slice plots of the gas density in $z = 0$ pc at $t = 1.0$ Myr (top left), 2.0 Myr (top right), 2.5 Myr (bottom left), and 3.0 Myr (bottom right) for the Yweak model. The arrows show normalized vectors and the color bar shows gas density, same as in Figure 2.1.

As a typical result of the weak B_0 models, we show numerical results in of the Yweak model in Figure 2.4, where $\boldsymbol{B}_0$ is perpendicular to the collision axis. As shown in the left-hand panel of Figure 2.2, the magnetic fields in the clouds are expected to have a minor effect on the gas motion induced by collision, since the Alfvén speed in the clouds is much less than the collision speed, 10 km s^{-1}. In Figure 2.4, we show the time evolution of the Yweak model at four epochs, $t =$ 1.0 Myr, 2.0 Myr, 2.5 Myr, and 3.0 Myr. At $t = 1.0$ Myr, the two clouds already touch each other, and a thin shocked layer is formed at the interface of the two clouds. At $t = 2.0$ Myr, the mass of the shocked layer increases from $t = 1.0$ Myr, and a cavity in the left-hand side of the shocked layer is formed by the small
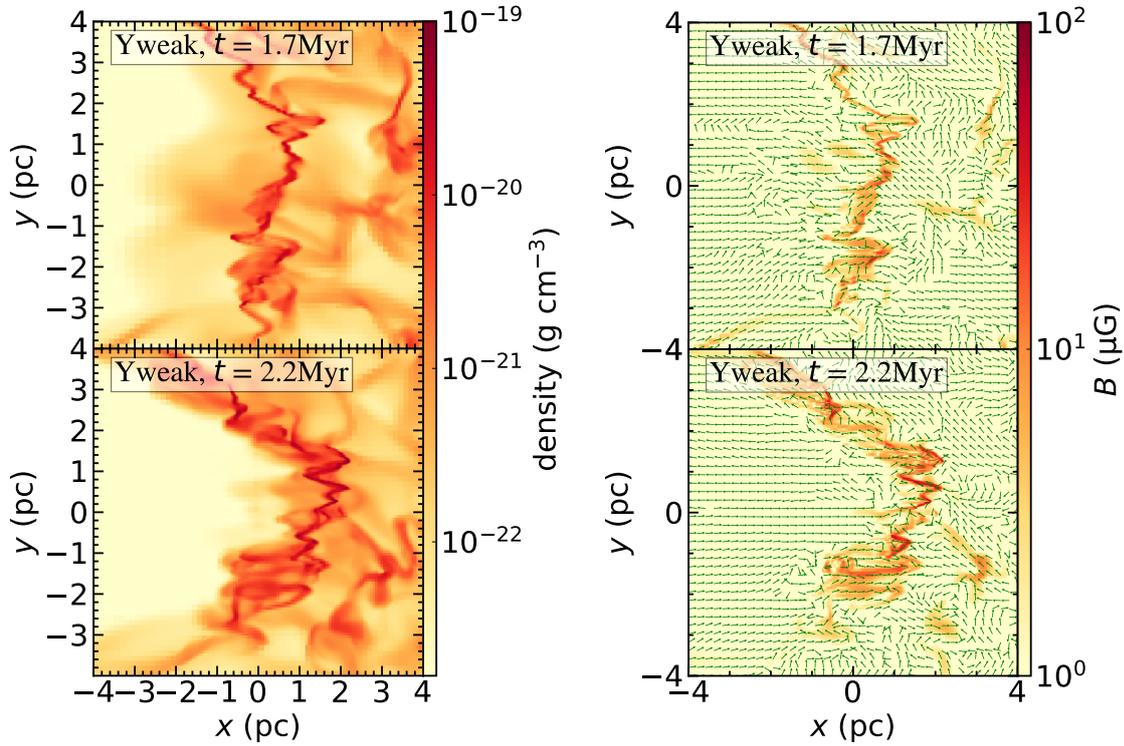
Figure 2.5: Slice plots of the gas density (left) and the magnetic field strength (right) for the shocked layer in close-up in $z = 0$ pc at $t = 1.7$ Myr (top) and 2.2 Myr (bottom) for the Yweak model. Color bars of the gas density (left) and magnetic field strength (right) are shown on the right edge of each panel. In the right panels, the arrows show normalized vectors, same as in Figure 2.1. The x-coordinates are shifted by 1 pc and 3 pc to the collision velocity direction in the top and bottom panels, respectively.

cloud's penetration into the large cloud. The time evolution of colliding clouds in the Yweak model is similar to hydrodynamic simulations of CCC by Takahira, Tasker, and Habe (2014), Takahira et al. (2018), and Shima et al. (2018).

The shocked layer shows quasi-periodic spatial shifts away from a line perpendicular to the collision axis located along the collision interface with scales of less than 1 pc at $t = 2.0$ Myr. Figure 2.5 shows the close-up slice images of gas (left-hand panels) and magnetic field strength (right-hand panels) near the shocked layer at $t = 1.7$ Myr (upper panels) and 2.2 Myr (lower panels). The spatial shifts should be due to the nonlinear thin shell instability (NTSI) (Vishniac, 1994; Anathpindika, 2010) (see Appendix B). Figure 2.5 shows that the spatial shifts develop with time between $t = 1.7$ Myr and $t = 2.2$ Myr. Dense gas concentrations are formed at the extremes of the spatial shifts of the shocked layer. The distribution of magnetic field strength is similar to the gas distribution, as shown in Figure 2.5. This implies that the magnetic field plays a minor role in the evolution of the shocked layer. This can be explained as follows. If a magnetic field is strong enough to control the gas flow, the gas flow along the magnetic field

is easier than the transverse flow. In this case, the gas distribution can be very different from the magnetic field distribution. If magnetic fields are too weak to affect the gas flow, the gas flow will change the magnetic field structure, and the distribution of magnetic field strength can be similar to the gas distribution for a highly turbulent magnetic field as in the post-shock gas in the clouds. At $t = 2.5$ Myr, the shocked layer shape is more concave than $t = 2.0$ Myr, with additional substructures developing in the shocked layer, as shown in Figure 2.4. This is due to the shrinking of the central part of the shocked layer along the collision axis caused by converging flow in the shocked layer. From $t = 2.5$ Myr to 3.0 Myr, the concave shape develops further with additional substructures developing in the shocked layer and dense mass concentrations are formed near $x \sim 5$ pc and $y \sim 0$ pc in Figure 2.4, which is the bottom of the concave shape. A similar evolution is found in the numerical results of the other models with the weak B_0, implying that the magnetic field plays only a minor role in the evolution of the shocked layer in the weak B_0 models.
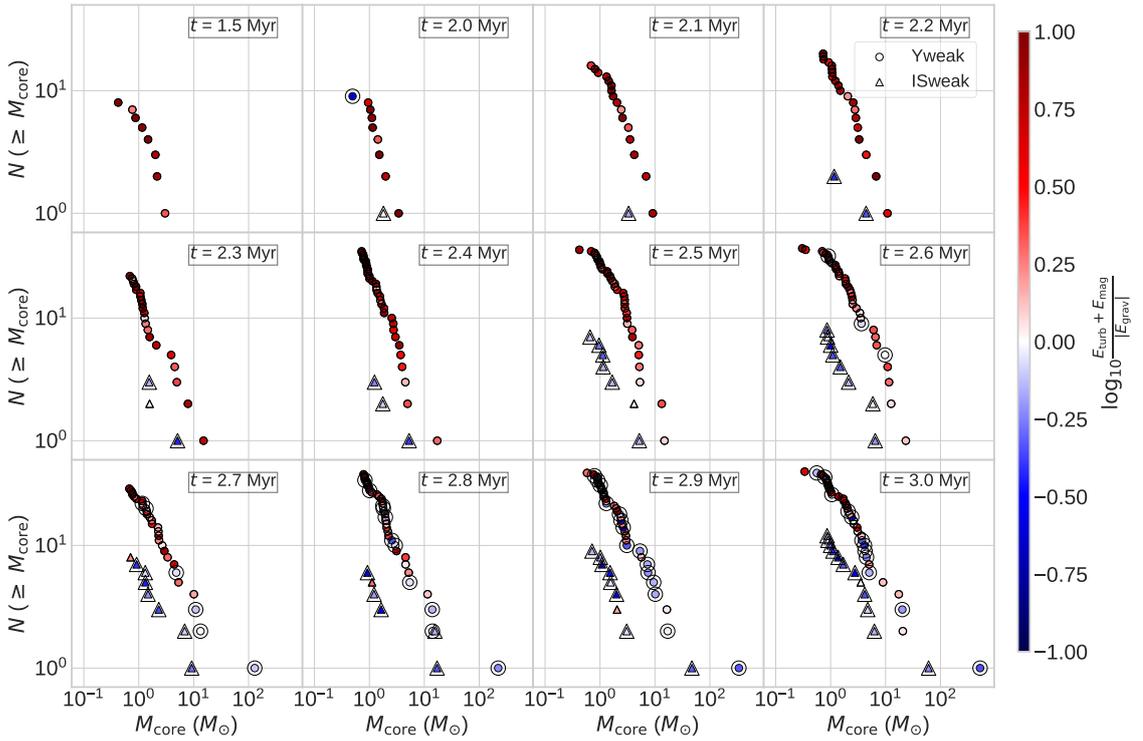
Figure 2.6: Cumulative core mass distributions shown by filled circles and filled triangles at $t = 1.5$ Myr and $t = 2.0$ Myr to 3.0 Myr for the Yweak and ISweak models, respectively. The color bar in the right-hand side shows the energy ratio of turbulent energy plus magnetic field energy to self-gravitational energy (absolute value). The gravitationally bound cores are marked by larger open circles and larger open triangles for the Yweak and ISweak models, respectively.
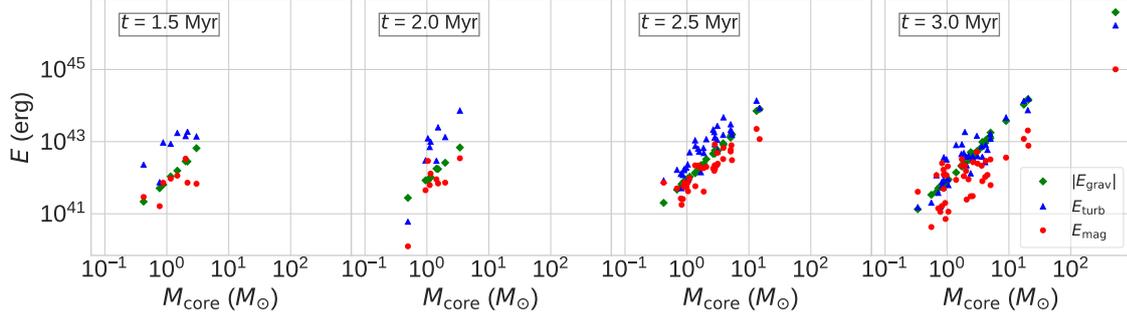
Figure 2.7: Energies of the self-gravity (absolute value) $|E_{grav}|$ (diamond), turbulence E_{turb} (triangle), and magnetic field E_{mag} (circle) of the dense cores at $t = 1.5$ Myr (left), 2.0 Myr (middle left), 2.5 Myr (middle left), and 3.0 Myr (right) for the Yweak model.

Dense core formation and evolution

In order to study dense core formation and evolution, we define a dense core by the threshold density, $\rho_{th} = 5 \times 10^{-20}$ g cm^{-3}, which is in the range of the typical density of molecular cores (Bergin and Tafalla, 2007). We define dense cores by following steps: (1) selection of cells with $\rho \geq \rho_{th}$ as dense cells, (2) grouping together with neighboring dense cells, and (3) rejection of those groups with cell number less than 27. This minimum cell number condition is used to obtain a good resolution of dense cores.

We show a cumulative dense core mass distribution, $N (\geq M_{core})$, which is number of cores with mass more than M_{core}, at $t = 1.5$ Myr and 2.0 Myr to 3.0 Myr in Figure 2.6. We also show the cumulative dense core mass distribution of the isolated cloud model with the weak magnetic field using filled triangles in Figure 2.6. Figure 2.6 clearly shows that more massive dense cores are formed in the colliding clouds model than the isolated model. The dense cores are already formed at $t = 1.5$ Myr and the core number rapidly increases from $t = 2.0$ Myr to $t = 2.5$ Myr in the colliding clouds. In the isolated cloud, the first dense core forms at a later epoch than in the colliding clouds, and the total number of dense cores is also much smaller compared to the colliding clouds at each epoch shown. At $t = 3.0$ Myr, four massive dense cores with their masses greater than 10 $M_\odot$ are formed in the colliding clouds.

We check the gravitational stability of each dense core by comparing its turbulent energy, E_{turb}, its magnetic field energy, E_{mag}, and an absolute value of its self-gravitational energy, $|E_{grav}|$. Here we ignore its thermal energy, since temperature of the dense core is nearly 10 K and the sound speed of gas at this temperature is much smaller than the turbulent velocity and the Alfvén speed. E_{turb} is given for a dense core by

$$E_{turb} = \sum_i \frac{1}{2} m_i |v_i - v_{mean}|^2, \tag{2.2}$$

where i is an index of a dense cell in the dense core, the sum is made over all cells belonging to the dense core, m_i is the mass of the dense cell i, and $\boldsymbol{v}_{\mathrm{mean}}$ is the mean velocity of the dense core given by

$$\boldsymbol{v}_{\mathrm{mean}} = \frac{\sum_i m_i \boldsymbol{v}_i}{\sum_i m_i}. \tag{2.3}$$

E_{mag} is given by

$$E_{\mathrm{mag}} = \sum_i \frac{\boldsymbol{B}_i \cdot \boldsymbol{B}_i}{8\pi} V_i, \tag{2.4}$$

where $\boldsymbol{B}_i$ and V_i are the magnetic field flux density vector and volume, respectively, of the dense cell i. We estimate $|E_{\mathrm{grav}}|$ by

$$|E_{\mathrm{grav}}| = \frac{3GM_{\mathrm{core}}^2}{5\langle R \rangle}, \tag{2.5}$$

where G is the gravitational constant, M_{core} is the mass of the dense core, and $\langle R \rangle$ is given by

$$\langle R \rangle = \left(\frac{3V_{\mathrm{core}}}{4\pi}\right)^{1/3}, \tag{2.6}$$

where V_{core} is total volume of the dense core. In Figure 2.7, we show these energies. If $(E_{\mathrm{turb}} + E_{\mathrm{mag}}) \leq |E_{\mathrm{grav}}|$, we can expect that the dense core is gravitationally bound, and we call such a dense core a gravitationally bound core. Since a dense core is defined by the condition of $\rho \geq \rho_{\mathrm{th}}$, its free-fall time $t_{\mathrm{ff}} \leq 0.3$ Myr. Many cores are gravitationally bound at $t = 3.0$ Myr, as shown in Figure 2.6. The main reason for the formation of gravitationally bound cores is the turbulent energy dissipation, as shown in Figure 2.7. Figure 2.7 also shows that the turbulent energy is still comparable to the gravitational binding energy in the bound cores at $t = 3.0$ Myr. In the monolithic collapse scenario by McKee and Tan (2003), a primary star formed in a massive bound core with such large turbulence will be massive. If we apply the monolithic collapse scenario to those massive bound cores, we can expect massive star formation in them. The most massive dense core is formed in the dense gas region near the bottom of the concave structure of the shocked layer. This core becomes gravitationally bound at $t = 2.7$ Myr, and its mass is 127 $M_\odot$ at this epoch. Rapid mass increase of this core from $t = 2.7$ Myr to 3.0 Myr is due to gas accretion on the core, since this core is in the gas dense region near the bottom of the concave structure of the shocked layer. In the isolated cloud with the weak B_0, the first bound core forms at $t = 2.0$ Myr and its mass is $\sim 2\ M_\odot$. The mass of the bound core increases to $\sim 5\ M_\odot$ after its free-fall time. The other bound cores are formed with mass $\sim 1\ M_\odot$, and the mass evolution of these cores is similar to the first bound one. In the monolithic collapse scenario, a star will form with the free-fall timescale of the bound core. In these bound cores, we can expect low- or intermediate-mass star formation according to the monolithic

scenario, since the core masses are less than 10 $M_\odot$ after their free-fall time from their formation epoch of gravitationally bound cores.

2.3.2 Strong B_0 models

Collision induced structure

As a typical result of the strong B_0 models, we show numerical results of the Ystrong model in which $B_0 = 4.0\,\mu G$ and its direction is perpendicular to the collision axis in Figure 2.8. In this model, the collision speed, 10 km s^{-1}, is larger than the Alfvén speed of gas in both clouds, as shown in the right-hand panel of Figure 2.2. The formation of the shocked layer and formation of the cavity are similar to the weak B_0 models, as shown in Section 2.3.1. However, the cavity produced by the collision of the small cloud displays a wider opening angle than in the Yweak model, as shown in Figure 2.4 and Figure 2.8. This can be explained by the smaller Alfvén Mach number in terms of collision speed (v_{coll}), $M_A = v_{\text{coll}}/v_A$, in this model than in the Yweak model (see Figure 2.2), as in the MHD bow shock wave formed in the solar wind around a planet (Slavin et al., 1984). The shocked layer produced by the CCC is much thicker than that seen in the Yweak model. This may be due to smaller M_A and the larger magnetic pressure in the shocked layer in the Ystrong model than the Yweak model.

Figure 2.9 is a close-up slice image of the shocked layer at t = 1.7 and 2.2 Myr. This Figure shows that there are no clear quasi-periodic spatial shifts of the layer, contrary to the Yweak model. The strong magnetic fields suppress the NTSI in the Ystrong model. The NTSI in an MHD flow was studied by Heitsch et al. (2007). They show that the magnetic fields weaken the NTSI. Density fluctuations of larger sizes than the Yweak model are formed in the shocked layer, as shown in Figures 2.5 and 2.9. The density fluctuations of larger sizes can be formed by Richtmyer-Meshkov instability, by which density fluctuations in the pre-shock region are enhanced in the post-shock gas, as shown by Inoue, Yamazaki, and Inutsuka (2009) and Mizuno et al. (2010). For example, Inoue and Inutsuka (2012) simulated a colliding flow with inhomogeneities of gas density and showed that the post-shock gas is highly turbulent and that density fluctuations in the post-shock gas are created by the development of the Richtmyer-Meshkov instability. More detailed analysis of the Richtmyer-Meshkov instability in our models is beyond the scope of this paper.

The density and magnetic field enhancements are not coincident, as shown in Figure 2.9. Distribution of the magnetic field strength is much smoother than the density enhancements. This indicates that the turbulent magnetic fields on a large scale are enhanced by the CCC flow, and gas moves along the smaller scale magnetic fields to create further density enhancements in the shocked layer. In this way, a difference in density and magnetic field enhancements is produced.
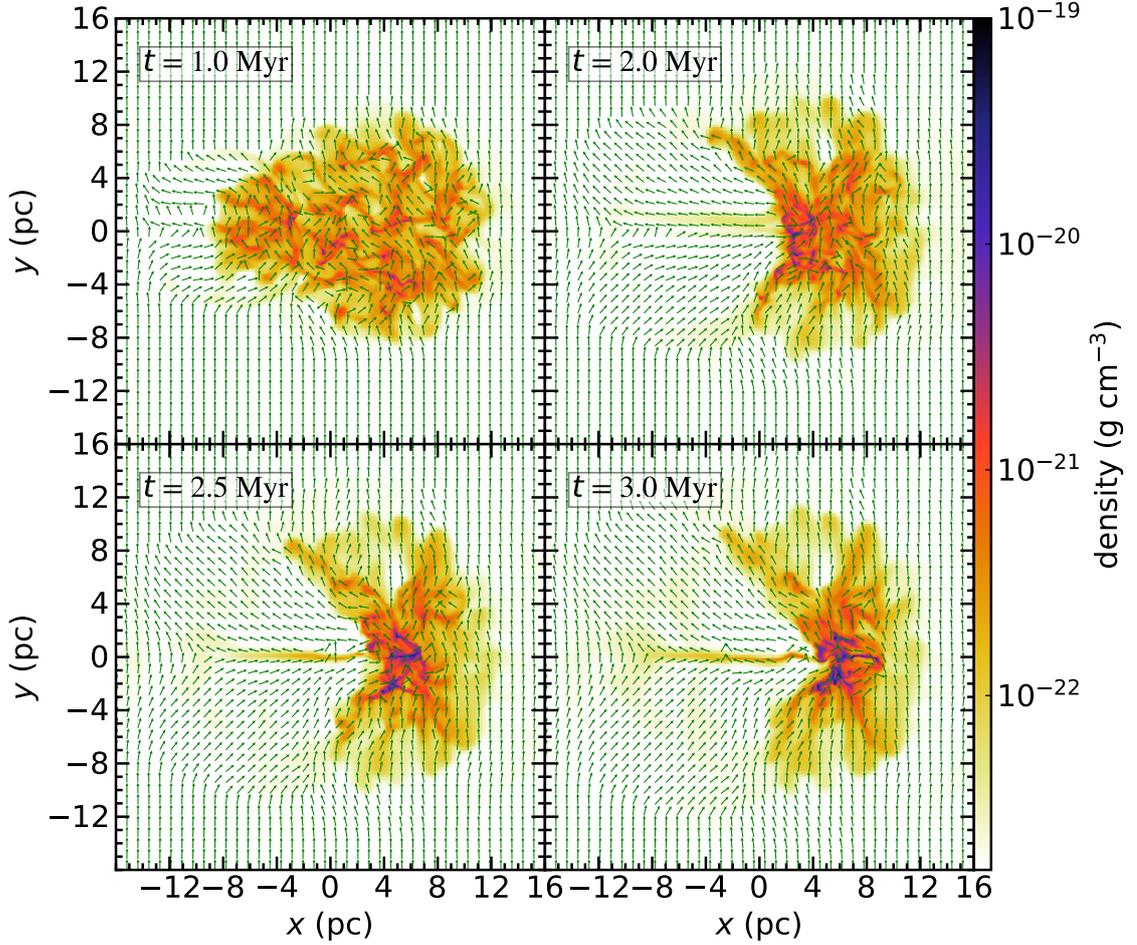
Figure 2.8: Same as Figure 2.4, but for the Ystrong model.

Dense core formation and evolution

We show the time evolution of the cumulative core mass distribution in the Ystrong model in Figure 2.10. The total number of dense cores formed in the Ystrong model is less than that in the Yweak model (see Figure 2.6) during the early phase of collision ($t = 1.5$ Myr). This is due to the suppression of the NTSI in the smaller scales in the Ystrong model. More massive dense cores are formed in the Ystrong model than the Yweak model at $t \gtrsim 2.0$ Myr, and the number of the massive dense cores with masses more than 10 $M_\odot$ is also greater than the Yweak model at $t = 3.0$ Myr. The massive dense core formation is due to gas accumulation to massive dense cores in the dense gas regions in the thick shocked layer, as shown in Figure 2.9.

The time evolution of the magnetic field energy, the turbulent energy, and the absolute value of self-gravitational energy of each dense core with its mass is shown in Figure 2.11 from $t = 1.5$ Myr to $t = 3.0$ Myr. At $t = 1.5$ Myr and 2.0 Myr,

(a) density

(b) magnetic field strength
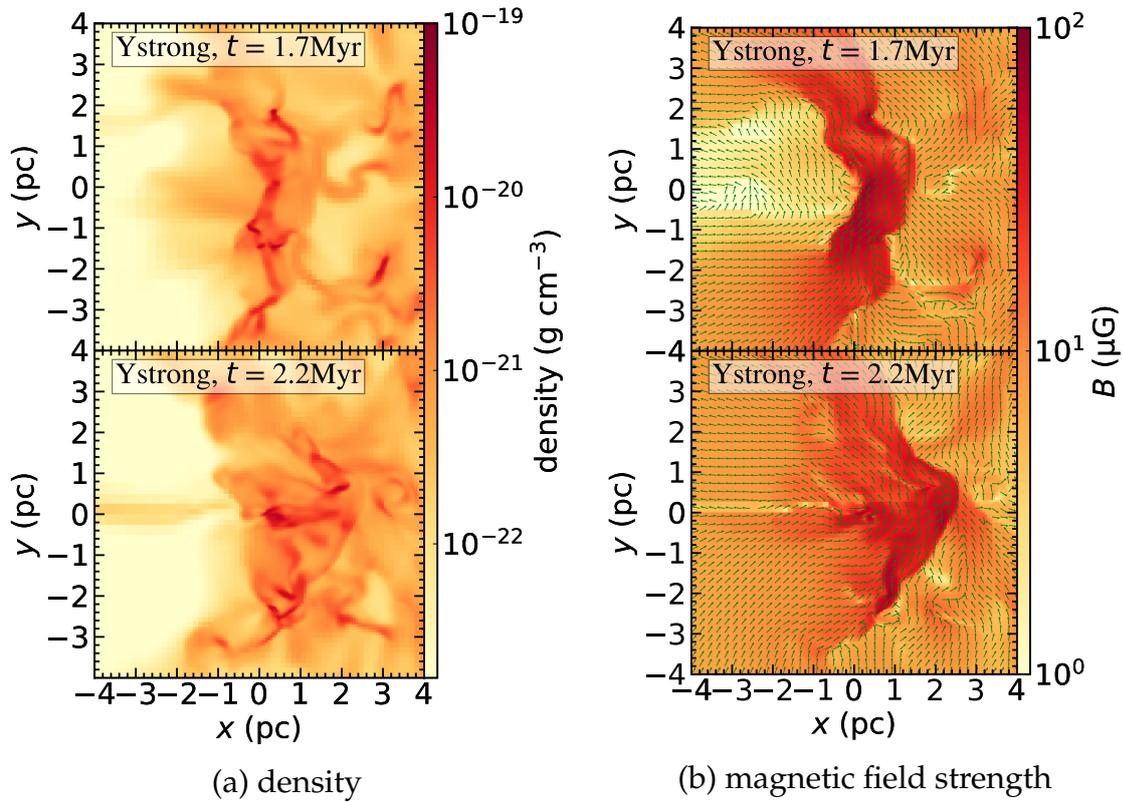
Figure 2.9: Same as Figure 2.5, but for the Ystrong model.

the magnetic field energies are larger than the absolute self-gravitational energies in all cores. However, at $t = 2.5$ Myr and 3.0 Myr, the absolute self-gravitational energies are dominant in the massive dense cores. This change is mainly due to their mass increase by gas accumulation.

The mass evolution of the top 10 massive dense cores and the epoch for them to become gravitationally bound is shown in Figure 2.12. In this figure, we also show merger trees that indicate dense core mergers. The mass growth of any given dense core is a combination of the accretion of surrounding gas and mergers with other dense cores. If the mass contribution by mergers is not enough to explain the mass growth of the dense core, the gas accretion to the dense core should be a dominant process for the mass growth. We estimate mass contribution of core mergers to the mass growth of the top ten massive dense cores. Figure 2.12 shows that Core1 grows from 5 $M_\odot$ at $t = 1.9$ Myr to 132 $M_\odot$ at $t = 3.0$ Myr with mass contribution of 26 $M_\odot$ (20 %) by mergers of dense cores during this time interval. Core2 grows from 2 $M_\odot$ at $t = 1.8$ Myr to 66 $M_\odot$ at $t = 3.0$ Myr with mass contribution of 7 $M_\odot$ (10 %) by mergers of dense cores during this time interval. Core3 grows from 39 $M_\odot$ at $t = 2.4$ Myr to its peak of 110 $M_\odot$ at $t = 2.7$ Myr with a mass contribution of 28 $M_\odot$ (40 %) by one merger at $t = 2.4$ Myr. For
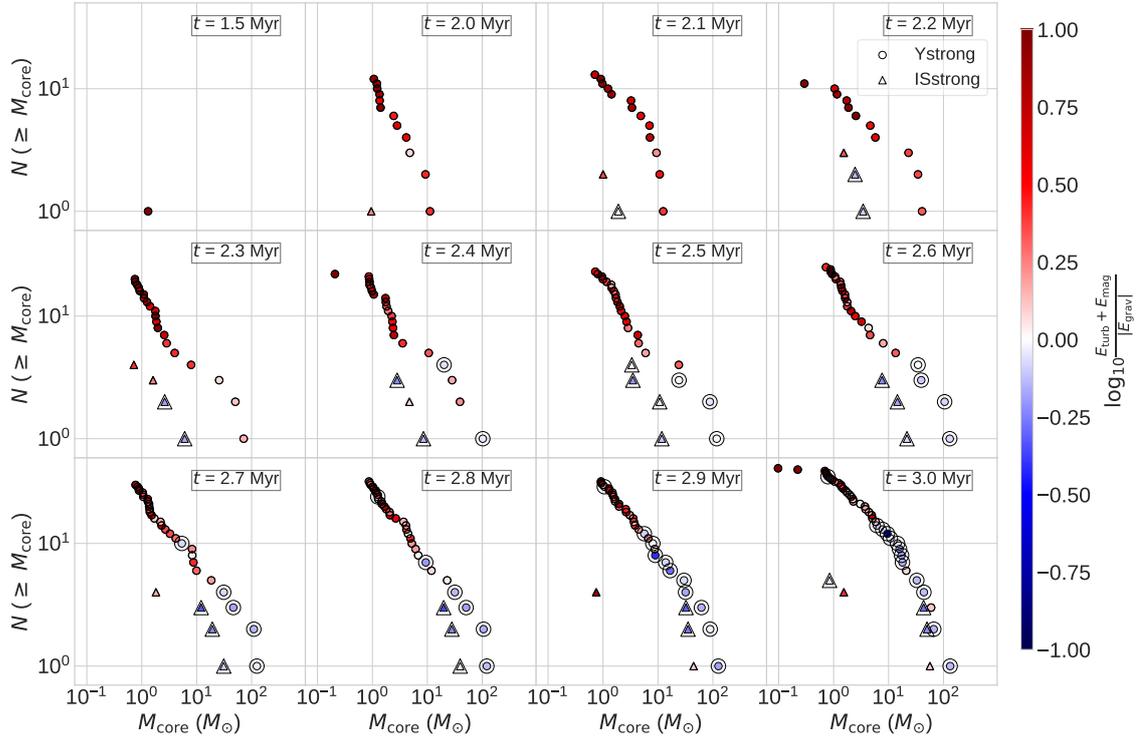
Figure 2.10: Same as Figure 2.6, but for the Ystrong and ISstrong models.
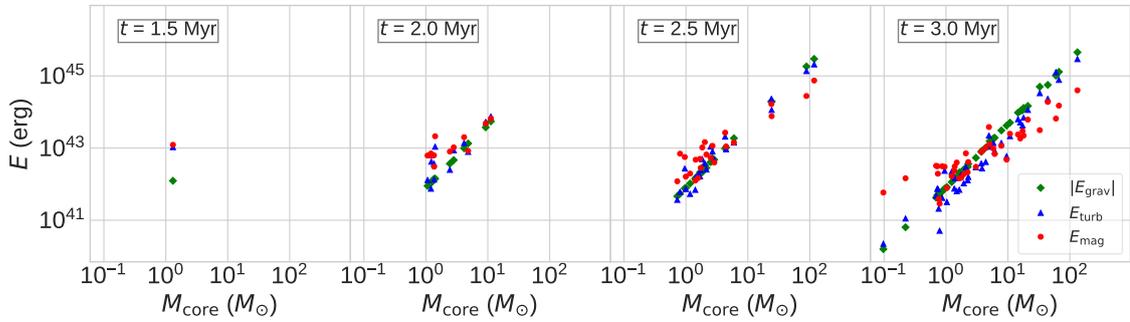
Figure 2.11: Same as Figure 2.7, but for the Ystrong model.

Core4, mergers contribute 5 % mass to the core mass growth. For Core7, mergers contribute 10 % mass up to its peak mass at $t = 2.6$ Myr. There are no mergers for the rest of the massive dense cores. Merger events play more of a secondary effect in increasing the mass of the top ten massive dense cores, with mass growth primarily a smoother function of time implying accretion dominated, evolution. Since the free-fall time of these massive dense cores is less than 0.3 Myr, we expect that protostars form in these cores.
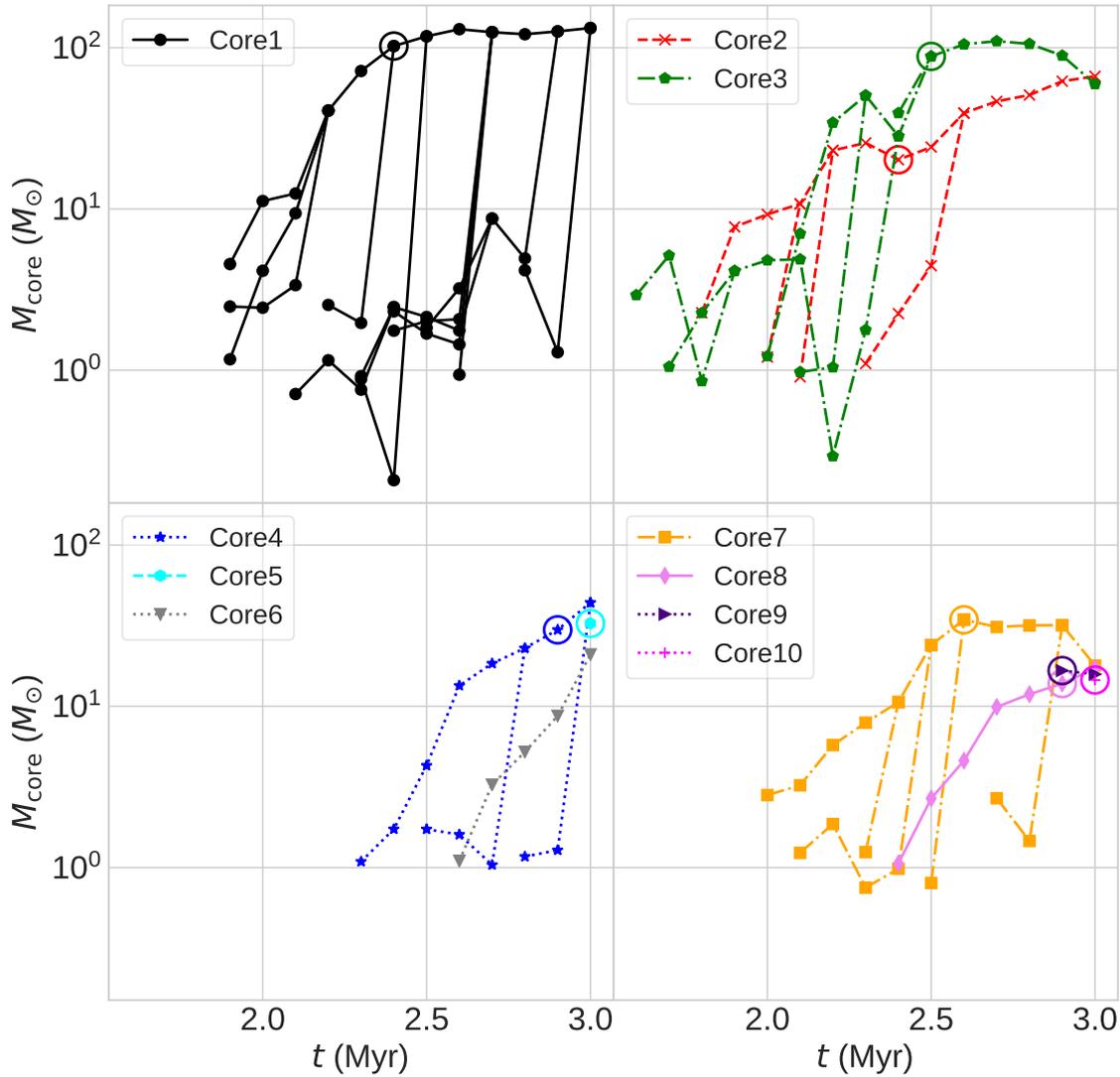
Figure 2.12: Mass evolution of top ten massive dense cores at t = 3.0 Myr in the Ystrong model. The cores are numbered in descending order of their mass. Merging events are shown by joining of the evolutionary tracks of the core. Open circles show the formation epoch of gravitationally bound cores.

We highlight the gravitationally bound cores using larger open circles in Figure 2.10. As shown in Figure 2.10, three massive dense cores become gravitationally bound at t = 2.5 Myr, although these are not gravitationally bound at t = 2.0 Myr. Their masses are larger than 10 $M_\odot$. At t = 3.0 Myr, most dense cores (nine out of the 10) with more than 10 $M_\odot$ become gravitationally bound. The number of bound cores in the Ystrong model is much larger than the Yweak model in which only two bound cores with a masses more than 10 $M_\odot$ are found at t = 3.0 Myr, as shown in Figure 2.6. This may be due to the thick shocked layer caused

by the strong magnetic field in the Ystrong model. The NTSI grows faster for a small-scale shift of the shocked layer. In the Yweak model, the NTSI develops in the small scale shift and results in the accumulation of low-mass gas at the extremes of the quasi-periodic shifts, as shown in Figure 2.5. These gas concentrations move with large irregular velocities, which may suppress further gravitational gas accumulation to the gas concentrations. As a result, this mass growth by gas accretion can be suppressed. In the Ystrong model, since the shocked layer is thickened by the strong magnetic fields, as shown in Figure 2.9, and the dense cores have small irregular velocities by suppression of the NTSI, the dense cores can acquire mass by accretion in the thick shocked layer. The cumulative core mass distribution in the isolated cloud model with the strong magnetic field, $B_0 = 4$ µG, is shown for comparison in Figure 2.10 using filled triangle symbols. The bound cores form earlier than the Ystrong model, and the mass of bound cores just formed is less than 3 $M_\odot$. We can expect intermediate-mass star formation in these cores in the free-fall time ~ 0.3 Myr, assuming that the gas mass in these cores accretes to form a single star. This is very different from colliding clouds models, which hosted bound cores formed with masses greater than 10 $M_\odot$. The resulting formation of protostars can be studied using sink particle models, though this is beyond the scope of the work presented here (Federrath et al., 2010; Shima et al., 2018).

2.3.3 Core mass distribution and gravitationally bound cores

We show the core mass functions of all models at $t = 3.0$ Myr in Figure 2.13. We find many gravitationally bound cores in the strong B_0 models at $t = 3.0$ Myr. The core mass distributions of the weak B_0 models are very similar to each other. In each weak B_0 model, there is one exceptionally massive dense core. In the strong B_0 models, the number of dense cores with mass more than 10 $M_\odot$ is larger than the weak B_0 models. This indicates that the strong B_0 contributes to the formation of a greater number of massive dense cores. The number of massive dense cores in the Xstrong model is slightly smaller than the Ystrong and XYstrong models, yet it is still greater than those in the weak B_0 models (Xweak, Yweak, and XYweak models). These results indicate that the strong magnetic field parallel to the collision axis (as in the Xstrong) is less effective in suppressing the NTSI and in keeping the shocked layer thick, compared with the strong magnetic field with orientations oblique or perpendicular to the collision axis (as in the Ystrong and XYstrong models).

The mass of the most massive dense cores attains more than 100 $M_\odot$ in the last 1 Myr in all models, since we cannot find such massive dense cores at $t = 2.0$ Myr. Since the free-fall time of these cores is less than 0.3 Myr, we can expect rapid protostar formation before $t = 3.0$ Myr. If massive stars are formed in those colliding clouds, we can expect very strong feedback from these massive stars, as shown by Shima et al. (2018).
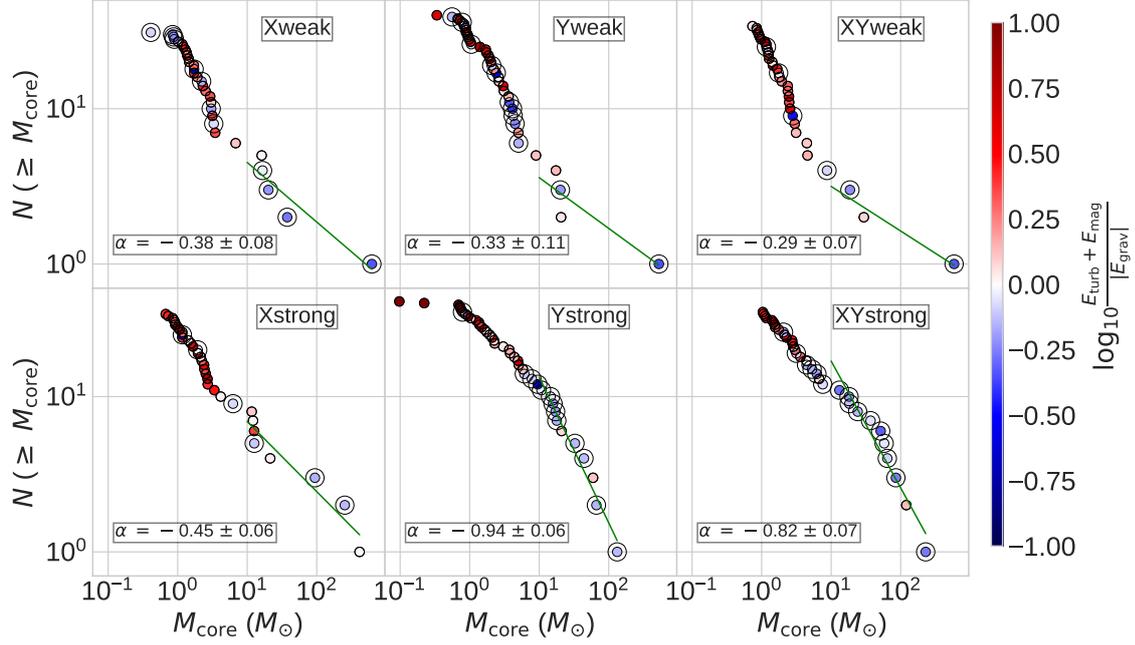
Figure 2.13: Cumulative core mass distributions at $t = 3.0$ Myr for the Xweak (top left panel), Yweak (top middle panel), XYweak (top right panel), Xstrong (bottom left panel), Ystrong (bottom middle panel), and XYstrong (bottom right panel) models. The larger open circles show the gravitationally bound cores. The least square fits with standard deviations for cores with masses greater than 10 $M_\odot$ done using equation 2.8 are shown.

In Figure 2.14, we show the position of cores with masses greater than 10 $M_\odot$ in the strong B_0 models, the Xstrong, Ystrong, and XYstrong models, and the weak B_0 model, the Yweak model, overlaid on the plot of column density looking from the collision axis (x-axis). Large crosses show cores with more than 100 $M_\odot$, and small crosses show cores with 10 $M_\odot < M_{\rm core} < 100$ $M_\odot$. These massive dense cores are distributed along the filaments with column densities greater than 10^{-1} g cm^{-2} in the strong B_0 models. In the Ystrong and XYstrong models, the filaments hosting the massive dense cores are roughly perpendicular to the normalized mass-weighted magnetic field lines of which directions are shown by unit arrows in Figure 2.14.

If the core mass function, ϕ, is defined as

$$\phi = \frac{dN}{dM_{\rm core}} \propto M_{\rm core}^{-\gamma}, \tag{2.7}$$

where $M_{\rm core}$ is the core mass, dN is the number of cores with masses between
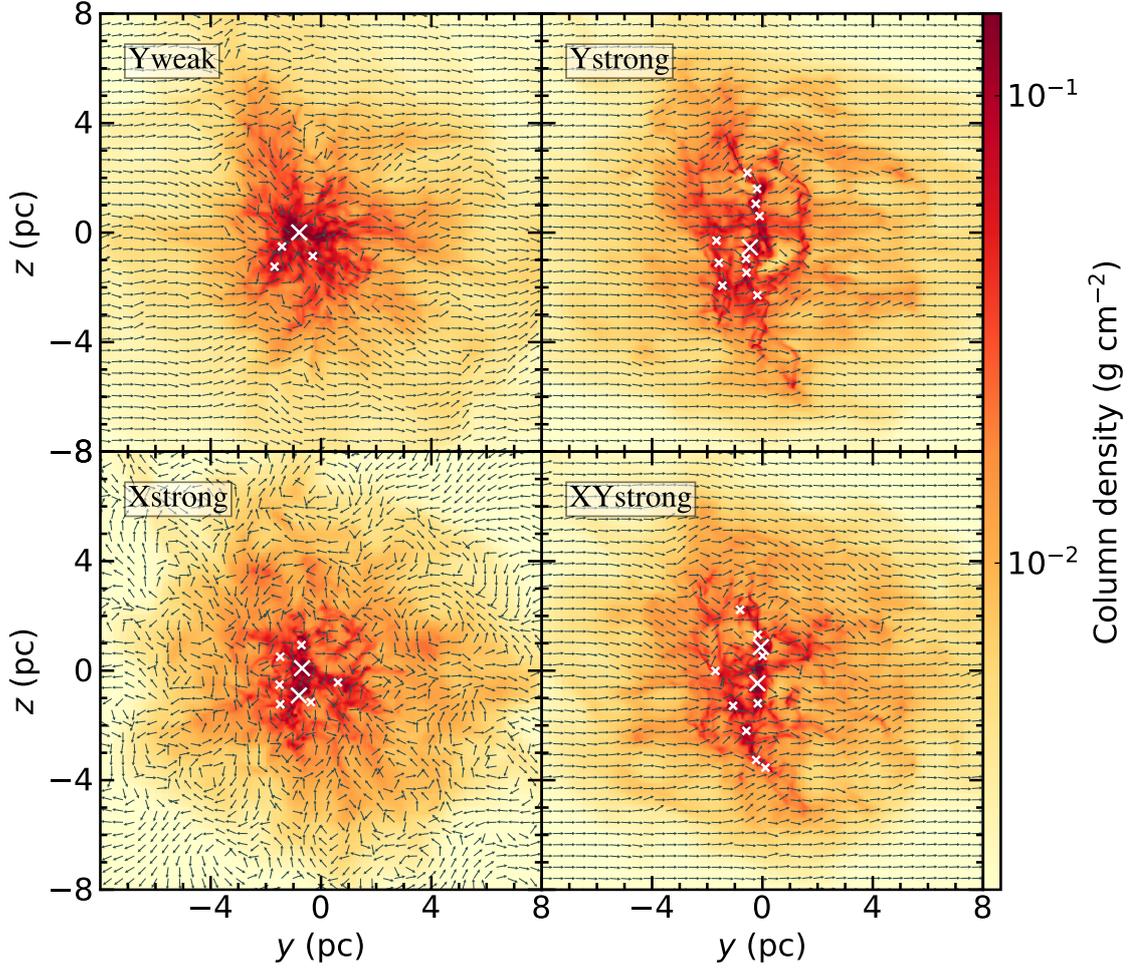
Figure 2.14: The column density along the collision axis in the in the y-z plane at $t = 3.0$ Myr for the Yweak (top left), Ystrong (top right), Xstrong (bottom left), and XYstrong (bottom right) models. The large crosses show massive dense cores more than 100 $M_\odot$, and small crosses show dense cores of $10\,M_\odot < M_{\mathrm{core}} < 100\,M_\odot$. The color bar shows the column density, and the arrows show normalized mass-weighted magnetic fields averaged along the collision axis.

M_{core} and $M_{\mathrm{core}}+dM_{\mathrm{core}}$, and γ is power index of core mass function, the cumulative core mass distribution, $N(\geq M_{\mathrm{core}})$, is given by,

$$N(\geq M_{\mathrm{core}}) = \int_{M_{\mathrm{core}}}^{\infty} \frac{dN}{dM_{\mathrm{core}}} dM_{\mathrm{core}} \propto M_{\mathrm{core}}^{-(\gamma-1)} \propto M_{\mathrm{core}}^{\alpha} \qquad (2.8)$$

where $\alpha = -(\gamma\text{-}1)$. The least square fits (α) using equation 2.8 with standard deviation for cumulative mass distributions of cores with masses greater than 10 $M_\odot$ for all models at $t = 3.0$ Myr are shown in Figure 2.13 . The power indexes of core mass functions, γ, are $\gamma \sim 1.3$ - 1.4 in the weak B_0 models and $\gamma \sim 1.5$ - 1.9 in the strong B_0 models. The strong B_0 models have slightly larger γ than

that in the weak B_0 models. These γ values are similar to those of HD simulations performed by Takahira, Tasker, and Habe (2014) and Takahira et al. (2018). These values are also closer to the observed power indexes of core mass functions (Ikeda, Sunada, and Kitamura, 2007; Uehara et al., 2019), indicating the possible integral role of magnetic fields in determining the observed core mass function.

2.4 Discussion

Our simulation results have shown that a greater number of massive dense cores ($> 10\ M_\odot$) form in the strong B_0 models than the weak B_0 models. In the weak B_0 models, NTSI develops in the shocked layer produced by the CCC and induces the quasi-periodic shifts of the shocked layer in the early stage of CCC. Gas concentrations develop at the extremes of the shifts. In these gas concentrations, dense cores of small mass form earlier than the strong B_0 models. In the strong B_0 models, the turbulent magnetic fields suppress such small-scale NTSI. The turbulent magnetic fields increase the typical scale of NTSI and the thickness of the shocked layer. The turbulent magnetic fields also contribute to the increase in mass of dense cores in the thick shocked layer. Both effects contribute to the formation of massive dense cores in the strong B_0 models. The suppression effect of the magnetic field on NTSI in a shocked region is studied by Heitsch et al. (2007). They have reported that magnetic fields parallel to the shock are more effective in suppression of the NTSI than magnetic fields normal to the shock. This effect can be the reason why the direction of B_0 to the collision axis affects the core mass functions.

In Figure 2.15, we show the concave structures of the shocked layer created by the small cloud penetration into the large cloud in the strong B_0 models at $t =$ 2.0 Myr, as well as for the Yweak model for comparison (all shock fronts in the weak B_0 models look essentially identical). The concave structure indicates a converging flow to the collision axis for the post-shock gas of the small cloud in the left side part of the shocked layer and a diverging flow from the collision axis for the post-shock gas of the large cloud in the right-hand-side part of the shocked layer, since the appearance of oblique part of the concave structure implies that oblique shock wave is formed by the collision of the clouds. The converging flow of the post-shock gas of the small cloud accumulates gas in the shocked layer to the collision axis and contributes to the mass increase of the massive dense cores in the post-shock gas of the small cloud in the later stage of the collision. On the other hand, the diverging flow of the post-shock gas of the large cloud moves away from the collision axis and reduces the gas mass of the shocked layer. Stronger diverging flow appears at the shock more distant from the collision axis, as shown by normalized vectors, $[v_x/(v_x{}^2 + v_y{}^2)^{1/2}, v_y/(v_x{}^2 + v_y{}^2)^{1/2}]$ in Figure 2.15, although the diverging flow is highly disturbed by the turbulent flow in clouds. The diverging flow effect of reducing the gas mass of the shocked
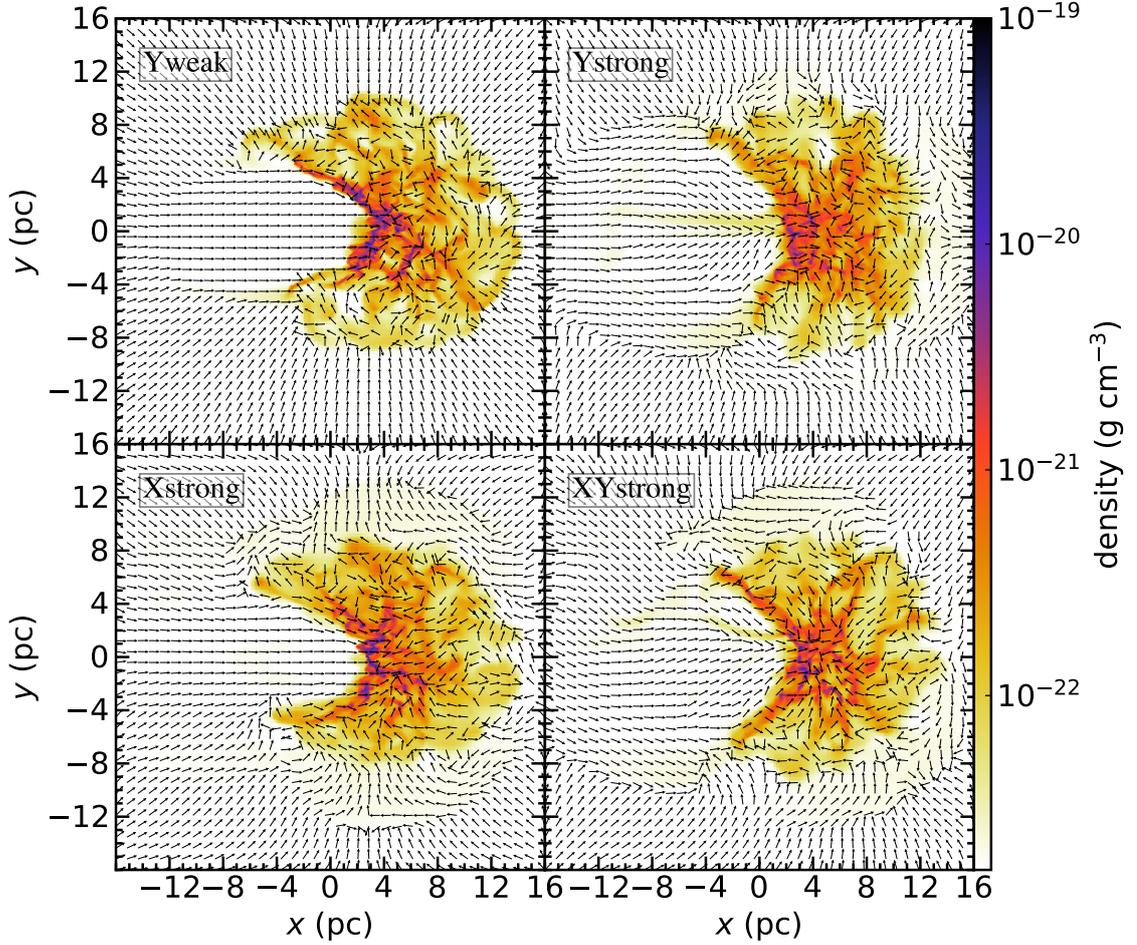
Figure 2.15: Slice plots of the gas density in $z = 0$ pc at $t = 2.0$ Myr for the Yweak (top left), Ystrong (top right), Xstrong (bottom left), and XYstrong (bottom right) models. These panels show that the concave structures produced by the small cloud depend on the direction of B_0. The arrows show normalized vectors, $[v_x/(v_x{}^2 + v_y{}^2)^{1/2}, v_y/(v_x{}^2 + v_y{}^2)^{1/2}]$. Color bar on the right edge shows the gas density.

layer is weaker than the converging flow effect near the collision axis. After the left-hand-side shock of the shocked layer has swept up the small cloud at $t = 1.7$ Myr, we expect a rarefaction wave to propagate rightward in the shocked layer. However, this rarefaction wave does not affect the dominance of the converging flow in the post-shock gas, since speeds of gas flows caused by the rarefaction wave are as high as the magnetosonic speed $\sim 0.4\text{-}3$ km s^{-1}, and they are much less than the converging gas speeds $\sim 5\text{-}10$ km s^{-1} at $t = 2.0$ Myr, which is 0.3 Myr after the complete penetration of the small cloud into the large cloud, as shown in Figure 2.15. The converging gas flow is dominant in the shocked layer at $t = 2.0$ Myr, as shown by the normalized velocity vectors in Figure 2.15. The shape of the concave structure should be closely related to the strength of the converging

flow. If the concave structure is widely opened, we expect a weak converging flow. If the concave structure is instead narrow, we expect a stronger converging flow. Figure 2.15 shows that among the strong B_0 models the concave structure is most widely opened in the Ystrong model and is most narrow in the Xstrong model. The concave structure in the XYstrong is intermediate between them. We expect a stronger converging flow in the Xstrong and a weaker converging flow in the Ystrong model. We also expect that the converging flow in the XYstrong is intermediate between them. The concave structures in those models are consistent with the difference of core mass distributions, if the converging flow indeed contributes to the formation of massive dense cores. The concave structures in the weak B_0 models are similar to the Xstrong model. We expect rather strong converging flow in the weak B_0 models, and this can explain the reason why the mass of the most massive dense core is larger in the weak B_0 models than the strong B_0 models, as shown in Figure 2.13.

We discuss a possible role of magnetic field on self-gravitational instability in the shocked layer. The gravitational instability condition for a disk with a magnetic field B_n is given by

$$\frac{\Sigma \sqrt{4\pi^2 G}}{B_n} = 16.2 \left(\frac{\Sigma}{0.01 \text{ g cm}^{-2}} \right) \left(\frac{B_n}{1 \,\mu\text{G}} \right)^{-1} > 1, \tag{2.9}$$

where B_n is the perpendicular magnetic field to the disk and Σ is the surface density of the disk (Nakano and Nakamura, 1978; Tomisaka and Ikeuchi, 1983). A disk with a parallel magnetic field is gravitationally unstable for a perturbation with a wave number vector parallel to the magnetic field (Tomisaka and Ikeuchi, 1983; Nagai, Inutsuka, and Miyama, 1998). We estimate the gravitational unstable scale of this case according to Tomisaka (2014). In Tomisaka (2014), the maximum mass per unit length, $\lambda_{\max}$, of a gravitational equilibrium filament perpendicular to the magnetic field B is given as

$$\lambda_{\max} = 0.24 \frac{BR_0}{\sqrt{G}} \tag{2.10}$$

for the limiting case of the magnetic field energy being much larger than the internal gas energy in the filament, where R_0 is the filament radius. The gravitational instability condition of a filament with a width h and with surface density, Σ, is

$$h > h_{\min} = \lambda_{\max}/\Sigma = 0.24 \frac{BR_0}{\sqrt{G}\Sigma}, \tag{2.11}$$

since λ of this filament is given as $\lambda = h\Sigma$. We estimate the averaged magnetic field, $\langle B \rangle$, and the averaged surface density, $\langle \Sigma \rangle$, of the shocked layer formed in our numerical simulations by using a thick disk region with a radius of 4 pc and

with a thickness of 2.5 pc that can contain the shocked layer. In the Xstrong, Ystrong, and XYstrong models at $t = 1.7$ Myr (a similar epoch at which the small cloud completely penetrates the large cloud), the averaged $\langle B_x \rangle = 11.8$ µG, 16.4 µG, and 15.8 µG, the averaged $\langle B_y \rangle = 10.1$ µG, 25.9 µG, and 21.4 µG, and the averaged surface density is $\langle \Sigma \rangle = 0.018$ g cm^{-2}, 0.015 g cm^{-2}, and 0.016 g cm^{-2}, respectively. We note that $\langle B_x \rangle$ and $\langle B_y \rangle$ in the weak B_0 models are much smaller than in the strong B_0 models, and averaged surface density is $\langle \Sigma \rangle = 0.019$-0.020 g cm^{-2} in the weak B_0 models. Using these values, from equation (2.9), we find that $\langle B_x \rangle$ cannot suppress gravitational instability of the shocked layers in the strong B_0 models. Using $\langle B_y \rangle$ and $\langle \Sigma \rangle$, from equation (2.11) we get $h_{\min}$ as 0.65 pc, 2.0 pc, and 1.6 pc for the Xstrong, Ystrong, and XYstrong models, respectively. These values of $h_{\min}$ are less than the typical, lateral size (~ 8 pc) of the shocked layers. We also estimate gravitational instability of the filaments formed in our models. We find five filaments in shocked layers, one filament in each model expect for the Ystrong model, at $t = 1.7$ Myr, and we estimate their $\lambda / \lambda_{\max}$. The width of filaments in the Xstrong, XYstrong, Xweak, Yweak, and XYweak are 0.2, 0.6 pc, 0.3 pc, 0.3 pc, and 0.3 pc, respectively, and their line masses, λ, estimated using surface density and the width of the filaments are 16 $M_\odot$ pc^{-1}, 48 $M_\odot$ pc^{-1}, 30 $M_\odot$ pc^{-1}, 28 $M_\odot$ pc^{-1}, and 28 $M_\odot$ pc^{-1}, respectively. The critical line masses, $\lambda_{\max}$, for these filaments are estimated from the magnetic field threading the filaments and the width of the filaments, and the $\lambda / \lambda_{\max}$ for these filaments are 4.6, 1.6, 26.7, 8.9, and 5.9, respectively. Since $\lambda_{\max} < \lambda$, the filaments are gravitationally unstable. This suggests that the shocked layers are gravitationally unstable in all models and that a typical mass of a fragment formed by the gravitational instability is $\Sigma h_{\min}^2$, which is much larger than masses of dense cores formed in the early stage of the collisions of clouds. From the discussion, the main effects of magnetic fields on the CCCs are the suppression of the NTSI and the increase of the thickness of the shocked layers formed in the strong B_0 models, as shown in Section 2.3.

We estimate the magnetic field strength B_0 that can suppress NTSI in the shocked layer from our simulation results. We can expect a magnetic field suppression effect on the NTSI, if

$$\frac{B^2}{8\pi\lambda} > \rho \frac{(\Delta v)^2}{\lambda}, \tag{2.12}$$

where B and ρ are magnetic field strength and gas density, respectively, in the shocked layer, λ is the typical scale of the NTSI, and Δv is the perturbed velocity induced by the NTSI. If the magnetic pressure enhanced by the shock compression is dominant in the shocked layer, we can expect

$$\rho_0 v_{\mathrm{sh}}^2 \sim B^2 / 8\pi, \tag{2.13}$$

$$\rho = \rho_0 B / (\alpha B_0), \tag{2.14}$$

and

$$\rho v = \rho_0 v_{\text{sh}} \tag{2.15}$$

from the MHD shock-wave condition in the rest frame of the shock front, where v_{sh} and v are pre-shock and post-shock gas velocities, respectively, and αB_0 and ρ_0 are pre-shock parallel component of the magnetic field to the shock front and gas density, respectively. Here, α is an enhancement factor of the parallel component of the magnetic field to the shock front induced by the turbulent motion in the clouds before the collision.

The suppression condition of NTSI can be given as

$$B_0 > \frac{\sqrt{8\pi\rho_0}v_{\text{sh}}}{\alpha} \left(\frac{\Delta v}{v_{\text{sh}}}\right)^2 \tag{2.16}$$

from equation (2.12), using equation (2.13) and equation (2.14). If $\Delta v/v_{\text{sh}} \sim 0.2$ and $\alpha \sim 1$, we have

$$B_0 > 1.92 \left(\frac{\rho_0}{3.67 \times 10^{-22} \text{ g cm}^{-3}}\right)^{0.5} \left(\frac{v_{\text{sh}}}{5 \text{ km s}^{-1}}\right) \mu G. \tag{2.17}$$

Here, we assume that v_{sh} is roughly half of the collision speed. This estimated value is consistent with our numerical results, since the strong B_0 is much larger than this value and the weak B_0 is much less than this value.

If the magnetic field pressure is dominant in the shocked layer compared to the effects of the turbulent motions and the thermal gas, we estimate magnetic field strength, B, and gas density, ρ, in the shocked layer as,

$$B = 48.0 \left(\frac{\rho_0}{3.67 \times 10^{-22} \text{ g cm}^{-3}}\right)^{0.5} \left(\frac{v_{\text{sh}}}{5 \text{ km s}^{-1}}\right) \mu G \tag{2.18}$$

and

$$\rho = 4.39 \times 10^{-21} \left(\frac{\rho_0}{3.67 \times 10^{-22} \text{ g cm}^{-3}}\right)^{1.5}$$

$$\times \left(\frac{v_{\text{sh}}}{5 \text{ km s}^{-1}}\right) \left(\frac{\alpha B_0}{4 \ \mu G}\right)^{-1} \text{ g cm}^{-3} \tag{2.19}$$

using equation (2.13) and equation (2.14).

After the whole small cloud penetrates the shocked layer, the shocked layer will change its structure in the free-fall timescale of the shocked layer ~ 1 Myr, since the ram pressure by the small cloud gas does not push the shocked layer after the whole small cloud penetrates the large cloud. In this stage, dense core formation and core mass evolution proceed to form massive bound cores in the timescale of t_{ff}, as shown in Section 2.3.2. We thus propose that if the shocked layer moves out of the large cloud in less than t_{ff} after the whole small cloud penetrates, then such massive dense core formation will not proceed. We have

adopted a collision speed of 10 km s^{-1} in this study.

We briefly discuss the consequences of a higher collision speed, since the observed collision speeds are in the range of 10 to 20 km s^{-1} (Fukui et al., 2018b). If we assume the collision speed of 20 km s^{-1}, v_{sh} = 10 km s^{-1}, then the condition of suppression of NTSI will be

$$B_0 > 3.84 \left(\frac{\rho_0}{3.67 \times 10^{-22} \text{ g cm}^{-3}} \right)^{0.5} \left(\frac{v_{sh}}{10 \text{ km s}^{-1}} \right) \text{ µG} \qquad (2.20)$$

from equation (2.17). This result indicates that stronger B_0 than that used in this study is required to suppress the NTSI. The free-fall time of the shocked layer is $t_{ff} \sim 0.7$ Myr for the collision speed of 20 km s^{-1}. If the penetration time of the small cloud is

$$t_{\text{penetration}} = \frac{2R_{\text{small}}}{v_{sh}} \sim 0.7 \text{ Myr} \qquad (2.21)$$

and the crossing time of the small cloud to the large cloud is

$$t_{\text{cross}} = \frac{2R_{\text{large}}}{v_{sh}} \sim 1.4 \text{ Myr}, \qquad (2.22)$$

t_{cross} is comparable to sum of $t_{\text{penetration}}$ and t_{ff}. This means that larger cloud sizes of the large cloud are needed to induce massive dense core formation. We focus on this scenario of high-speed collision and also larger cloud sizes in next Chapter 3. In our galaxy, various sizes and masses of GMCs are observed. Magnetic field strength depends on location in our galaxy (Beck, 2015). We will extend our study to a higher collision speed case with larger cloud sizes and stronger magnetic fields in our future works. We will study protostar formation and stellar feedback effects on massive star formation by CCCs, using sink particles in our future works.

2.5 Summary

We have performed magnetohydrodynamic simulations of the cloud-cloud collision to study the role of the magnetic field on massive dense core formation in the colliding clouds. We selected two clouds with masses of 972 $M_\odot$ and 7774 $M_\odot$ with the typical density of giant molecular clouds and with internal turbulence such that the clouds are in the virial equilibrium. Two cases of uniform magnetic field strengths, B_0 = 4.0 µG (strong) and 0.1 µG (weak), and three cases of uniform magnetic field directions, parallel, perpendicular, and oblique to collision axis, were studied. Magnetic fields were modified by internal turbulent motion in the clouds. The distribution of magnetic field strength and gas density in the clouds in the strong B_0 model is consistent with the relation observed by Crutcher et al. (2010). The small cloud is given a collision speed of 10 km s^{-1} after the turbulent

magnetic field generation in the clouds. We have also simulated the evolution of the isolated clouds with the same uniform magnetic field strengths as in colliding clouds for comparison. Our main conclusions are as follows.

1. In the weak B_0 models, quasi-periodic shifts with small size appear in the shocked layer formed by cloud-cloud collision and develop with time. The quasi-periodic spatial shifts should be caused by nonlinear thin shell instability. Dense cores are formed at the extremes of the shifts. In the strong B_0 models, such shifts are suppressed by the stronger magnetic field, and a greater number of massive dense cores greater than 10 $M_\odot$ are formed than in the weak B_0 models. The number of massive bound cores in which self-gravitational energy dominates over turbulent energy and magnetic field energy is also mostly larger than in the weak B_0 models. In the massive bound cores with more than 10 $M_\odot$, we can expect massive star formation, since the free-fall time of these cores is less than 0.3 Myr. In isolated cloud models, the bound cores form earlier and are less massive than the colliding clouds models. Since their masses are less than 3 $M_\odot$ and their free-fall times are less than 0.3 Myr, we can expect only intermediate-mass star formation in these cores.

2. The cumulative mass distributions of dense cores formed in our simulation models clearly show that a greater number of massive dense cores are formed in the strong B_0 models than in the weak B_0 models.

3. In the strong B_0 models, massive dense cores distribute in dense gas filaments of which directions are roughly perpendicular to the direction of B_0 except for the Xstrong (strong B_0 parallel to collision axis) model.

4. We give a simple analytic model for the magnetic field strength needed to suppress the instability of the shocked layer formed by colliding clouds and thus suppress low mass core formation. The magnetic field strength is related to collision speed. Testing this model further will be the subject of future works.

Chapter 3

Effect of collision speed on massive core/star formation by CCC

3.1 Chapter highlight

Aim: We perform magnetohydrodynamic simulations of colliding clouds with typical density of molecular clouds to study the effect of high collision speed on massive bound core formation.

Models: We assume two combinations of colliding clouds, Small (7 pc) and Medium (14 pc) clouds, and Small and Large (20 pc) clouds, and collision speeds between 10 and 40 km s^{-1}. The clouds are initially immersed in a uniform magnetic field of 4 µG, and turbulence is generated in them.

Results: In the collision of Small and Medium clouds with 20 km s^{-1}, massive bound cores are hard to form than the 10 km s^{-1} case. In the collision of Small and Large clouds, a greater number of massive bound cores form than that in Small and Medium clouds with 20 km s^{-1}. Longer duration time of the collision in this model than that in Small and Medium clouds explains such massive bound core formation by mass growth due to gas accretion to the dense cores. In the same colliding clouds with higher collision speeds, 30 and 40 km s^{-1}, massive bound core formation is more suppressed with increasing collision speed. Our numerical results show that the collision speed controls massive dense core formation and the collision speed upper limit for massive bound core formation increases with sizes of colliding cloud.

Discussion: We discuss a relation between collision speed and column density of magnetized, colliding clouds for massive bound core formation and compare it with observed relation by Enokiya, Torii, and Fukui (2021).

3.2 Numerical Method and Models

3.2.1 Numerical Method

We use same simulation method as in Sakre et al. (2021) (hereafter Paper I, also presented in Chapter 2). We briefly summarize it here. We use simulation
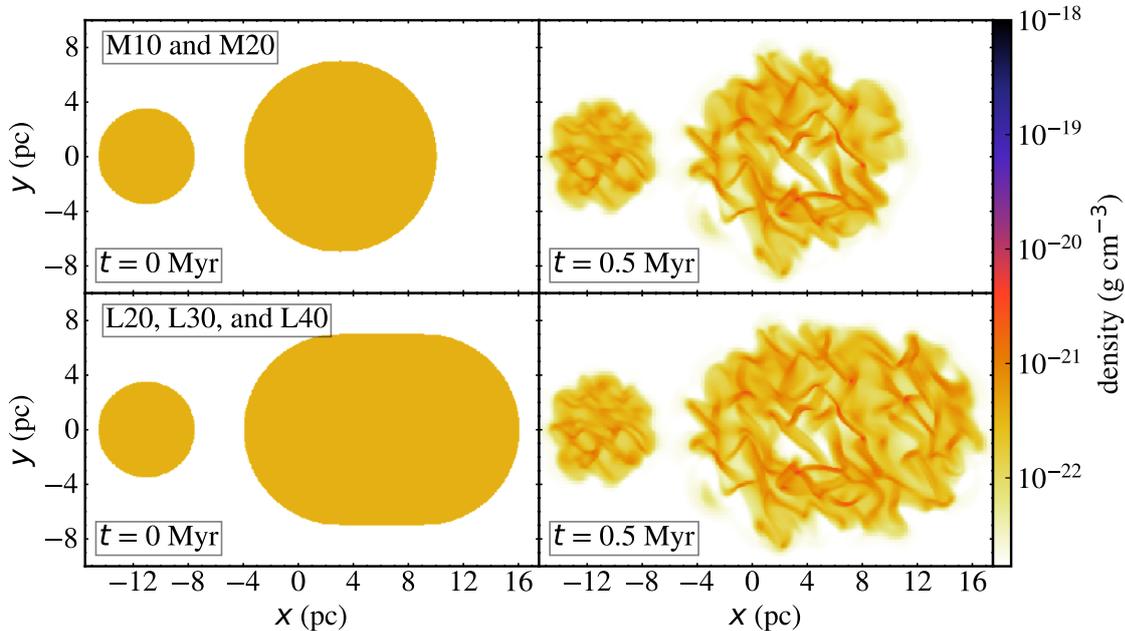
Figure 3.1: Slice plots of the gas density in $z = 0$ pc at $t = 0$ (left) and 0.5 Myr (right) for M10 and M20 in top panels and L20, L30, and L40 in bottom panels. The color bar shows gas density.

code ENZO, a three-dimensional MHD adaptive mesh refinement (AMR) code (Bryan et al., 2014; Brummel-Smith et al., 2019). We assume ideal MHD in our simulations. The code solves the MHD equations using the MUSCL 2nd-order Runge-Kutta temporal update of the conserved variables with the Harten-Lax-van Leer (HLL) method and a piecewise linear reconstruction method (PLM). The hyperbolic divergence cleaning method of Dedner et al. (2002) is adopted to ensure the solenoidal constraint on the magnetic field. We use numerical methods of cooling, the pressure floor, and the Alfvén speed limiter, same as in Paper I. The minimum density in our simulations is selected as the initial density of ambient medium of 1.69×10^{-23} g cm^{-3} (see section 3.2.2).

3.2.2 Cloud Models

Initial clouds and collision setup

We assume two combinations of colliding clouds, which are denoted Small and Medium clouds, and Small and Large clouds as shown in Figure 3.1. We assume an initial state of each cloud based on properties of observed GMCs (Heyer et al., 2009; Murray, 2011), as summarized in Table 1.

Small cloud, Medium cloud, and Large cloud have same uniform density, $\rho_0 = 3.67 \times 10^{-22}$ g cm^{-3}, of which free-fall time is 3.5 Myr. Small and Medium clouds are spherical clouds with radii of 3.5 pc and 7 pc, respectively, as in Paper

Table 3.1: Initial cloud model parameters.

Parameter	Small cloud	Medium cloud	Large cloud	Isolated Medium cloud	Isolated Large cloud	Units
Shape	Sphere	Sphere	Capsule	Sphere	Capsule	-
R^{a}	3.5	7	7	7.25	7.18	pc
H^{b}	-	-	6	-	6.15	pc
M^{c}	972	7774	12803	8566	13595	$M_\odot$
$\rho_0{}^{\text{d}}$	3.67×10^{-22}	3.67×10^{-22}	3.67×10^{-22}	3.67×10^{-22}	3.67×10^{-22}	g cm^{-3}
$t_{\text{ff}}{}^{\text{e}}$	3.5	3.5	3.5	3.5	3.5	Myr
$\sigma_v{}^{\text{f}}$	1	2	2	2	2	km s^{-1}

[a] The radius of sphere for spherical clouds or hemispheres in capsule-shaped clouds.
[b] The height of cylindrical part in capsule-shaped clouds.
[c] The cloud mass.
[d] The cloud initial density.
[e] The free-fall time of the cloud.
[f] The velocity dispersion of the cloud.

I. Masses of Small and Medium clouds are 972 $M_\odot$ and 7774 $M_\odot$, respectively. We assume Large cloud with a larger size along the collision axis (x-axis of the simulation box) to study effect of long duration of collision between the clouds on massive core formation. Large cloud has initially an elongated shape (capsule) consisting of a cylinder with two hemispheres at its both ends. The height of this cylinder is 6 pc, and radii of the two hemispheres are 7 pc. Its symmetric axis is along the collision axis. Mass of Large cloud is 12803 $M_\odot$. The lengths of Medium and Large clouds along the collision-axis are 14 pc and 20 pc, respectively.

We assume initial temperatures of the clouds as 68 K, 273 K, and 273 K for Small cloud, Medium cloud, and Large cloud, respectively. These temperatures provide initial thermal pressures to support those clouds. The dense gas in the clouds rapidly cools down to 10 K due to the radiative cooling during their evolution. These parameters of the clouds are summarized in Table 3.1. The ambient medium has a density of 1.69×10^{-23} g cm^{-3} and a temperature of 800 K. This high density of the ambient medium is used to avoid high Alfvén speeds in the ambient medium.

These clouds are immersed in an initial uniform magnetic field, $\boldsymbol{B}_0$, and turbulence is initially generated in both clouds (see Section 3.2.2). After $t = 0.5$ Myr for their isolated evolution, collision speed is given to Small cloud in direction of other cloud. We call the other cloud the target cloud.

We simulated five CCC models, as shown in Table 3.2. Two additional isolated cloud models are simulated for comparison. For the collision of Small and Medium clouds, we assume collision speeds of 10 and 20 km s^{-1} (M10 and M20). For the collision of Small and Large clouds, collision speeds of 20, 30, and 40 km s^{-1} are assumed (L20, L30, and L40). For isolated clouds, Isolated Medium cloud in IM0 model is a spherical cloud with a total mass of Small and Medium clouds, and Isolated Large cloud in IL0 model is an elongated cloud with similar shape of

Table 3.2: Simulation models.

Model Name	B_0 (µG)[a]	Clouds		v_{coll} (km s^{-1})[b]
		Left	Right	
M10[c]	4.0	Small	Medium	10
M20	4.0	Small	Medium	20
L20	4.0	Small	Large	20
L30	4.0	Small	Large	30
L40	4.0	Small	Large	40
IM0	4.0	-	Isolated Medium	-
IL0	4.0	-	Isolated Large	-

[a] The initial magnetic field strength.
[b] The collision speed given to the left cloud.
[c] Same as the Ystrong model in Paper I, expect some differences in initial velocity field mentioned in main text.

Large cloud with a total mass of Small and Large clouds. Since we want to make clear the effects of collision by comparison with numerical results of the isolated clouds, we assume each isolated cloud with same total mass of corresponding, colliding clouds. For this purpose, we assume same initial density ρ_0 for isolated clouds. Detailed parameters of these isolated clouds are given in Table 3.1. We stop our simulations at $t = 3.1$ Myr, which is earlier than the free-fall time of the clouds (3.5 Myr).

Our simulation domain encompasses (64 pc)^3 with root grids 256^3, and we use four refinement levels based on the condition of minimum baryon mass of 0.05 $M_\odot$ for refinement. This gives the minimum cell size of 0.015 pc at the maximum refinement level.

The details of turbulence and magnetic fields are mentioned in Section 3.2.2. The methods used for the analysis of dense cores are mentioned in Section 3.2.2.

Magnetic field and Turbulence in clouds

After the clouds are initially immersed in a uniform magnetic field, B_0, we develop turbulent motions inside them from $t = 0$ to 0.5 Myr, resulting in turbulent magnetic fields inside the clouds. The strength of initial magnetic field B_0 is assumed to be $B_0 = 4.0$ µG, as in Paper I, since we have shown that turbulent magnetic fields in the turbulent clouds in this choice are consistent with the observed relation between gas densities and turbulent magnetic fields in molecular clouds given by Crutcher et al. (2010). The direction of B_0 is perpendicular (the positive y-axis of the simulation box) to the collision axis. We use this direction of B_0 in all our simulations. This is because we found that the total number of

dense cores more than 10 $M_\odot$ is not so different between models with different directions of $\boldsymbol{B}_0$ in Paper I, although detailed evolution of density structures and dense cores is different between them.

Turbulent velocities are generated to be consistent with the Larson relation (Larson, 1981; Heyer et al., 2009) at $t = 0$ Myr, by imposing a velocity field with power spectrum $v_k{}^2 \propto k^{-4}$. We assume the velocity dispersion, $\sigma_v \sim 1.0$ km s^{-1} for Small cloud and $\sigma_v \sim 2.0$ km s^{-1} for Medium and Large clouds. We use same box which covers the Large cloud and generate turbulent velocity fields. We adapt velocity fields in the target cloud. By this choice we have similar density structures in overlap regions in Medium and Large clouds at $t = 0.5$ Myr, as shown in right panels of Figure 3.1. Since we use different size of the box from Paper I for the turbulence generation, the detailed density structures in the target clouds at $t = 0.5$ Myr are different from Paper I at $t = 0.5$ Myr.

Dense cores

In order to study dense core formation and evolution, we define a dense core by a threshold density, $\rho_{\text{th}} = 5 \times 10^{-20}$ g cm^{-3}, which is in the range of the typical density of observed molecular cores (Bergin and Tafalla, 2007), as in Paper I. We define dense cores by following steps: 1) selection of cells with $\rho \geq \rho_{\text{th}}$ as dense cells, 2) grouping together the neighboring dense cells into a dense core, and 3) exclusion of those groups with cell number less than 27 from dense cores. This minimum cell number condition is used to get a good spatial resolution of dense cores.

Gravitationally bound molecular cores are expected to form stars. We check the gravitational boundness of each dense core by comparing its turbulent energy, E_{turb}, its magnetic field energy, E_{mag}, its thermal energy, E_{ther}, and its self-gravitational energy, E_{grav}. E_{turb}, E_{mag}, and E_{grav} are calculated by equations (2.2), (2.4), and (2.5) in Chapter 2, respectively. Here, we also included E_{ther} in our gravitational boundness estimation. Gravitationally bound molecular cores are expected to form stars. We check the gravitational boundness of each dense core by comparing its turbulent energy, E_{turb}, its magnetic field energy, E_{mag}, its thermal energy, E_{ther}, and its self-gravitational energy, E_{grav}. E_{ther} is given by

$$E_{\text{ther}} = \sum_i \frac{3}{2} m_i c_{s,i}{}^2, \tag{3.1}$$

where i is an index of a dense cell in the dense core, the sum is made over all cells in the dense core, m_i is the mass of the dense cell i, and $c_{s,i}$ is the sound speed of the dense cell i. If $(E_{\text{turb}} + E_{\text{mag}} + E_{\text{ther}}) \leq |E_{\text{grav}}|$, the dense core is gravitationally bound, and we call such a dense core a bound core. Since a dense core is selected by using condition of $\rho \geq \rho_{\text{th}}$, its free-fall time $t_{\text{ff}} \leq 0.3$ Myr. We trace core evolution using similar method as in Takahira, Tasker, and Habe (2014). We modify their method as follows. We increase size of a spherical volume for

searching of the next core position around its predicted position in their method by a factor of 1.75 (see Section 2.1 in their paper for details). We use additional condition that mass of the core in the next time step should be greater than 0.2 times its mass at the previous time step of data-output of which interval is 0.1 Myr. By these modification, we can exclude too small core which is most close to the the predicted position, since we find more massive core in the increased spherical volume in some model.

To make clear a role of accretion in the mass evolution of dense core, we estimate accreted mass to dense core based on Bondi accretion (Bondi, 1952). Following the core evolution, we estimate the mass due to accretion till $(n+1)^{\text{th}}$ simulation time step as

$$M_{\text{acc}} = M_{\text{init, core}} + \sum_{n=1}^{n} \dot{M}_n \Delta t, \tag{3.2}$$

where $M_{\text{init, core}}$ is core mass at formation epoch of the dense core ($n = 1$), Δt is the time interval between the simulation time steps, and $\dot{M}_n$ is accretion rate of the core at n^{th} time step defined by

$$\dot{M}_n = \pi r_{\text{acc}}^2 \sigma_{\text{srr}} \rho_{\text{srr}}, \tag{3.3}$$

where σ_{srr} is the average effective speed given by

$$\sigma_{\text{srr}} = (c_{\text{s, srr}}^2 + \sigma_{\text{1D, srr}}^2 + v_{\text{A, srr}}^2)^{1/2}, \tag{3.4}$$

where $c_{\text{s, srr}}$, $\sigma_{\text{1D, srr}}$, $v_{\text{A, srr}}$, and ρ_{srr} are the mass-weighted averages of sound speed, 1D non-thermal velocity dispersion, Alfvén speed, and density in a volume of a sphere of radius r_{srr} around the core excluding the core volume, respectively. The r_{srr} is calculated from gas properties in a volume surrounding the core. We repeat the following procedure to get r_{srr} and r_{acc}. We use the formula,

$$r_{\text{sph}} = \frac{2GM_{\text{core}}}{\sigma^2} + \langle R \rangle, \tag{3.5}$$

which is sum of the Bondi radius and $\langle R \rangle$ given by equation (2.6) in Chapter 2. First, we get r_{sph} by this equation using σ^2 in the core. Then, we obtain the mean value of σ^2 in a volume of a sphere of r_{sph} outside of the core. Second, we obtain again r_{sph} using the new σ^2. We use the new r_{sph} as r_{srr}. Finally, after we get the mean value of σ^2 in a volume of a sphere of r_{srr} outside of the core, we obtain r_{sph} using the second new σ^2. We use this r_{sph} as r_{acc}. In this procedure, we assume that maximum radius of these spheres is 1 pc.
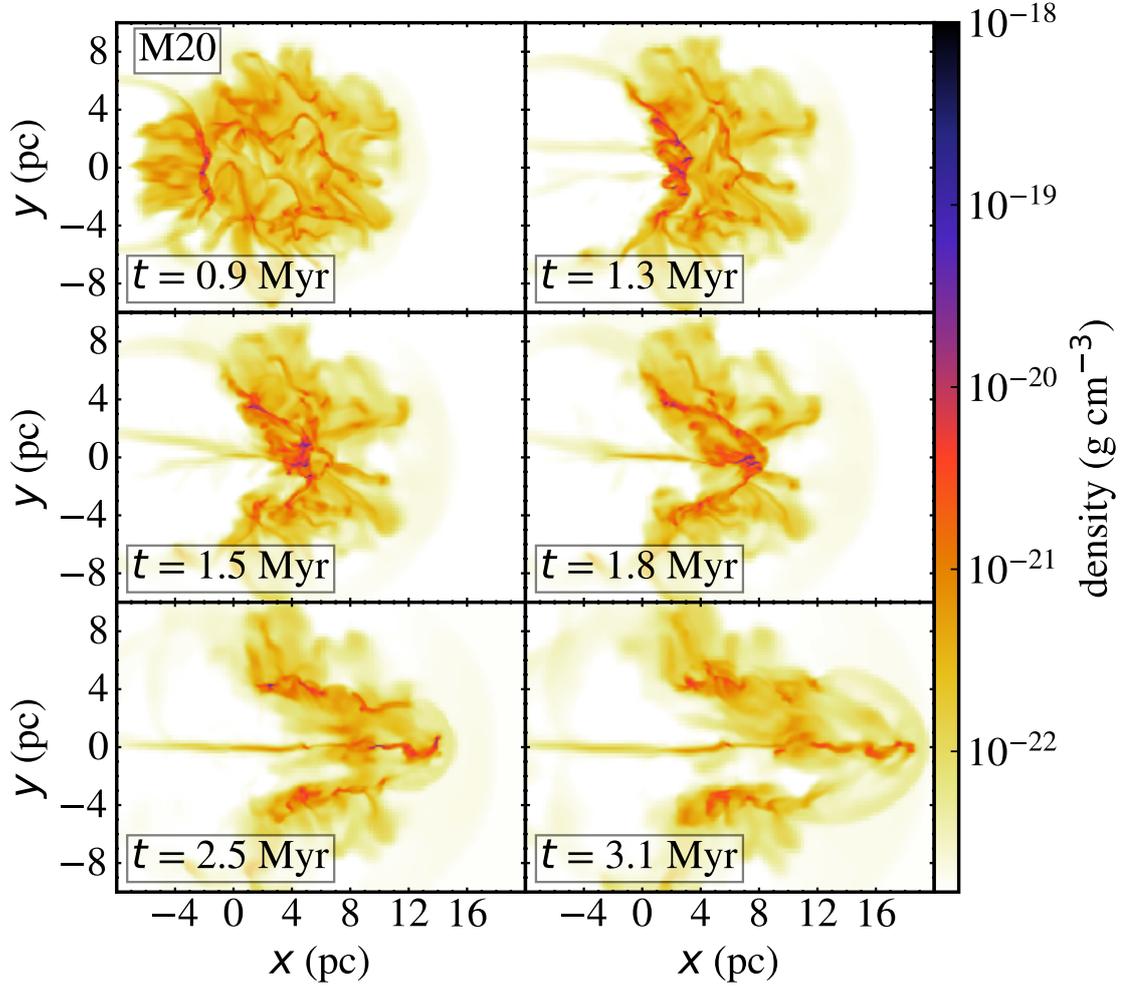
Figure 3.2: Slice plots of the gas density in $z = 0$ pc at $t = 0.9$, 1.3, 1.5, 1.8, 2.5, and 3.1 Myr in M20. The color bar shows gas density.

3.3 Numerical Results

We present simulation results of collision of Small and Medium clouds (M10 and M20) in Section 3.3.1, and those of collision of Small and Large clouds (L20, L30, and L40) in Section 3.3.2. Numerical simulation results of isolated cloud models are given in Appendix C.

3.3.1 Collision of Small and Medium clouds

This section shows simulation results of the collision of Small and Medium clouds. We show results of 20 km s^{-1} collision (M20) in Section 3.3.1. In Section
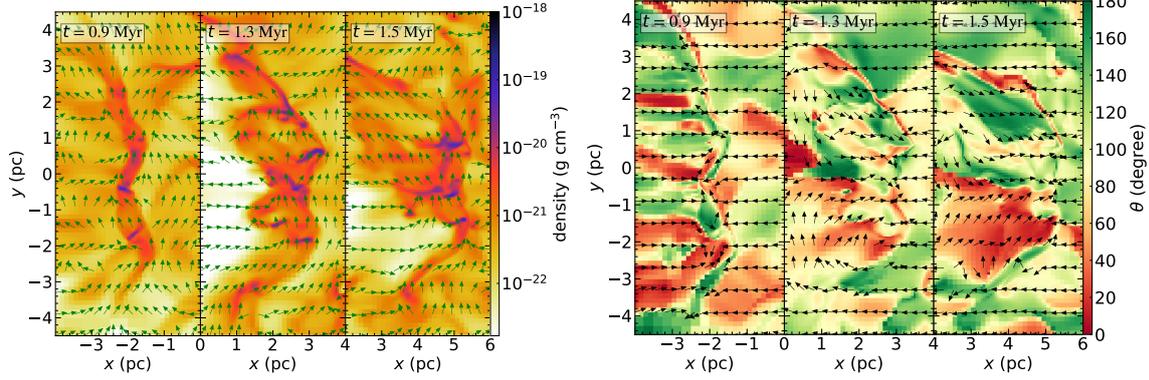
Figure 3.3: Left panels: Slice plots of the gas density in $z = 0$ pc at $t = 0.9$, 1.3, and 1.5 Myr with normalized vectors of magnetic filed directions given by $(B_x, B_y)/\sqrt{B_x^2 + B_y^2}$ in M20. Right panels: Slice plots of θ which is the angle between the magnetic field and the velocity (v_x, v_y, v_z), in $z = 0$ pc at same epochs with unit vectors of $(v_x, v_y)/\sqrt{v_x^2 + v_y^2}$ in M20. The v_x, v_y, and v_z are x-, y-, and z-components of velocity in the frame co-moving with the shocked region, respectively.

3.3.1, we compare M20 with 10 km s^{-1} collision (M10) results. In Section 3.3.1, we compare dense core formation and evolution in both models.

Time evolution of M20

Figure 3.2 shows time evolution of the gas density structures of M20 in which the collision speed is 20 km s^{-1}. The top and middle panels in Figure 3.2 show early stage of the collision at $t = 0.9$ Myr, the shocked region having crossed Small cloud at $t = 1.3$ Myr, the shocked region proceeding in Medium cloud at $t = 1.5$ Myr, and the shocked region near Medium cloud's right edge at $t = 1.8$ Myr.

At $t = 0.9$ Myr, the shocked region formed by the supersonic collision of both clouds is near $x = $ -2 pc and its both sides are two shock fronts (left and right shock fronts). NTSI on scales smaller than 1 pc is well suppressed by the magnetic fields, although the collision speed is twice of Paper I in which we simulated a collision of the same clouds with the collision speed 10 km s^{-1} and with the same initial magnetic field in M20. In Paper I, such spatial shifts are suppressed for $B_0 = 4.0$ µG and develop for $B_0 = 0.1$ µG. Dense structures more than the core threshold density, 5×10^{-20} g cm^{-3}, (hereafter, we call these structures as the high-density gas regions) are formed in the shocked region.

At $t = 1.3$ Myr, Small cloud has completely entered the shocked region leaving a low-density cavity in the left-hand side of the shocked region. Hereafter, we call this epoch as the shock-crossed epoch of Small cloud. Several high-density gas regions are already formed in the shocked region. The shape of the shocked region is roughly arc-like due to the difference in sizes of the colliding clouds. Thickness of the shocked region is still increasing with time after $t = 1.3$ Myr.
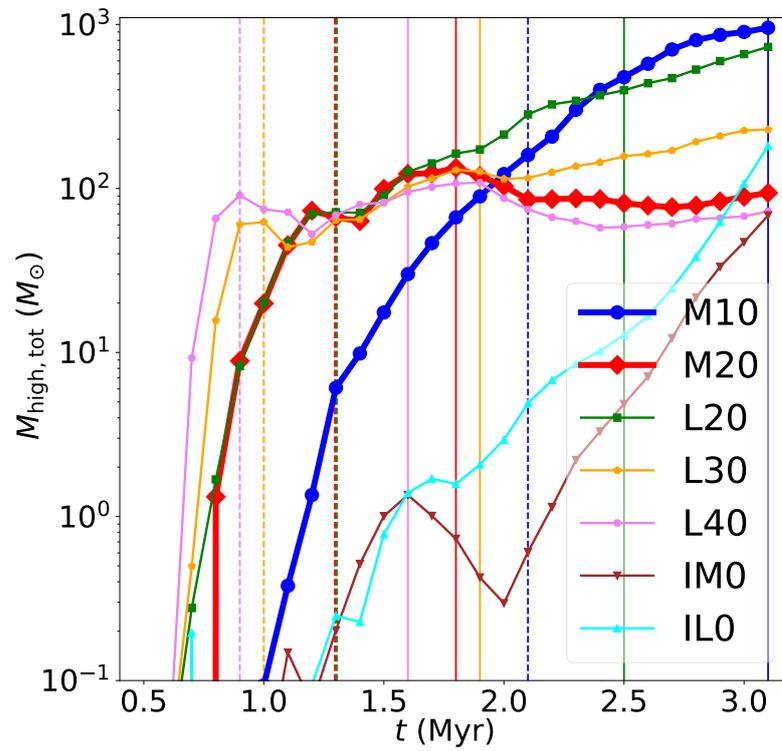
Figure 3.4: Time evolution of total mass of high-density ($> 5 \times 10^{-20}$ g cm^{-3}) gas regions, $M_{\mathrm{high,tot}}$, in all models. The dashed and solid vertical-lines indicate the shock-crossed epochs of Small cloud and target clouds for all CCC models. The dashed vertical-lines for M20 and L20 are overlapped in the early phase.
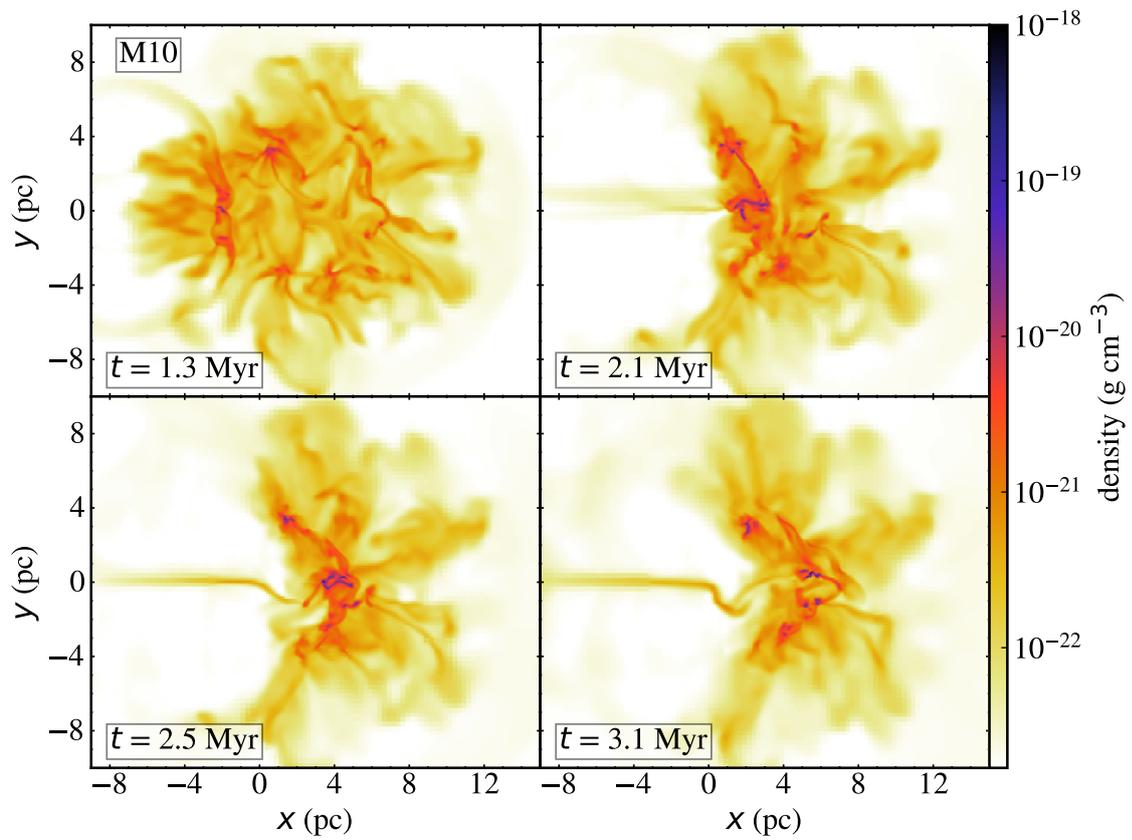
Figure 3.5: Slice plots of the gas density in $z = 0$ pc at $t = 1.3$, 2.1, 2.5, and 3.1 Myr in M10. The color bar shows gas density.

At t = 1.5 Myr, the left-hand side edge of the shocked region is relatively expanding to the negative direction of the x-axis. This is because the ram pressure by Small cloud to the left side of the shocked region disappears after the shock-crossed epoch of Small cloud. Most of the high-density gas regions in the shocked region move toward the collision axis (y = 0 pc). The arc-like structure of the shocked region is more bend than that at t = 1.3 Myr.

At t = 1.8 Myr, the shocked region reaches the right edge of Medium cloud. Hereafter, we call this epoch as the shock-crossed epoch of Medium cloud. A large high-density gas region is formed near the collision axis at this epoch, caused by the accumulation of dense gas regions by gas flow along the magnetic field in the arc-like shocked region, as shown in Figure 3.3.

We show close-up views of magnetic field structures on colormaps of the density in the shocked region at t = 0.9, 1.3, and 1.5 Myr in the left panels in Figure 3.3. We show magnetic field directions with unit vectors defined by $((B_x, B_y)/\sqrt{B_x^2 + B_y^2})$. These panels show that the magnetic fields in the shocked region roughly align with the edge of the shocked region. We show gas flow structures with unit vectors defined by $((v_x, v_y)/\sqrt{v_x^2 + v_y^2})$ in the right panels in Figure 3.3. We also show colormaps of θ which is an angle between magnetic field and velocity (v_x, v_y, v_z) in the right panels to make clear relative directions between them, where v_x, v_y, and v_z are 3D-components of gas velocity in the frame co-moving with the shocked region. These panels show that the gas flow in the shocked region is roughly along the magnetic fields at t = 1.3 and more at t = 1.5 Myr. Figure 3.3 indicates that the magnetic fields in the shocked region bent with deformation of the shocked region, gas is easy to move along the deformed magnetic field lines in the shocked region, and this gas flow helps the accumulation of the high-density gas regions to the collision axis.

The gas flow along the deformed magnetic field lines can be driven by inertial force due to the deceleration of the shocked region. This is estimated as follows. The mass-weighted velocity of the shocked region decelerates with time from 8.6 km s^{-1} at t = 1.3 Myr to 6.5 km s^{-1} at t = 1.5 Myr. From t = 1.3 to 1.5 Myr, this deceleration can drive gas flow along the magnetic field lines, since the magnetic fields in the shocked region are large enough to control the gas flow along the magnetic fields. This flow speed can be estimated as

$$v = (8.6 - 6.5)\cos\theta \text{ km s}^{-1} = 1.4\cos\theta/\cos(\pi/4) \text{ km s}^{-1}, \qquad (3.6)$$

where θ is an angle between the deceleration and the magnetic field. This flow speed is high enough to explain the gas flow that contributes to the accumulation of the high-density gas regions to the collision axis.

The bottom panels in Figure 3.2 show time evolution of the gas density structures after the shock- crossed epoch of Medium cloud. These panels show that the gas in the leading part of the shocked region expands in the ambient medium. At t = 2.5 Myr, the gas expansion already occurs. This expansion begins near the
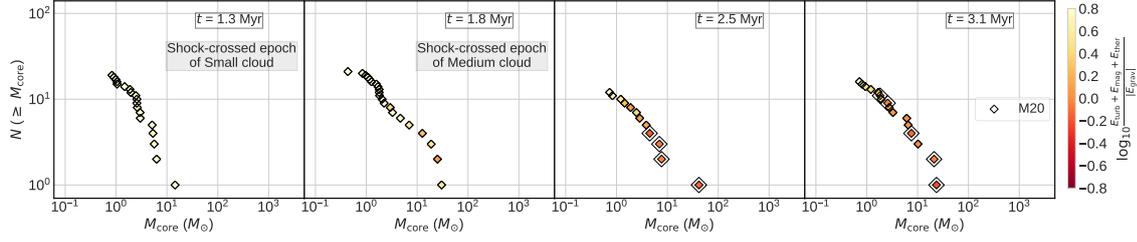
Figure 3.6: Cumulative dense core mass distributions shown by filled diamonds at t = 1.3, 1.8, 2.5, and 3.1 Myr for M20. The color bar in the right-hand side shows the energy ratio of sum of turbulent, magnetic field, and thermal energies to absolute value of self-gravitational energy. The gravitationally bound cores are marked by larger, open diamonds.
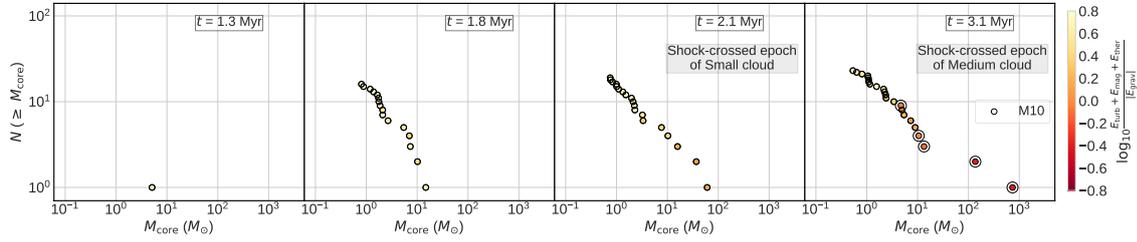

Figure 3.7: Same as in Figure 3.6 but for M10 shown by filled circles at t = 1.3, 1.8, 2.1, and 3.1 Myr.

shock-crossed epoch of Medium cloud and is due to excess magnetic pressure in the shocked region than ram pressure by the ambient medium after the shock-crossed epoch of Medium cloud. The mean magnetic pressure in the shocked region is $\sim 5 \times 10^{-11}$ g cm^{-1} s^{-2} at the shock-crossed epoch of Medium cloud, which is significantly higher than that in the right-hand side of the shocked region. Before the shock-crossed epoch of Medium cloud, the shocked region is confined by the ram pressure by Medium cloud, $\sim \rho_0 v_{\mathrm{sh}}^2 \sim 7 \times 10^{-11}$ g cm^{-1} s^{-2}, which is comparable to the magnetic pressure of the shocked region. After the shock-crossed epoch of Medium cloud, the ram pressure is provided by the ambient medium and is significantly lower than the ram pressure by Medium cloud. This leads to the expansion of the leading part of the shocked region. Details of this expansion and its effects on the dense cores are given in Section 3.3.1.

Figure 3.4 shows the time evolution of the total mass of the high-density regions, $M_{\mathrm{high,tot}}$, in M20 (red thick-line) and the other models. $M_{\mathrm{high,tot}}$ increases with time in M20 until t = 1.8 Myr. After this, change of $M_{\mathrm{high,tot}}$ is small. In this phase, the leading part of the shocked region expands. This indicates that change of the physical state of the shocked region affects evolution of $M_{\mathrm{high,tot}}$.

Comparison of time evolution of M20 and M10

Figure 3.5 shows time evolution of the gas density structures of M10 in which the collision speed is 10 km s^{-1}. Each panel shows the shocked region correspond to the top and middle panels of Figure 3.2 which show numerical results of M20. These figures show that the time evolution of the gas structure is much faster in M20 than that in M10. The swept-up mass by the shock should be similar for the same corresponding positions of the shocked regions in the colliding clouds. However, $M_{high,tot}$ evolves differently in these models as shown in Figure 3.4. We notice that $M_{high,tot}$ is smaller than the swept-up mass. The shock-crossed epochs of Small cloud are shown by dashed lines in Figure 3.4. At these epochs, the swept mass by the shock is estimated to be twice of Small cloud mass, ~ 2000 $M_\odot$. However, $M_{high,tot}$ is much smaller than this value in all colliding models in Figure 3.4. These results indicate that formation of high-density gas regions proceeds more slowly than the mass growth of the shocked region.

In the early stage of the collision (top left panels in Figure 3.2 and Figure 3.5), the shocked region is thinner in M20 than that in M10. This is because of higher ram pressure of the pre-shock gas flows in M20 than M10. At $t = 1.3$ Myr, a greater number of the high-density gas regions are formed in M20 than M10. This is because of higher mass of the shocked region in M20 due to the higher collision speed of clouds than M10 at this epoch.

At the stage of the shock-crossed epoch of Small cloud (top right panels in Figure 3.2 and Figure 3.5), the high-density gas regions are less concentrated towards the collision axis in M20 than in M10. This is because M20 has less time for their concentration to the collision axis than M10. The concentration is driven by the flow along the deformed magnetic fields. A similar difference appears in middle left panel in Figure 3.2 and bottom left panel in Figure 3.5.

At the stage of the shock-crossed epoch of Medium cloud (middle right panel in Figure 3.2 and bottom right panel in Figure 3.5), the high-density gas regions are highly concentrated to the collision axis in both models. However, $M_{high,tot}$ is significantly lower in M20 than M10 at this stage, as shown in Figure 3.4.

$M_{high,tot}$ is much less in M20 than that in M10 (blue thick-line) at the end of the simulation, $t = 3.1$ Myr, as shown in Figure 3.4. $M_{high,tot}$ increases with time until $t = 1.8$ Myr and decreases after this in M20. This mass decrease occurs due to the expansion of the shocked region after $t = 1.8$ Myr in M20, as shown in section 3.3.1. In M10, such expansion of the shocked region does not occur before $t = 3.1$ Myr. We will discuss the reason of the difference in evolution of $M_{high,tot}$ between two models by comparing dense core evolution in both models in the next subsection.
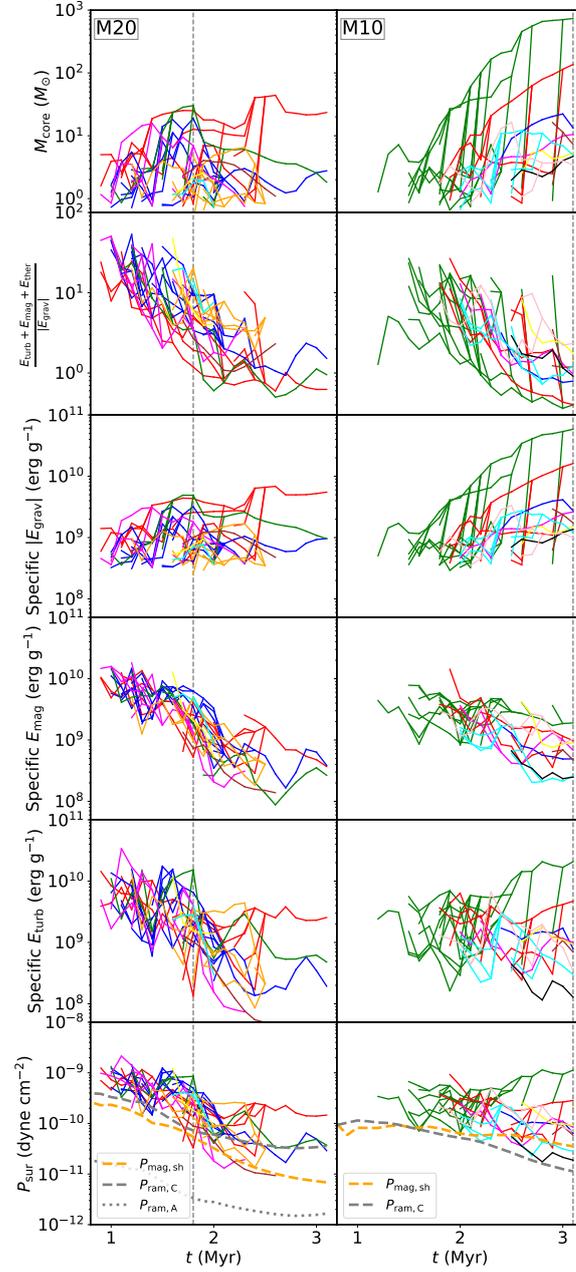
Figure 3.8: Time evolution of masses, the gravitational boundness ratios, the specific self-gravitational, magnetic field, and turbulent energies, and the estimated pressures at the surfaces of massive dense cores which are top ten at the shock-crossed epoch of Medium cloud, where this epoch is $t = 1.8$ Myr in M20 (left panels) and $t = 3.1$ Myr in M10 (right panels). The vertical line shows the shock-crossed epoch of Medium cloud in each model. The details of other thick lines are given in the main text.

Dense core formation and evolution in M20 and comparison with M10

We show cumulative dense core mass distributions (CMDs), $N (\geq M_{\text{core}})$, which is the number of dense cores with mass more than M_{core} as given in equation (2.8 in Chapter 2), at t = 1.3, 1.8, 2.5, and 3.1 Myr for M20 in Figure 3.6. In this figure, the color of filled diamond markers shows the logarithmic value of gravitational boundness ratio defined as $((E_{\text{turb}} + E_{\text{mag}} + E_{\text{ther}})/|E_{\text{grav}}|)$, of which positive (or negative) value indicates that the core is gravitationally unbound (or bound).

The maximum mass of dense cores increases from t = 1.3 Myr to the shock-crossed epoch of Medium cloud, t = 1.8 Myr. Before t = 1.8 Myr, no bound core more than 10 $M_{\odot}$ (hereafter, we call such cores as the massive bound cores) is formed.

After the shock-crossed epoch of Medium cloud, the total number of dense cores and dense cores more than 10 $M_{\odot}$ (hereafter, we call such cores as the massive cores) decreases with time. The total number of dense cores decreases from twenty-one at t = 1.8 Myr to twelve at t = 2.5 Myr, and the number of massive cores decreases from four at t = 1.8 Myr to one at t = 2.5 Myr. These decreases appear during the gas expansion of the leading part of the shocked region which occurs after the shock-crossed epoch of Medium cloud, as shown in bottom panels in Figure 3.2. Since the total pressure of the leading part of the shocked region decreases during this gas expansion, highly unbound massive cores lose their mass as shown later in this subsection.

At t = 3.1 Myr, there are two massive bound cores, as shown in Figure 3.6. We expect formation of a very small number of massive stars in M20. We note that total mass of dense cores agrees well with $M_{\text{high,tot}}$ shown in Figure 3.4, since we use same ρ_{th} for the selection of dense cores and the high-density gas regions.

We show the CMDs for M10 at t = 1.3, 1.8, 2.1, and 3.1 Myr in Figure 3.7 for comparison. One dense core is formed at t = 1.3 Myr, while many dense cores are already formed in M20 at the same epoch, as shown in Figure 3.6. This is because the shocked region accumulates gas faster in M20 than in M10 due to the higher collision speed in M20 than in M10.

At the shock-crossed epoch of Small cloud (t = 1.3 Myr for M20 as shown in Figure 3.6, and t = 2.1 Myr for M10 as shown in Figure 3.7), the number of massive cores is lower in M20 than M10, although the shocked regions contain roughly same mass. This may be due to difference of mass evolution of dense cores in both models.

At the shock-crossed epoch of Medium cloud (t = 1.8 Myr for M20 as shown in Figure 3.6, and t = 3.1 Myr for M10 as shown in Figure 3.7), no massive bound core is formed in M20, whereas four massive bound cores are formed in M10. The maximum mass of dense core is significantly lower in M20 than M10 at this stage. Total mass of dense cores agrees well with $M_{\text{high,tot}}$ in both models.

We examine evolution of dense cores in both models. Figure 3.8 shows time evolution of masses, gravitational boundness ratios, and specific self-gravitational,
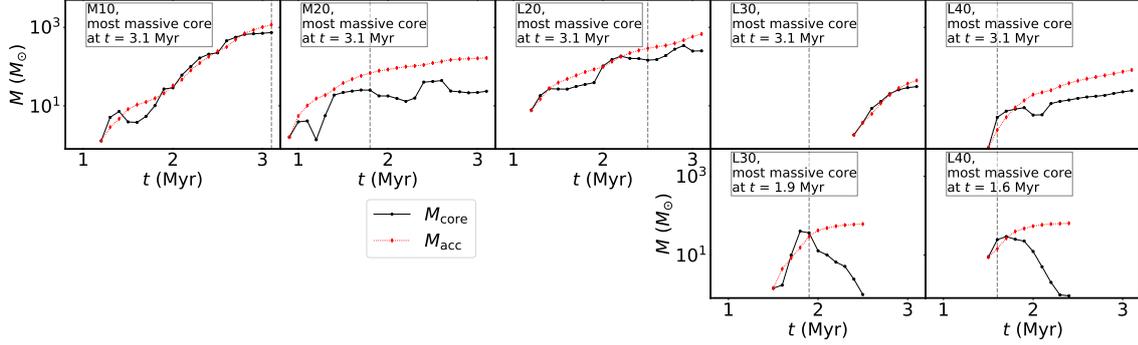
Figure 3.9: Top panels: Mass evolution of the core which is most massive at $t = 3.1$ Myr in all CCC models shown by solid black lines. Bottom panels: Mass evolution of most massive core at the shock-crossed epoch of Large cloud in L30 and L40 shown by solid black lines. The dotted red lines show M_{acc}. The details of this mass estimate are given in the main text. The vertical dashed line shows the shock-crossed epoch of Medium cloud in M10 and M20 and the shock-crossed epoch of Large cloud in L20, L30, and L40.

magnetic field, and turbulent energies of ten most massive dense cores at the shock-crossed epoch of Medium cloud in M20 (left panels) and M10 (right panels). We use same color for lines to show evolution of the cores which finally merge into one core. This figure clearly shows that mass evolution of the cores is very different between M20 and M10. In M20, mass evolution of the cores is suppressed after the shock-crossed epoch of Medium cloud, $t = 1.8$ Myr, and they are gravitationally unbound at $t = 3.1$ Myr, except for cores shown by red lines and green line. In M10, the cores roughly increase their mass with time to $t = 3.1$ Myr, and five cores among them are gravitationally bound at this epoch. Evolution of specific self-gravitational energies of these cores is similar to their mass evolution.

We study the reason for the destruction of cores in M20 by comparing mean magnetic pressure of the shocked region with non-thermal pressure at the surfaces of dense cores estimated by

$$P_{\mathrm{sur}} = ((E_{\mathrm{turb}} + E_{\mathrm{mag}})\rho_{\mathrm{th}})/M_{\mathrm{core}}. \tag{3.7}$$

The bottom panels of Figure 3.8 show P_{sur} of the cores. The dashed orange line shows the mean magnetic pressure of the shocked region, $P_{\mathrm{mag,sh}} = B_{\mathrm{sh}}^2/8\pi$. The dashed and dotted grey lines show typical ram pressures to the shocked region by the cloud medium, $P_{\mathrm{ram,C}} = \rho_0 v_{\mathrm{sh}}^2$, and by the ambient medium, $P_{\mathrm{ram,A}} = \rho_{\mathrm{amb}} v_{\mathrm{sh}}^2$, respectively, where ρ_{amb} is the density of the ambient medium and v_{sh} is mean speed of the shocked region. For these estimations, we select the shocked region as a group of cells with density $> 5\rho_0$ and with a positive x-component of velocity. $P_{\mathrm{mag,sh}}$ is a volume-weighted average quantity, and v_{sh} is a mass-weighted average quantity of the x-component of velocity.

In M20, $P_{\mathrm{mag,sh}}$ is comparable to $P_{\mathrm{ram,C}}$ before the shock-crossed epoch of

Medium cloud. This means that $P_{\mathrm{mag,sh}}$ is dominant to support the shocked region. $P_{\mathrm{mag,sh}}$ decreases faster than $P_{\mathrm{ram,C}}$ after the shock-crossed epoch of Medium cloud. After this epoch, the ram pressure which acts on the leading part of the shocked region changes from $P_{\mathrm{ram,C}}$ to $P_{\mathrm{ram,A}}$ which is much smaller than $P_{\mathrm{ram,C}}$. This decrease of the ram pressure induces the expansion of the leading part and decrease of $P_{\mathrm{mag,sh}}$. The cores which are highly unbound and have P_{sur} higher than $P_{\mathrm{mag,sh}}$ at the shock-crossed epoch of Medium cloud are mostly destroyed. We show this in next paragraph by comparing time evolution of five most massive core at t = 1.8 Myr in M20. In M10, the cores are not destroyed, since the change of $P_{\mathrm{mag,sh}}$ is small.

We compare time evolution of five most massive cores at t = 1.8 Myr in M20 (green, red, blue, red, and pink lines in descending order of core mass). The most massive, third most massive, and fifth most massive cores are highly unbound at t = 1.8 Myr as the gravitational boundness ratio ~ 3.5. These three cores significantly lose their mass from t = 1.8 Myr to 2.0 Myr. The second and fourth most massive cores do not change their mass considerably in this period. These two cores are not highly unbound at t = 1.8 Myr as their gravitational boundness ratio ~ 1.9 and 1.2.

The top, left two panels in Figure 3.9 show mass evolution of the most massive bound core, M_{core}, at t = 3.1 Myr and its estimated accreted mass, M_{acc} (see equation (3.2) in Section 3.2.2 for details) in M20 and M10. We show their evolution from t = 0.9 Myr for M20 and from t = 1.2 Myr for M10. The accreted mass, M_{acc}, well reproduces M_{core} before the shock-crossed epochs of Medium cloud, t = 1.8 Myr in M20 and t = 3.1 Myr in M10. After the shock-crossed epoch in M20, M_{core} becomes smaller than M_{acc}. This indicates that the core losses its mass by the expansion to surrounding region of core. Such evolution of gravitationally unbound cores explains the suppression of total mass evolution of high-density gas regions in M20.

We find that highly unbound cores easily lose their mass and gas accretion to such dense cores is suppressed during expansion of the shocked region. We expect that a target cloud of larger size which is expected to have later shock-crossed epoch of target cloud than M20 will have more time for mass increase of dense cores by accretion. Such a target cloud will favor formation of massive bound cores for 20 km $^{-1}$ collision speed. For the above reason, we simulate the collision between Small and Large clouds, since the shock-crossed epoch of Large cloud is later than that of Medium cloud for the same collision speed. We give the numerical results of collision of Small and Large clouds in Section 3.3.2.

3.3.2 Collision of Small and Large clouds

In this section, we show simulation results of Small and Large, magnetized, colliding clouds. In Section 3.3.2, we show simulation results of 20 km s^{-1} collision speed, L20, and compare it with M20. In Section 3.3.2, we compare formation
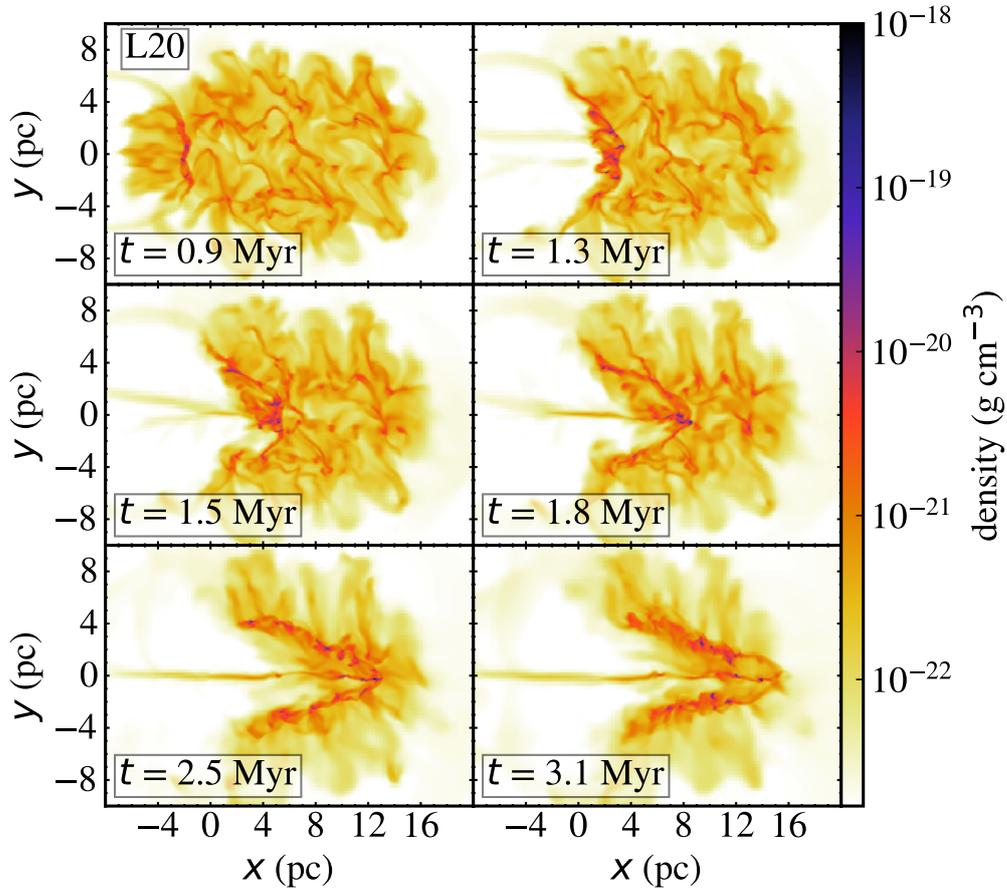
Figure 3.10: Slice plots of the gas density in $z = 0$ pc at $t = 0.9, 1.3, 1.5,$ and $1.8, 2.5,$ and 3.1 Myr in L20. The color bar shows gas density.

and evolution of dense cores in both models. In Section 3.3.2, we show results of 30 km s^{-1} (L30) and 40 km s^{-1} (L40).

Time evolution of L20 and its comparison with M20

Figure 3.10 shows time evolution of the gas density structures of L20. At $t =$ $0.9, 1.3, 1.5,$ and 1.8 Myr, the shocked regions in L20 have similar structures to those at same epochs in M20 (see Figure 3.2). We note that same initial turbulent velocities are used to generate turbulent structures. $M_{\text{high,tot}}$ in L20 is similar to M20 before $t = 1.8$ Myr, as shown in Figure 3.4.

After $t = 1.8$ Myr, $M_{\text{high,tot}}$ monotonically increases with time in L20, while it does not increase with time in M20, as shown in Figure 3.4. This difference is due to different evolution of the shocked regions after $t = 1.8$ Myr. From $t = 1.8$ to 2.5 Myr, the shocked region moves in Large cloud in L20, as shown in Figure 3.10. Mass of the shocked region increases by sweeping up the gas in Large cloud.
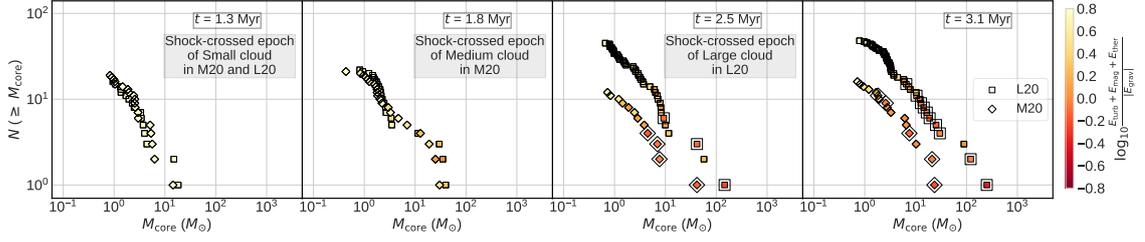
Figure 3.11: Cumulative dense core mass distributions shown by filled squares and diamonds at t = 1.3, 1.8, 2.5, and 3.1 Myr for L20 and M20, respectively. The gravitationally bound cores are marked by larger, open squares and diamonds for L20 and M20, respectively.

In the same period, the shocked region expands and mass evolution of cores is suppressed, since a leading part of the shocked region has already moved in the ambient medium in M20, as shown in Figure 3.2.

At t = 2.5 Myr, several high-density regions are formed in the shocked region in L20. After t = 2.5 Myr, a leading part of the shocked region goes through the right edge of Large cloud. This leads to expansion of the shocked region near Large cloud's right edge. Figure 3.10 shows expansion of the leading part of the shocked region from t = 2.5 Myr to t = 3.1 Myr. In this period, $M_{high,tot}$ still increases with time, as shown in Figure 3.4.

Dense core formation and evolution

Figure 3.11 shows CMDs at t = 1.3, 1.8, 2.5, and 3.1 Myr by filled squares for L20 and diamonds for M20 for comparison. The CMDs in both models are very similar to each other at t = 1.3 and 1.8 Myr. This result is reasonable, since both the models have similar $M_{high,tot}$ till t = 1.8 Myr, as described in Section 3.3.2.

After t = 1.8 Myr, difference of the CMDs between L20 and M20 becomes large. At t = 2.5 Myr, two massive bound cores are formed in L20, whereas there is only one such massive bound core in M20. At t = 3.1 Myr, nine massive bound cores are formed in L20, whereas there are only two massive bound cores in M20. The total number of dense cores in L20 is larger than that in M20 after t = 1.8 Myr.

These differences in the total number of massive bound cores and the total number of dense cores between L20 and M20 can be explained by the different evolution of the dense cores in the shocked regions. The longer time for the dense cores to accumulate gas favors massive bound core formation in L20 than M20.

We explain this using two examples of most massive core at t = 3.1 Myr in L20 and M20 as follows. Time evolution of mass of the core, M_{core}, which is most massive at t = 3.1 Myr can be explained by the estimated accreted mass, M_{acc}, up to the shock-crossed epoch of Large cloud, t = 2.5 Myr, in L20 and up to the shock-crossed epoch of Medium cloud, t = 1.8 Myr, in M20, as shown in top panels in Figure 3.9. Since the shock-crossed epoch of Large cloud in L20 is later than the
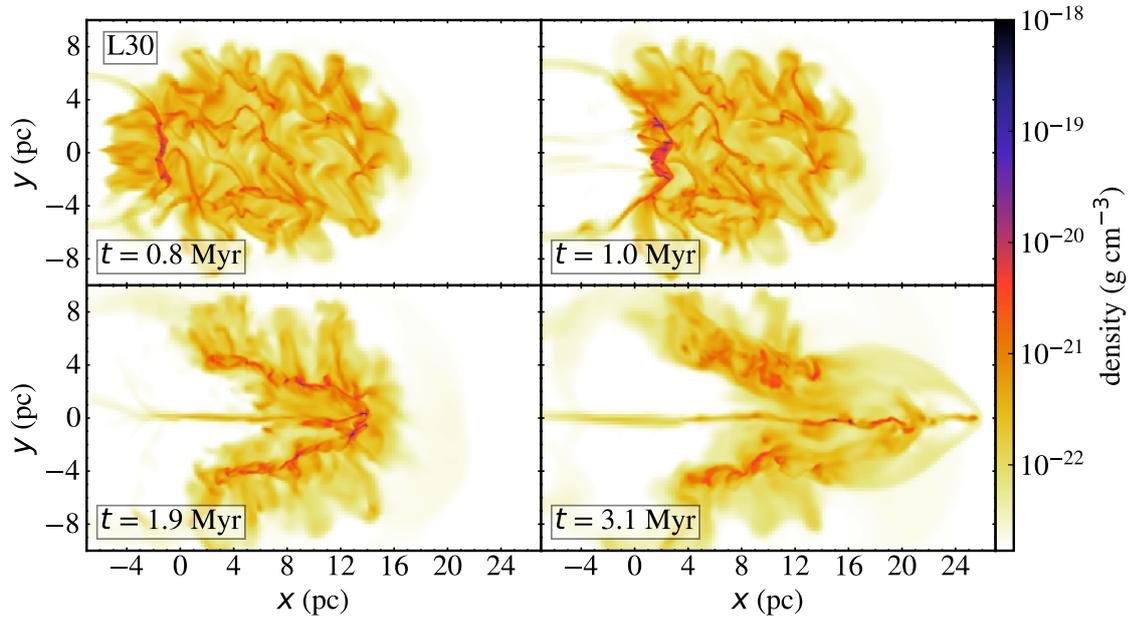
Figure 3.12: Slice plots of the gas density in $z = 0$ pc at $t = 0.8$, 1.0, 1.9, and 3.1 Myr in L30. The color bar shows gas density.
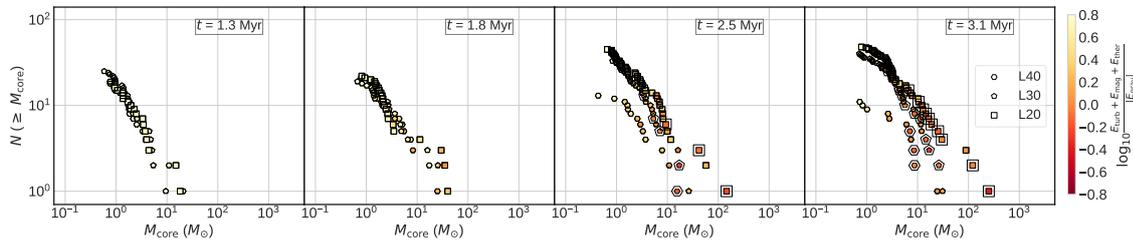

Figure 3.13: Same as in Figure 3.11, but for L40, L30, and L20.

shock-crossed epoch of Medium cloud in M20, dense cores get higher mass by the accretion for a longer time in L20 than that in M20.

We have shown that many massive bound cores form in L20. For the same cloud models, we extend our simulations to more higher collision speeds, 30 and 40 km s^{-1}, to study collision speed limit for massive bound core formation. In next Section 3.3.2, we show results of collisions of Small and Large clouds with these speeds (L30 and L40).

L30 and L40

Figure 3.12 shows time evolution of the gas density structures of L30. The panels in this figure show early stage of the collision between Small and Large clouds at $t = 0.8$ Myr, the shocked region at the shock-crossed epoch of Small
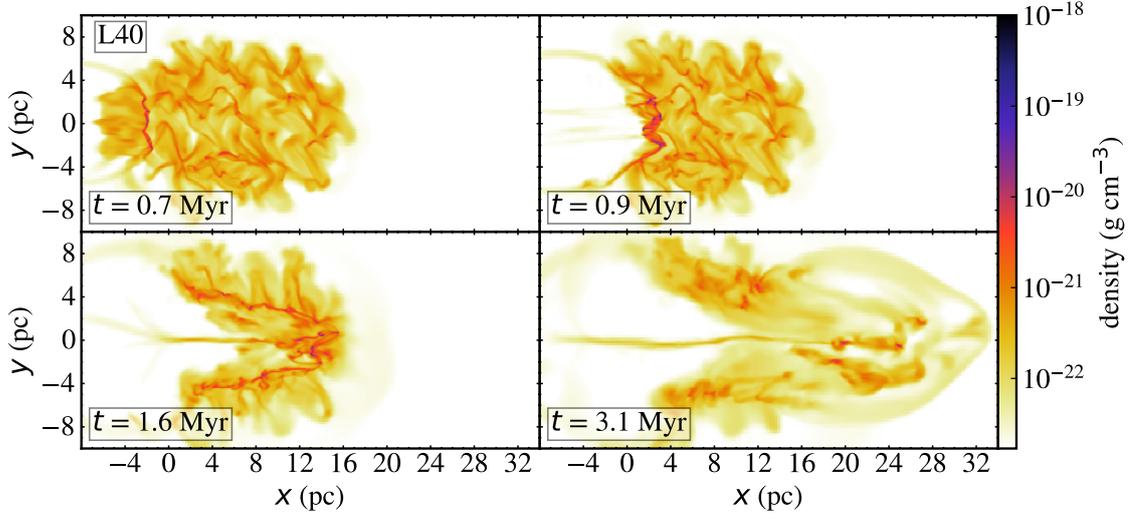
Figure 3.14: Slice plots of the gas density in $z = 0$ pc at $t = 0.7$, 0.9, 1.6, and 3.1 Myr in L40. The color bar shows gas density.

cloud at $t = 1.0$ Myr, the shocked region at the shock-crossed epoch of Large cloud at $t = 1.9$ Myr, and the end of simulation at $t = 3.1$ Myr.

In the early stage of the collision (top left panel in Figure 3.12) and in the stage of the shock-crossed epoch of Small cloud (top right panel in Figure 3.12), the structure of the shocked region is similar to that in the corresponding stages of L20. In those stages, $M_{\text{high,tot}}$ in L30 are similar to those in L20, as shown in Figure 3.4.

In the stage of the shock-crossed epoch of Large cloud (bottom left panel in Figure 3.12), the high-density gas regions in the shocked region are concentrated to the collision axis. $M_{\text{high,tot}}$ in this stage is lower in L30 than that in L20, as shown in Figure 3.4. This difference shows less accumulation of dense gas to the high-density gas regions in L30 than L20. This occurs because of less time in L30 than L20 for the high-density gas regions to accumulate gas by the flow along the deformed magnetic fields.

After the shock-crossed epoch of Large cloud, a leading part of the shocked region moves in the ambient medium and expands. $M_{\text{high,tot}}$ hardly increases in L30, as shown in Figure 3.4. At $t = 3.1$ Myr, the leading part of the shocked region has significantly expanded in the ambient medium, as shown in Figure 3.12. During this expansion, the core which is most massive at the shock-crossed epoch of Large cloud is destroyed, as shown in the bottom left panel in Figure 3.9. The core which is most massive at $t = 3.1$ Myr grows in the non-expanding part of the shocked region. The M_{acc} well reproduces M_{core} of this core, as shown in the top panel in Figure 3.9. This core is not gravitationally bound at $t = 3.1$ Myr. $M_{\text{high,tot}}$ in L30 is much smaller at this epoch than L20, as shown in Figure 3.4.

Figure 3.13 shows CMDs at $t = 1.3$, 1.8, 2.5, and 3.1 Myr in L30 and L20. The

figure shows that CMDs are not so different between these models at $t = 1.3$ and 1.8 Myr. At $t = 2.5$ and 3.1 Myr, the number of massive bound cores in L30 is smaller than that in L20. The massive bound cores formed in L30 are significantly less massive than those in L20. These massive bound cores in L30 are not in the expanding part of the shocked region, and they grow by the accretion.

Figure 3.14 shows time evolution of the gas density structure of L40. In early phase in L40, more high-density regions are formed than in L30, as shown by $M_{high,tot}$ in Figure 3.4. This is due to higher collision speed in L40 than L30. At the shock-crossed epoch of Large cloud, $M_{high,tot}$ in L40 is similar to that in L30, as shown in Figure 3.4. In the stage near the shock-crossed epoch of Large cloud (bottom left panels in Figure 3.14 and Figure 3.12), the shocked region is more dispersed in L40 than L30. This may be due to large irregular motions in the shocked region produced by NTSI by higher collision speed in L40 than L30.

After the shock-crossed epoch of Large cloud, a leading part of the shocked region moves in the ambient medium and expands. Then, $M_{high,tot}$ decreases, saturates later, and is significantly lower than that in L20 and L30 at $t = 3.1$ Myr, as shown in Figure 3.4. The core which is most massive at the shock-crossed epoch of Large cloud decreases its mass with time after that epoch, as shown in the bottom right panel in Figure 3.9. At $t = 3.1$ Myr, there is one massive core formed in the non-expanding part of the shocked region, as shown in the top right panel in Figure 3.9. This core is not gravitationally bound at $t = 3.1$ Myr.

The CMDs show that the number of dense cores and maximum mass of gravitationally bound dense cores are smaller in L40 than L20 and L30 at $t = 3.1$ Myr, as shown in Figure 3.13. These differences become large after the shock-crossed epoch of Large cloud in L40, $t = 1.6$ Myr. This significantly small the number of dense cores in L40 than L30 and L20 may be due to large irregular motion of dense cores. Further discussion on this is given in Section 3.4.1.

3.4   Discussion

3.4.1   Collision speed and target cloud size effects

We have shown that formation of massive ($> 10\ M_\odot$) bound cores is well suppressed in the collision speed of 20 km s^{-1} than 10 km s^{-1} for collision between Small and Medium clouds. The number of dense cores decreases with time in M20 after the shock-crossed epoch of Medium cloud. For the collision speed of 20 km s^{-1}, if we increase the target cloud size from that of Medium cloud to Large cloud, the collision between Small and Large clouds results in a larger number of dense cores than that in the collision between Small and Medium clouds. We discuss the reason why the target cloud size affects the formation of dense cores.

Takahira, Tasker, and Habe (2014) and Takahira et al. (2018) using hydrodynamic simulations demonstrated that the higher collision speed suppresses the mass increase of massive part of CMD in their colliding clouds with no magnetic
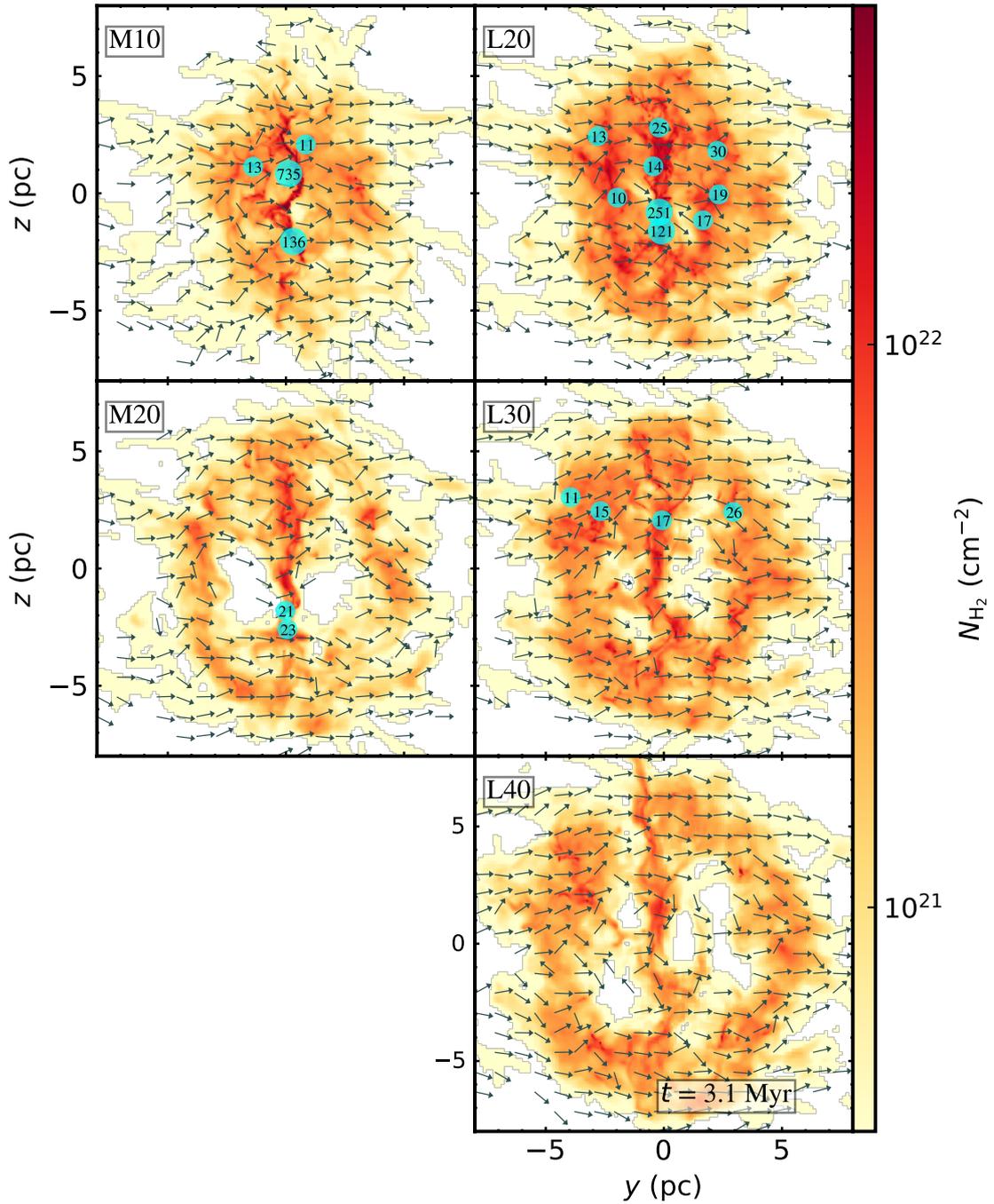
Figure 3.15: H$_2$ column density, N_{H_2}, along the collision axis in the y-z plane at $t = 3.1$ Myr for all CCC models. Markers show positions of massive bound cores and a number on each marker shows its mass in unit of $M_\odot$. Large marker is used for massive bound cores greater than 100 $M_\odot$. The color bar shows the column density and the arrows show unit vectors along the mass-weighted magnetic fields averaged along the collision axis.
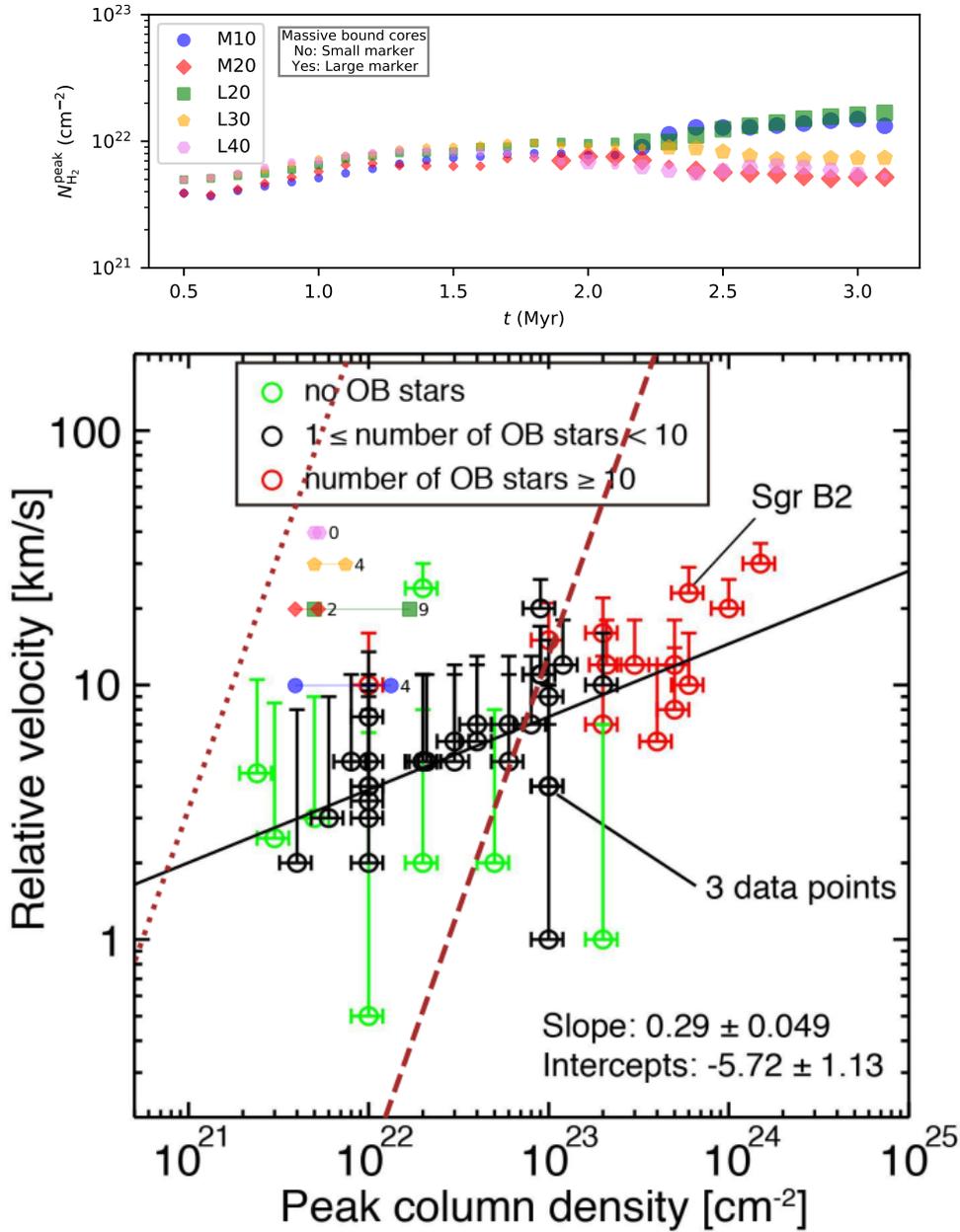
Figure 3.16: Top panel: Time evolution of peak H_2 column density, $N_{H_2}^{peak}$, measured along the collision axis with 1 pc spatial resolution from $t = 0.5$ to 3.1 Myr for CCC models. Larger markers are used for epochs after the massive bound core formation. Bottom panel: $N_{H_2}^{peak}$ and the collision speeds at $t = 0.5$ Myr and the final simulation epoch ($t = 3.1$ Myr) of CCC models with same makers used in the top panel on Figure 9(a) in Enokiya, Torii, and Fukui (2021). The left and right of the same markers shows $N_{H_2}^{peak}$ at $t = 0.5$ and 3.1 Myr, respectively. The total number of massive bound cores at $t = 3.1$ Myr is shown beside the right markers. Analytical conditions given by equation (3.12) are shown by dotted and dashed lines.

field. The suppression of the mass increase is due to a shorter accretion time scale in a higher speed collision for the same colliding clouds. The accretion to dense cores continues, if dense cores remain in the shock region produced by CCC. More massive cores are hard to be decelerated and go through the shocked region earlier than less massive cores. In this way, mass accretion stops earlier for more massive cores than less massive cores. This process produces CMD with a steeper power index of M_{core} in the higher mass part of CMD. We expect that a similar process occurs in M20 and that a higher collision speed of more than 20 km s^{-1} results in suppression of massive bound core formation in the collision of Small and Large clouds.

To study collision speed limit for massive bound core formation in collision of Small and Large clouds, we have simulated their collision with speeds of 30 km s^{-1} (L30) and 40 km s^{-1} (L40). The number of massive bound cores decreases with increasing collision speed, and there are no massive bound cores in L40 at the end of the simulation. Change of CMD mainly appears after the shock-crossed epoch of Large cloud. After the shock-crossed epoch, the leading part of the shocked region moves in the ambient medium, and this part rapidly expands with time due to the small ram pressure by the ambient medium. Total pressure in the leading part decreases due to this expansion. Highly unbound cores in this part disintegrate due to this rapid decrease of the total pressure. Since Takahira et al. (2018) did not show such expansion of the shocked region, this expansion is mainly caused by the magnetic pressure in the shocked region. We confirm this by restarting M20 at the shock-crossed epoch of Medium cloud without magnetic field (not shown in this paper). We see no expansion of the shocked region.

Another possible process in L40 to suppress the mass increase of dense cores is large irregular motions of dense cores in the shocked region. The speeds of irregular motions of dense cores are as high as 10.4, 8.0, and 4.6 km s^{-1} at the shocked-crossed epoch of Small cloud in L40, L30, and L20, respectively. It is possible that such large irregular motions in L40 can disturb the mass growth of dense cores. Such large irregular motions can be due to NTSI. In Paper I, we estimate a magnetic field that can suppress NTSI for a given collision speed. The collision speed in L40 is high enough to overcome the suppression effect of magnetic field of 4 μG on NTSI, as discussed in Paper I.

CCCs with high speeds are suggested in bar regions of barred galaxies. Fujimoto, Tasker, and Habe (2014) and Fujimoto et al. (2020) have shown via galaxy-scale simulations in a barred galaxy that a large fraction of colliding clouds in the bar region has higher collision speeds of more than 30 km s^{-1}. They pointed out that CCCs with such high collision speeds can explain the low star formation efficiency observed in the bar regions in some barred galaxies (e.g., (Momose et al., 2010; Maeda et al., 2021)), if massive star formation is suppressed in CCCs with high collision speeds due to suppression of massive bound core formation, which is demonstrated by hydrodynamic simulations in Takahira, Tasker, and

Habe (2014) and Takahira et al. (2018) and also by MHD simulations in this paper.

We apply the least square fits using equation (2.8) to the CMDs of massive cores at $t = 3.1$ Myr for all CCC models except L40 which has only one massive core. The power index of core mass function, γ, is ~ 1.3 in M10, ~ 2.0 in M20, ~ 1.7 in L20, and ~ 2.7 in L30. The γ increases with the collision speed for the same combination of colliding clouds. This tendency is similar to hydrodynamic simulation results of CCC performed by Takahira et al. (2018). It should be noted that for same collision speed, 20 km $^{-1}$, γ decreases with an increase in cloud size, as $\gamma \sim 2.0$ in M20 and $\gamma \sim 1.7$ in L20. $\gamma \sim 1.7$ is observed for molecular clumps in molecular clouds (Offner et al., 2014).

We show maps of H_2 column density, N_{H_2}, viewed along collision axis with markers at the positions of massive bound cores and with unit vectors of the magnetic fields at $t = 3.1$ Myr in all CCC models in Figure 3.15. We show the core mass in the unit of $M_\odot$ by a number on each marker. Here we exclude gas less than ρ_0 and assume particle number ratio of H_2 to He atoms of 4.7 (i.e., mean molecular weight $\mu = 2.35m_H$) in the calculation of column density. Here we assume that molecular clouds are dominated by H_2. In all CCC models, there are major filaments roughly parallel to the z-axis near $y = 0$ pc, and they are perpendicular to the initial magnetic fields. In M10 and L20, very massive bound cores greater than 100 $M_\odot$ are spatially associated with these filaments. The magnetic field structures are shown by unit vectors which show directions of magnetic fields averaged by mass-weighted in the direction of the collision axis. The magnetic field directions are roughly perpendicular to the filaments in all CCC models.

We compare the results of CCC models with isolated cloud models (IM0 and IL0) shown in Appendix C. CMDs in the isolated cloud models show that the formation of massive bound cores in those models is later and less effective than M10 and L20.

3.4.2 Comparison with Enokiya, Torii, and Fukui (2021) observational result

We have demonstrated that there is an upper threshold of collision speed which allows formation of massive bound cores in CCC, and it depends on colliding clouds, Small and Medium clouds and Small and Large clouds. Our simulation results indicate that CCCs with higher collision speeds need a larger size of target cloud for massive bound core formation. These results are similar to the observational results summarised by Enokiya, Torii, and Fukui (2021). They have reported a positive correlation between peak column densities of H_2 observed in colliding clouds with massive star formation and collision speeds of these clouds.

We compare our simulations results with their observational results. We show time evolution of peak H_2 column densities in our numerical results in Figure 3.16. Top panel in Figure 3.16 shows time evolution of peak H_2 column density,

$N_{H_2}^{peak}$, calculated along the collision axis with 1 pc spatial resolution in each CCC model. After massive bound core formation, $N_{H_2}^{peak}$ increases gradually with time in M10 and L20. Bottom panel in Figure 3.16 shows $N_{H_2}^{peak}$ at the epoch when Small cloud starts to move ($t = 0.5$ Myr) and at the final simulation epoch ($t = 3.1$ Myr) for the collision speeds in our CCC models on Figure 9(a) in Enokiya, Torii, and Fukui (2021). We also show the total number of massive bound cores at $t = 3.1$ Myr beside markers of our CCC models. Figure 9(a) in Enokiya, Torii, and Fukui (2021) shows the peak column densities and collision velocities of observed CCCs with colored markers. Maker color shows the number of OB stars observed in the CCCs. They suggested correlation between the peak column densities and collision velocities in observed CCCs. It implies that a collision with a higher relative velocity requires a higher column density to trigger star formation by CCC. Our simulation results show that $N_{H_2}^{peak}$ changes by a factor of 1.4 ~ 3.4 in each CCC model, and larger cloud models have larger $N_{H_2}^{peak}$. For same collision speed, number of massive bound cores increases with $N_{H_2}^{peak}$. The higher speed models for the same colliding clouds reduce number of massive bound cores. This implies that the upper limit of collision speeds of CCCs for massive bound core formation increases with the peak column density. This is similar to Enokiya, Torii, and Fukui (2021), if a massive star is formed in a massive bound core. $N_{H_2}^{peak}$ in our numerical results is consistent with the observed CCCs with small number of OB stars in Enokiya, Torii, and Fukui (2021). CCC simulations that correspond to formation of a larger number of OB stars should be done to understand the correlation given in Enokiya, Torii, and Fukui (2021). For such a numerical simulation, we need more detailed information of observed colliding clouds which show formation of massive star clusters, e.g., masses and sizes of colliding clouds, their density structures, their inner turbulence, and magnetic fields.

We estimate column density of a shocked layer with massive star formation in colliding clouds. This estimation is for comparison with our CCC models and with the observed correlation which can be approximated as $N_{obs} \propto v_0^{3.4}$ shown in Enokiya, Torii, and Fukui (2021).

Gravitational unstable condition of the shocked layer induced by CCCs is proposed as,

$$\frac{l}{v_1} > \sqrt{\frac{3\pi}{32G\rho_2}}, \tag{3.8}$$

where l is a typical scale of clouds swept by a shock induced by CCC, v_1 is collision velocity of CCC, and ρ_2 is density of the shocked layer. In this equation, we assume that duration of collision should be longer than the free-fall time of the shocked layer to be gravitational unstable. We assume a simple shock condition

as

$$\rho_1 v_1^2 = \frac{B_2^2}{8\pi}, \tag{3.9}$$

where ρ_1 is gas density of the clouds before the collision and B_2 is a magnetic field in the shocked layer and is assumed to dominate pressure in the shocked layer. B_2 is simply given as

$$B_2 = B_1 \left(\rho_2 / \rho_1 \right) \tag{3.10}$$

for one dimensional compression of magnetic field, B_1, perpendicular to the shocked layer, where B_1 is magnetic field in the preshock gas. From equations (3.8), (3.9), and (3.10), we estimate minimum column density required for gravitational instability of shocked layer as

$$N = \rho_1 l > \sqrt{\frac{3\pi B_1 v_1 \sqrt{\rho_1}}{32 G \sqrt{8\pi}}}. \tag{3.11}$$

From this, we have

$$N_{\mathrm{H}_2} > 1.7 \times 10^{21} \left(\frac{v_1}{10 \ \mathrm{km \ s^{-1}}} \right)^{0.5} \left(\frac{B_1}{4 \ \mu\mathrm{G}} \right)^{0.5}$$
$$\times \left(\frac{\rho_1}{3.67 \times 10^{-22} \ \mathrm{g \ cm^{-3}}} \right)^{0.25} \mathrm{cm^{-2}}. \tag{3.12}$$

This equation shows a column density of the gravitational unstable shocked layer is larger than the threshold value that is proportional to $v^{0.5}$, $\rho_1^{0.25}$, and $B_1^{0.5}$. This is a necessary condition for massive star formation. This should be a condition for bound core formation. Massive stars may form in the shocked layer which satisfy this condition. Further condition is needed for formation of massive bound core. The dotted line in Figure 3.16 shows this condition given by equation (3.12), using values of ρ_1 and B_1 same as the initial values in our clouds. Our results are consistent with this condition, since bound cores are formed in all CCC models. The observed CCCs by Enokiya, Torii, and Fukui (2021) satisfy the condition of equation (3.12). The observed colliding clouds in the range of high peak column density in Figure 3.16 are found in the galactic central region where observed clouds have higher magnetic field strengths and higher gas densities than our initial cloud models (Mangilli et al., 2019; Mills, 2017). The dashed line in Figure 3.16 shows the condition given by equation (3.12) for higher values of ρ_1 and B_1 as $100\rho_0$ and 1 mG which correspond to the observed values in molecular clouds in the galactic central region. This condition is well consistent with the observed colliding clouds in the range of high peak column density. Further study using colliding cloud models similar to the observed ones in the galactic central region is needed to understand the observed correlation given by Enokiya, Torii, and Fukui (2021).

3.4.3   Future works

We plan on extending our simulations to CCCs with higher column density and with stronger magnetic fields. Enokiya, Torii, and Fukui (2021) reported that higher peak column densities than our simulation models are observed in colliding clouds which associate with super star clusters and active star formation regions in the central region of our Galaxy. It is interesting to study how many massive stars can be formed by CCCs with observed high peak column density. Since strong magnetic fields of the order of 1 mG are estimated in the observed molecular clouds in the central molecular zone of our Galaxy (Mangilli et al., 2019), the effect of such a strong magnetic field on massive star formation process by CCCs should be investigated.

In this paper, we do not consider feedback effects by newly formed massive stars by CCCs. Such stellar feedback should affect core formation during CCC. Hydrodynamic simulations of CCCs with the stellar feedback by photoionization were performed by Shima et al. (2018), and they show that the feedback can promote massive star formation during CCCs. Stellar feedback should be considered in MHD simulation, since the massive star formation is observed in several CCCs in the central regions of our Galaxy where magnetic fields are very strong. We will address this in our future papers.

3.5   Summary

We have performed magnetohydrodynamic simulations of the cloud-cloud collision to study the effect of high-speed collisions on massive dense core formation in the magnetized, colliding clouds. We assumed two combinations of colliding clouds, Small and Medium clouds, and Small and Large clouds, with the typical density of giant molecular clouds and with the internal turbulence. The clouds are immersed in the uniform magnetic field of $B_0 = 4.0$ μG perpendicular to the collision axis. The magnetic fields are modified by the internal turbulent motion in the clouds. The collision speeds of 10 and 20 km s^{-1} are assumed for Small and Medium clouds (M10 and M20) and 20, 30, and 40 km s^{-1} are assumed for Small and Large clouds (L20, L30, and L40). We have also simulated isolated cloud models with the same uniform magnetic field as in the colliding clouds for comparison. We summarize our numerical results as follows.

1. In M20, massive bound cores are hard to be formed in the shocked region than M10. We find that the dense cores which are highly unbound before the shock-crossed epoch of Medium cloud are destroyed after this epoch during the expansion of the shocked region in the ambient medium, and the accretion to massive cores is suppressed in this stage. In M20, the shock-crossed epoch of Medium cloud is earlier than that in M10. This leads to suppression of massive bound core formation in M20 than M10.

2. We simulate L20, since the shock-crossed epoch of Large cloud is later than that of Medium cloud for $20 \, \text{km s}^{-1}$, and we show that more massive bound cores are formed in L20 than that in M20.

3. In higher-speed collisions of Small and Large clouds ($30 \, \text{km s}^{-1}$ in L30 and $40 \, \text{km s}^{-1}$ in L40), the total number of massive bound cores decreases with an increase in the collision speed, similar to the collisions between Small and Medium clouds (M10 and M20).

4. The massive bound core formation in M10 and L20 is more efficient than that in the isolated cloud models (IM0 and IL0).

5. Our results indicate that the massive bound core formation in colliding clouds with a higher speed requires a higher initial column density of the colliding clouds and that the upper limit on this collision speed depends on column density of colliding clouds. These properties are very similar to observed properties of colliding clouds with OB stars reported by Enokiya, Torii, and Fukui (2021).

Chapter 4

Summary and future work

4.1 Thesis summary

In this thesis, we focused on finding the physical conditions for massive star formation triggered by cloud-cloud collision (CCC). We selected this scenario of CCC due to its importance in triggering massive star formation, as shown by numerous observational evidences. In this scenario, we concentrated on two parameters of magnetic field and collision speed and studied their effects on massive core/star formation.

In Chapter 2, we studied the role of magnetic field on massive dense core formation triggered by CCC. We used uniform magnetic field strengths, B_0 = 4.0 μG (strong) and 0.1 μG (weak), and three cases of uniform magnetic field directions, parallel, perpendicular, and oblique to collision axis. We found the number of massive cores greater than 10 $M_\odot$ and massive, self-gravitationally bound cores in which self-gravitational energy dominates over turbulent energy and magnetic field energy is mostly greater in strong B_0 models than the weak B_0 models. The reason for this is as follows. In the weak B_0 models, quasi-periodic shifts with small size appear in the shocked layer formed by CCC and develop with time. These quasi-periodic spatial shifts should be caused by nonlinear thin shell instability (NTSI). Dense cores are formed at the extremes of the shifts. In the strong B_0 models, such shifts are suppressed by the stronger magnetic field, and a greater number of massive dense cores are formed than in the weak B_0 models. In isolated cloud models, the bound cores form earlier and are less massive than the CCC models. Since their masses are less than 3 $M_\odot$, we can expect only intermediate-mass star formation in these cores. In the strong B_0 models, massive dense cores distribute in dense gas filaments of which directions are roughly perpendicular to the direction of B_0 except for the Xstrong (strong B_0 parallel to collision axis) model.

In Chapter 2, we discussed analytically that higher speed collisions can lead to stronger NTSI and magnetic field should be stronger to suppress such a strong NTSI. In this way, strong NTSI may suppress massive core formation in high-speed collisions. Additionally, recent hydrodynamic simulations and observational survey demonstrated that high-speed collisions cannot produce massive

cores and massive stars. Hence, we simulate high-speed collisions to test this high-speed scenario.

In Chapter 3, we studied the role of collision speed on massive dense core formation triggered by high-speed CCC. We assumed two combinations of colliding clouds, Small and Medium clouds, and Small and Large clouds. The clouds are immersed in the uniform magnetic field of $B_0 = 4.0$ μG perpendicular to the collision axis. In 20 km s^{-1} collision of Small and Medium clouds, massive bound cores are hard to be formed in the shocked region than 10 km s^{-1} case. We find that the dense cores which are highly unbound before the shock cross epoch of Medium cloud are destroyed after this epoch during the expansion of the shocked region in the ambient medium, and the accretion to massive cores is suppressed in this stage. In 20 km s^{-1} case, the shock cross epoch of Medium cloud is earlier than that in 10 km s^{-1} case. This leads to suppression of massive bound core formation in 20 km s^{-1} than 10 km s^{-1} case. We simulate 20 km s^{-1} of Small and Large clouds, since the shock cross epoch of Large cloud is later than that of Medium cloud for 20 km s^{-1}, and show that more massive bound cores are formed in Small and Large clouds than that in Small and Medium clouds. In higher-speed collisions of Small and Large clouds (30 km s^{-1} and 40 km s^{-1}), the total number of massive bound cores decreases with an increase in the collision speed, similar to the collisions between Small and Medium clouds. Our results indicate that the massive bound core formation in colliding clouds with a higher speed requires a higher initial column density of the colliding clouds and that the upper limit on this collision speed depends on a column density of colliding clouds. These properties are very similar to observed properties of colliding clouds with OB stars reported by Enokiya, Torii, and Fukui (2021).

4.2   Future Work

The work presented in this thesis have clear and obvious avenues for extension. In following sections, we discuss our ongoing and future studies that can help us further understand the physical conditions of massive star formation in CCCs.

4.2.1   Stellar feedback effects on massive star formation in CCC

Since CCCs can promote massive star formation, the colliding molecular clouds will be significantly affected by stellar feedback by massive stars, eventually affecting further star formation.

Using hydrodynamic simulations, Shima et al. (2018) showed that feedback by photoionization can promote star formation in CCCs, whereas feedback can eventually suppress star formation in an isolated cloud. This is shown in Figure 4.1, which shows close-up image of the gas around the most massive sink particle
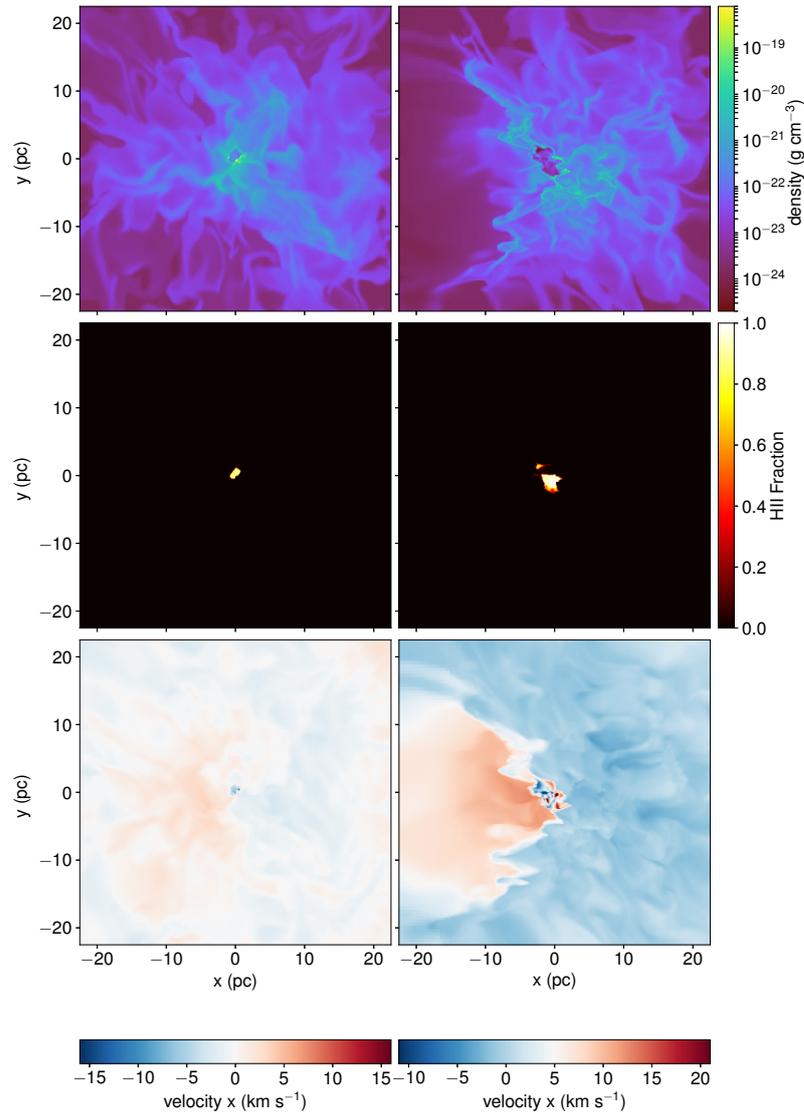
Figure 4.1: (From Shima et al. (2018)) The gas density (top), HII fraction (middle), and x-velocity (bottom) on a slice in the isolated cloud case (left) and 10 km s^{-1} collision case (right). Images are centered around the most massive sink particle a few Myr after it begins to emit radiation. The isolated cloud is shown at 5.2 Myr, while the colliding case is at 3.7 Myr as the sink formation time differs between these runs. The off-set in the velocity colorbar matches the shock propagation speed in the colliding cloud case of 5 km s^{-1}

a few Myr after it has begun to emit radiation. For their isolated cloud case, they found that radiation from the star formation regions counters the gravitational collapse after several Myr, which slows the production of stars and throttles the cloud's star formation efficiency. In their colliding clouds case, they found that

expanding HII region from the massive star clusters is able to keep pace with the shock front as it travels through the cloud, and the dense gas inside the shock front is not dispersed by the radiation, which continues to have a positive impact on the star formation efficiency. However, they did not consider magnetized, colliding clouds.

Using magnetohydrodynamic simulations, we demonstrated in Chapter 2 that magnetic field helps to form many massive cores which are gravitationally bound in magnetized, colliding clouds. This result suggests that a role of the stellar feedback can be highly crucial in magnetized, colliding clouds due to greater number of massive stars than in weakly magnetized, colliding clouds. Hence, it is important to study the role of stellar feedback in magnetized, colliding clouds.

For studying stellar feedback using our current models of colliding clouds, we need to make some changes since in our current simulations we had some critical limitations to venture in this direction. We searched for massive bound cores and simply assumed that a massive star can form in a massive bound core. For implementing stellar feedback in our MHD simulations, we have to use sink particle model and implement stellar feedback. The details of sink particle creation in MHD simulations and gas accretion in those sink particles is mentioned in Appendix D. For stellar feedback by photoionization, we will assume that the sink particle reaching a certain mass threshold (e.g., $> 10\ M_{\odot}$) will emit ionizing radiation of which evolution is calculated by using a ray-tracing scheme implemented in ENZO code (Wise and Abel, 2011). We will assume similar ionizing luminosity and mean photon energy as in simulations by Shima et al. (2018). Other stellar feedback mechanisms, for example, supernovae, will also be implemented.

4.2.2   CCC in extreme conditions

It is interesting to extend my current research to a stronger magnetic field and higher collision speed models, since such situations are expected in inner regions of the Galaxy, especially in the Galactic central region. In such regions, strong feedback is observed, and its role in the massive star formation process should be interesting to study. Such simulations with larger-sized clouds can help us interpret the recent observational survey result by Enokiya, Torii, and Fukui (2021) in which higher-speed collisions require higher column density to form massive stars. Our numerical results in Chapter 3 are consistent with this survey result. However, a wider range of parameter space should be explored for quantitative comparison between simulations and observations and to obtain a better understanding of this observational survey result.

4.2.3   Properties of dense cores in CCC

The structural, magnetic, and, kinetic properties of dense cores in our previously simulated colliding clouds could be useful to other simulators who use
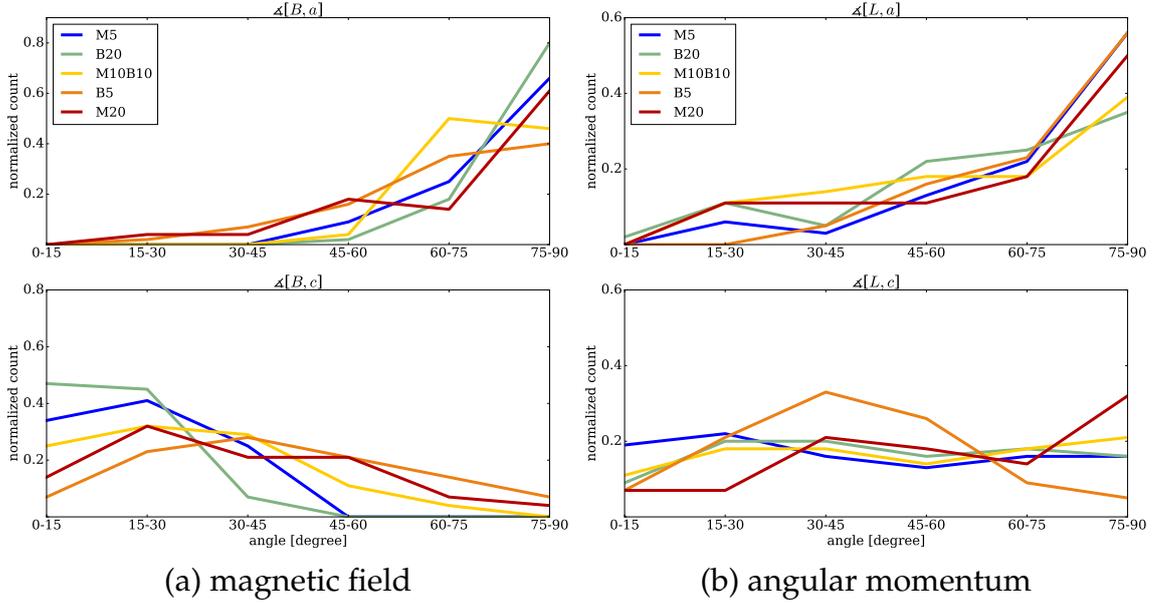
(a) magnetic field (b) angular momentum

Figure 4.2: (From Chen and Ostriker (2018)) Left panels: Histogram of relative orientations between the mean magnetic field and the major (*a*, top) and minor (*c*, bottom) axes of the core. Right panels: The histogram of the relative angle between the net, integrated angular momentum **L** of the core and its major (top) and minor (bottom) axes.

dense core in their initial setup. Dense cores are immediate precursor of stars and binary systems. Their properties can provide initial conditions of star formation and determine the local environment of protostellar disks and outflows. In particular, information on core's magnetic field and core angular momentum could be highly useful. Recently, Chen and Ostriker (2018) calculated these properties of dense cores in their MHD simulations. Left panels in Figure 4.2 shows the histogram of relative orientations between the mean magnetic field and the major (*a*, top) and minor (*c*, bottom) axes of the core. It is clear that the magnetic field preferably aligns perpendicular to the major axis and parallel to the minor axis, especially in models with stronger magnetization (B20) or weaker turbulence (M5). The alignment becomes weaker when the cloud is more perturbed (model M20) or weakly magnetized (model B5). Right panels in Figure 4.2 shows the histogram of the relative angle between the net, integrated angular momentum **L** of the core and its major (top) and minor (bottom) axes. The rotational axis defined by $\hat{\mathbf{L}}$ tends to align perpendicular to the major axis, regardless of the simulation models, but has no preferred direction with respect to the minor axis. We would like calculate similar properties of dense cores formed in simulations in this study.

4.2.4 Comparing CCC observations with simulations

Simulations help test the hypothesis based on observations. We did one such comparison in Fujita et al. (2021). We carried out the hydrodynamic simulation of the oblique collision of clouds for comparison with our observed results of high-mass star formation region which may be triggered by CCC in the Orion molecular cloud. Figure 4.3 shows the position-velocity diagrams of observation and simulation in left and right panels, respectively. We showed good agreement between our simulation results and the observation, as both the panels in the figure show two peaks of density at different velocities, and they are connected by an interface of intermediate velocity. This agreement supports that CCC triggers this high-mass star formation. This example shows the importance of comparing future observations with simulations.

(a) Observation

(b) Simulation
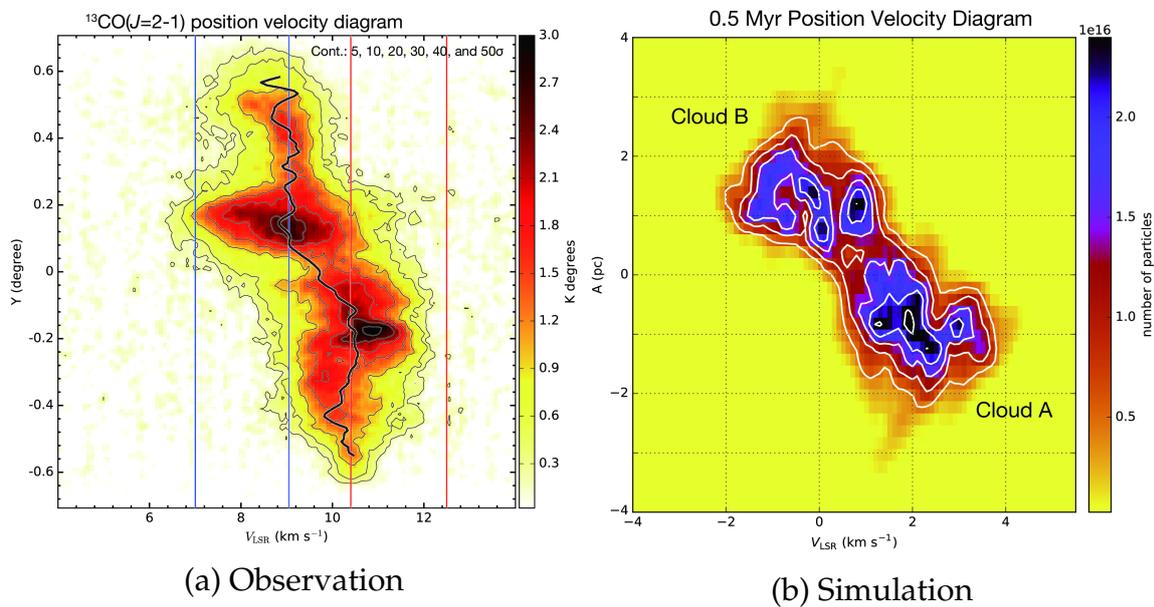
Figure 4.3: (From Fujita et al. (2021)) Left panel: The position-velocity diagram of ^{13}CO(J=2–1) emission toward NGC 2068 and NGC 2071. The black line shows the intensity-weighted mean velocity along the Y-axis at every $30''$. The blue and red lines indicate the integration ranges of two clouds. Right panel: The position-velocity diagram in the simulation at $t = 0.5$ Myr.

Appendix A

Isolated clouds (For Chapter 2)
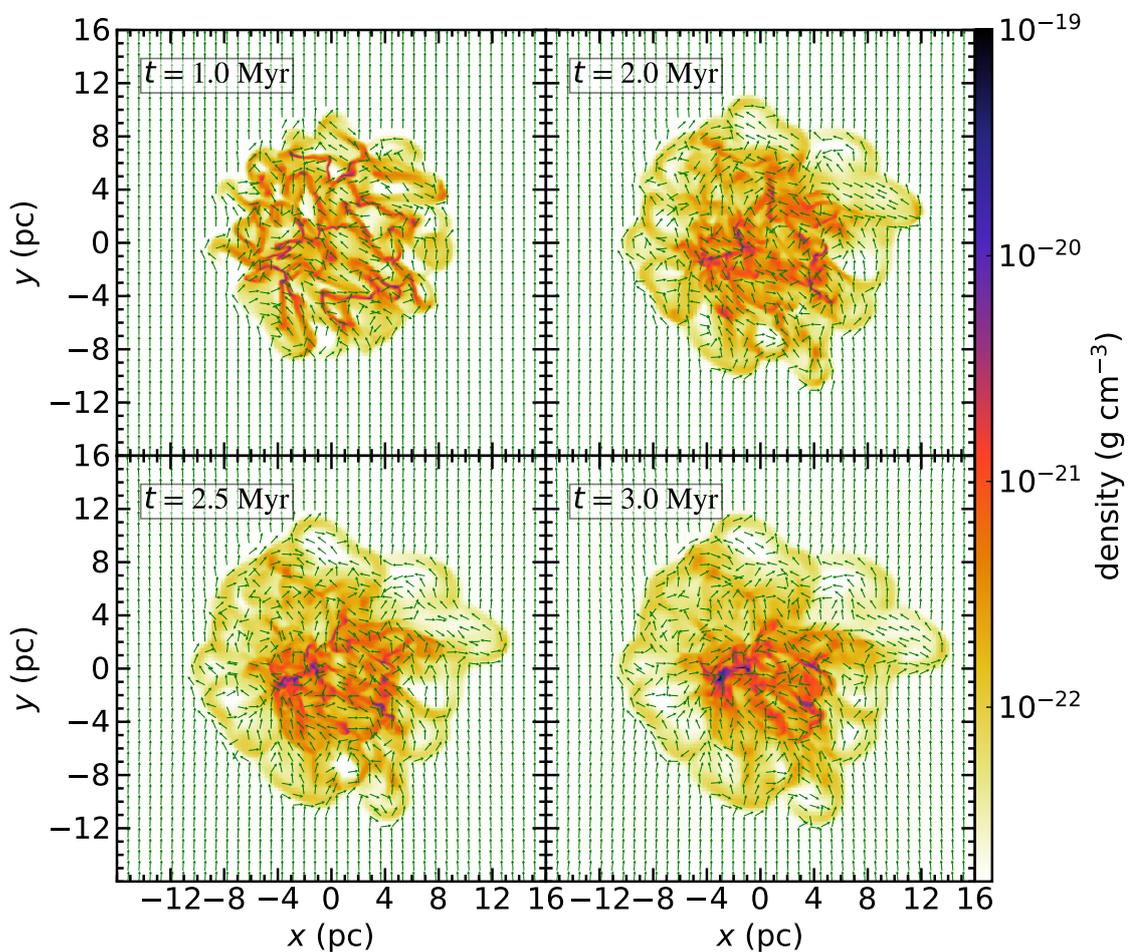
Figure A.1: Same as Figure 2.4, but for the ISweak model.

We show results of the isolated cloud models (ISweak and ISstrong models). The density slice plots at $t = 1.0$ Myr, 2.0 Myr, 2.5 Myr, and 3.0 Myr for the ISweak model ($B_0 = 0.1$ μG) are shown in Figure A.1. The initial uniform magnetic field is distorted by the turbulence. The gas density contrast is clearly seen at $t = 1.0$
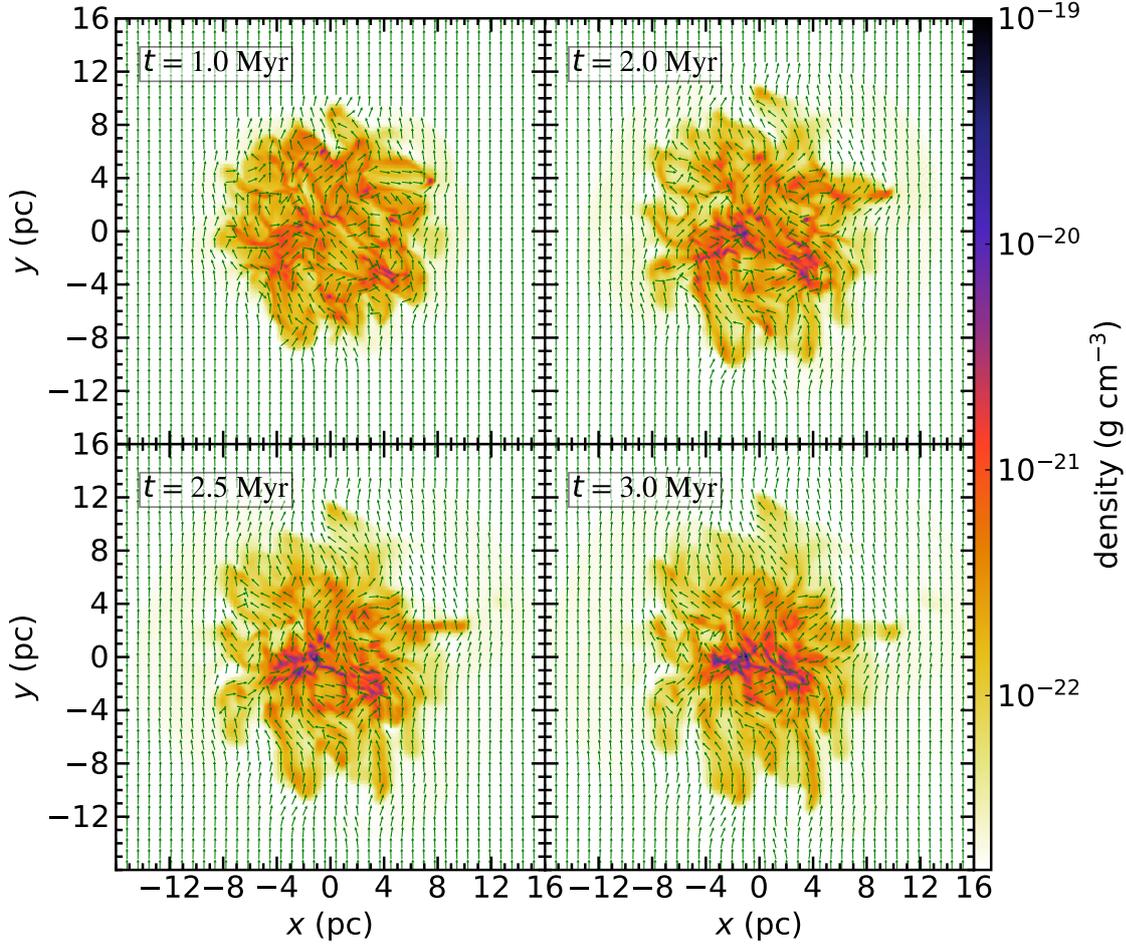
Figure A.2: Same as Figure 2.4, but for the ISstrong model.

Myr. Dense regions are formed at later epochs (t = 2.5 Myr and 3.0 Myr) due to gas motion induced by self-gravity of gas. The density slice plots at t = 1.0 Myr, 2.0 Myr, 2.5 Myr, and 3.0 Myr for the ISstrong model (B_0 = 4.0 μG) are shown in Figure A.2. Contrary to the ISweak model, the gas in the ISstrong model has less density contrast at t = 1.0 Myr, since the strong magnetic field suppresses density enhancement by the turbulence. At t = 2.0 and 2.5 Myr, more gas accumulation towards x-z plane is seen in the ISstrong model than the ISweak model. This is because the strong magnetic field induces more gas flow along the magnetic field lines than the weak magnetic field. At t = 3.0 Myr, we find the gas flow by the self-gravity towards dense gas regions in both models. We find more gas concentration near the x-z plane region at t = 3.0 Myr in the ISstrong model than the ISweak model. PDFs of the isolated clouds at t = 1.0 Myr, 2.0 Myr, 2.5 Myr, and 3.0 Myr for the ISweak and ISstrong models are shown in Figure A.3. In Figure A.3, the initial density of the isolated cloud and density threshold, ρ_{th}, for dense
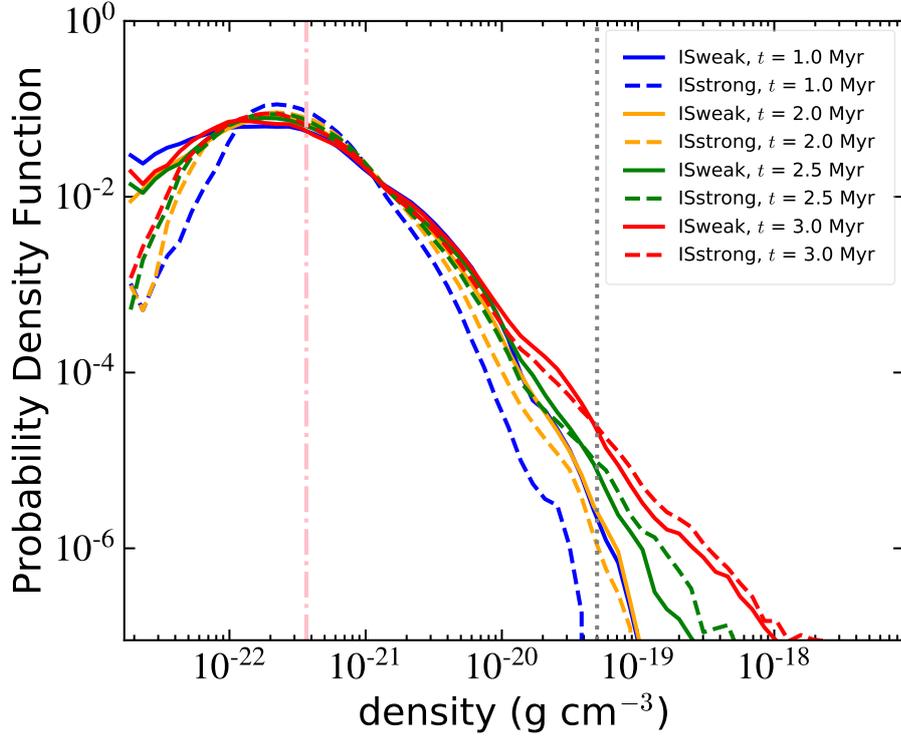
Figure A.3: Probability density functions (PDFs) of the isolated clouds at $t = 1.0$ Myr (blue lines), 2.0 Myr (orange lines), 2.5 Myr (green lines), and 3.0 Myr (red lines) for the ISweak (solid lines) and ISstrong (dashed lines) models. The vertical, dash-dotted, and dotted lines indicate the initial density of the cloud and the density threshold, ρ_{th}, for dense cores, respectively. The selection criteria for volumes used for PDFs is same as in Figure 2.3.

cores are indicated by the vertical, dash-dotted, and dotted lines, respectively. The PDFs at $t = 1.0$ Myr show higher gas density contrast in the ISweak model than the ISstrong model. The PDFs at later epochs ($t = 2.5$ Myr and 3.0 Myr) show power-law tail due to the effect of self-gravity and the formation of dense gas with a density greater than ρ_{th} in the ISweak and ISstrong models.

Appendix B

NTSI (For Chapter 2)
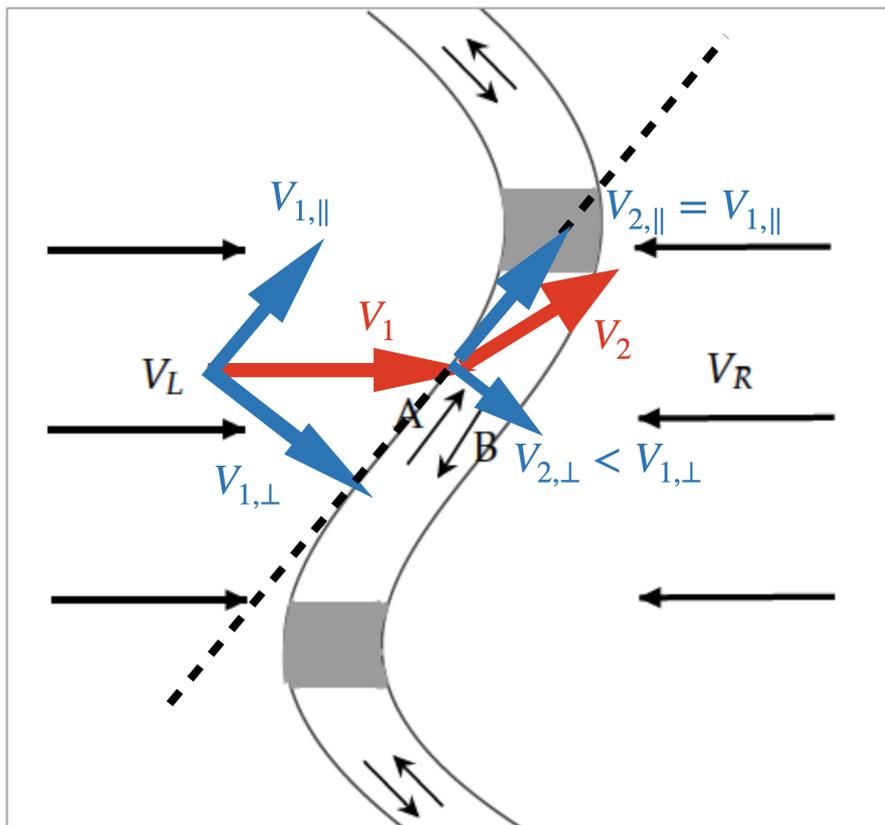
Figure B.1: Schematic view of NTSI. Details of the figure are mentioned in the text.

The nonlinear thin shell instability (NTSI) was first described by Vishniac (1994). This instability occurs in shocked layers, such as those confined between converging flows and it grows with time. Figure B.1 shows schematic view of NTSI. Thin shocked region (thin shell) is shown. This thin shell is due to high-density contrast between pre-shock and post-shock region in presence of strong cooling. If this thin shell is perturbed due to collision, gas flow inside the shock is altered. From shock condition of mass conservation, the parallel component

of post-shock velocity, $V_{2,\parallel}$, remains same and perpendicular component, $V_{2,\perp}$, decreases. Thus, the resultant post-shock velocity vector, V_2, changes direction from initial pre-shock velocity, V_1. This leads to accumulation of dense gas at the extremities of the thin shell shown by grey region. A and B vectors show the direction of gas flow in this thin shell.

In Strong B_0 models in Chapter 2, we found no clear NTSI with small scale. Magnetic field suppress small scale NTSI. This is due to combined effects of magnetic tension and magnetic pressure. Magnetic tension is strong as it inversely proportional to radius of curvature and it tries to straighten spatial shifts and suppress NTSI. Magnetic pressure also helps in suppressing NTSI as stronger magnetic pressure suppresses formation of thin shell.

Appendix C

Isolated clouds (For Chapter 3)
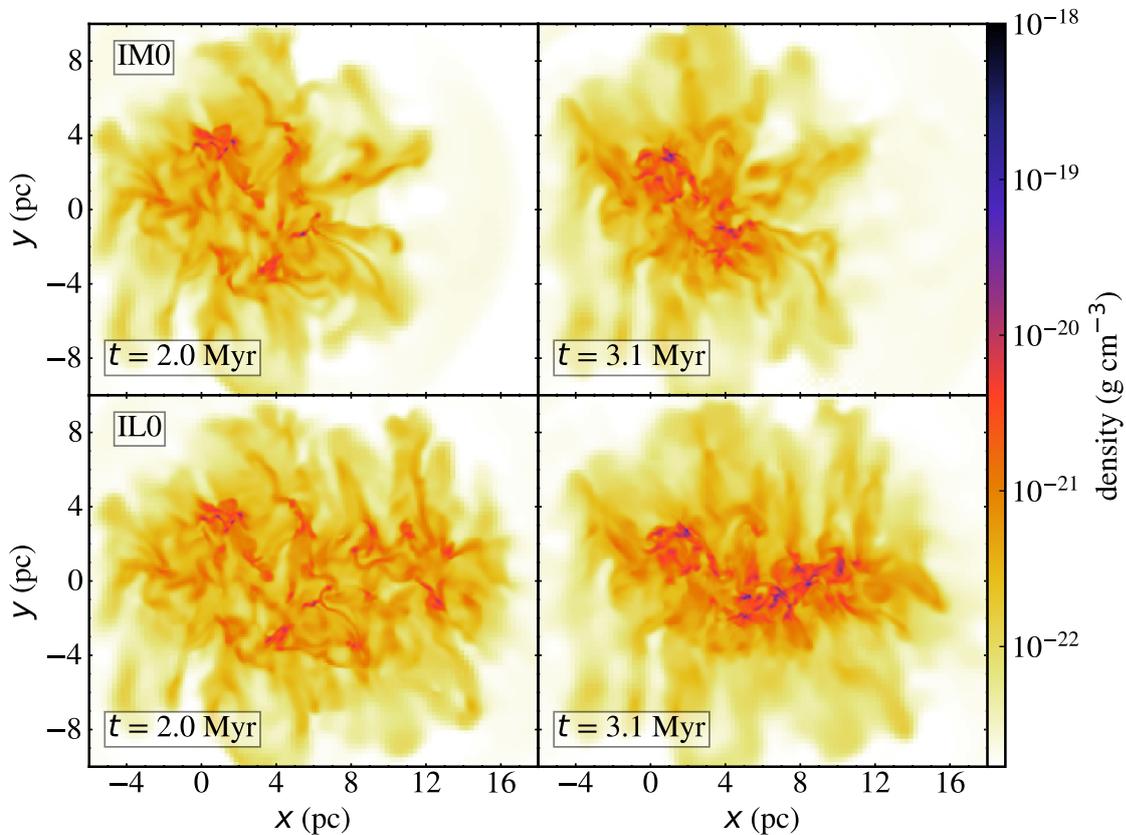
Figure C.1: Slice plots of the gas density in $z = 0$ pc at $t = 2.0$ (left panels) and 3.1 Myr (right panels) in the IM0 (top panels) and IL0 (bottom panels). The color bar shows gas density.

We show numerical results of the isolated cloud models (IM0 and IL0) and compare them with those of CCC models shown in main text.

The density slice plots at $t = 2.0$ and 3.1 Myr for IM0 (top panels) and IL0 (bottom panels) are shown in Figure C.1. This figure shows a clear difference between the dense regions in the isolated cloud models and CCC models. More dense regions are formed in CCC models than the isolated cloud models.
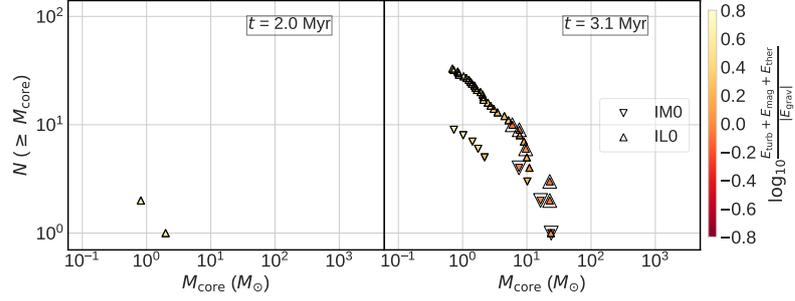
Figure C.2: Cumulative core mass distributions shown by filled down-pointing and up-pointing triangles at $t = 2.0$ (top panel) and 3.1 Myr (bottom panel) for the IM0 and IL0, respectively. The gravitationally bound cores are marked by larger, open down-pointing and up-pointing triangles for the IM0 and IL0, respectively.

We show time evolution of $M_{\text{high,tot}}$ in IM0 and IL0 in Figure 3.4. This figure shows that $M_{\text{high,tot}}$ in IL0 and IM0 increase very slowly than CCC models. By $t = 3.1$ Myr, growth of $M_{\text{high,tot}}$ is lower in the isolated cloud models than M10 and L20.

We show CMDs of both models at $t = 2.0$ and 3.1 Myr in Figure C.2. This figure shows that dense core formation occurs later than CCC models. At $t = 3.1$ Myr, there are two massive bound cores in both models and a significantly greater number of dense cores in IL0 than IM0. These numbers of massive bound cores and maximum masses of dense core in isolated cloud models are much smaller than those in M10 and L20.

Appendix D

Sink particle model (For Chapter 4)

D.1 Sink Particle Creation

For sink particle creation, it is necessary to perform a number of tests (Federrath et al., 2010). A sink particle is formed in a cell when the following criteria are met:

(a) The cell density is greater than a threshold value, ρ_{th},

(b) The cell is on the finest level of refinement.

(c) The gas within the control volume (i.e., the Jeans volume) is not within the accretion sphere of another sink particle.

(d) The gas in the control volume is converging towards the center of the control volume.

(e) The local gravitational potential minimum is within the accretion sphere.

(f) The gas within the accretion sphere is Jeans unstable for collapse.

(g) The gas within the accretion sphere is gravitationally bound.

Section D.1.1 describes the threshold density, ρ_{th}, in check (a). Section D.1.2 describes the accretion sphere. Section D.1.3 describes the Jeans instability check (f). Section D.1.4 describes the check for Bound State (g).

D.1.1 Density Threshold

The Jeans length for density ρ is

$$\lambda_J = \left(\frac{\pi c_s^2}{G\rho} \right)^{1/2}, \tag{D.1}$$

where c_s is sound speed. Since we consider magnetic field in our simulations, we use magnetic version of Jeans length, which simply is defined by using sum of thermal and magnetic pressures ($\rho c_s^2 + 0.5\rho v_a^2$) instead of thermal pressure (ρc_s^2) (Federrath and Klessen, 2012). This gives modified jeans length as

$$\lambda_{J,mag} = \left(\frac{\pi c_s^2}{G\rho} + \frac{B^2}{8G\rho^2} \right)^{1/2}, \tag{D.2}$$

where B is magnetic field strength.

We define threshold density ρ_{th} which satisfies the Truelove condition that the Jeans length must be resolved with at least four grid cells. Thus, ρ_{th} is controlled by minimum cell width Δx_{min} as

$$4\Delta x_{min} = \left(\frac{\pi c_s^2}{G\rho_{th}} + \frac{B^2}{8G\rho_{th}^2} \right)^{1/2} \tag{D.3}$$

D.1.2 Accretion sphere

Accretion sphere is a temporarily created spherical region with a radius r_{acc} ($= 2\,\Delta x_{min}$) centered on the cell. This radius is same as the accretion radius of the sink particle for the implementation of accretion.

D.1.3 Jeans Instability Check

The relation

$$\left| E_{grav} \right| > 2E_{th} + E_{mag} \tag{D.4}$$

must hold for gas within the accretion sphere for sink particle creation, where E_{grav}, E_{th}, E_{mag} are gravitational, thermal and magnetic energies, respectively. This means that the gas mass exceeds the Jeans mass in the accretion sphere. This is a modified version of the Jeans criterion, which takes into account the additional pressure provided by magnetic field.

D.1.4 Check for Bound State

For the sink particle creation, the total gas energy inside the accretion sphere must be negative,

$$E_{grav} + E_{th} + E_{kin} + E_{mag} < 0, \tag{D.5}$$

where E_{kin} is kinetic energy.

D.2 Gas Accretion

After a sink particle is created, it can gain mass by gas accretion. If a cell within r_{acc} exceeds ρ_{th}, the mass increment ΔM is calculated. If ΔM is bound to the central sink particle and the remaining gas within r_{acc}, $0.5\Delta M$ is accreted by the sink particle. The sink gets mass for a local dynamical time (the free-fall time of the accretion sphere).

To verify that ΔM is bound to the particle, the kinetic energy of ΔM is calculated in the reference frame of the particle and is compared to its gravitational binding energy. Furthermore, the radial velocity of ΔM must be negative. If ΔM

is in a region of overlapping multiple particles (which can happen due to particle motion), the gravitational binding energy of ΔM for each of these particles is calculated, and $0.5\Delta M$ is accreted to the particle to which ΔM is most strongly bound.

The accretion takes place such that mass, linear momentum, and angular momentum are conserved. The accreting gas is moved to the center of mass of the sink particle and accreting gas before the accretion step.

References

Anathpindika, S. V. (2010). "Collision between dissimilar clouds: stability of the bow-shock, and the formation of pre-stellar cores". In: *MNRAS* 405, pp. 1431–1443. DOI: `10.1111/j.1365-2966.2010.16541.x`.

Beck, Rainer (2015). "Magnetic fields in spiral galaxies". In: *A&A Rev.* 24, 4, p. 4. DOI: `10.1007/s00159-015-0084-4`.

Bergin, E. A. and M. Tafalla (2007). "Cold Dark Clouds: The Initial Conditions for Star Formation". In: *ARA&A* 45, pp. 339–396. DOI: `10.1146/annurev.astro.45.071206.100404`.

Bondi, H. (1952). "On spherically symmetrical accretion". In: *MNRAS* 112, p. 195. DOI: `10.1093/mnras/112.2.195`.

Brummel-Smith, Corey et al. (2019). "ENZO: An Adaptive Mesh Refinement Code for Astrophysics (Version 2.6)". In: *The Journal of Open Source Software* 4.42, 1636, p. 1636. DOI: `10.21105/joss.01636`.

Bryan, Greg L. et al. (2014). "ENZO: An Adaptive Mesh Refinement Code for Astrophysics". In: *ApJS* 211, 19, p. 19. DOI: `10.1088/0067-0049/211/2/19`.

Chen, Che-Yu and Eve C. Ostriker (2014). "Formation of Magnetized Prestellar Cores with Ambipolar Diffusion and Turbulence". In: *ApJ* 785, 69, p. 69. DOI: `10.1088/0004-637X/785/1/69`.

— (2015). "Anisotropic Formation of Magnetized Cores in Turbulent Clouds". In: *ApJ* 810, 126, p. 126. DOI: `10.1088/0004-637X/810/2/126`.

— (2018). "Geometry, Kinematics, and Magnetization of Simulated Prestellar Cores". In: *ApJ* 865.1, 34, p. 34. DOI: `10.3847/1538-4357/aad905`.

Crutcher, R. M. et al. (2010). "Magnetic Fields in Interstellar Clouds from Zeeman Observations: Inference of Total Field Strengths by Bayesian Analysis". In: *ApJ* 725, pp. 466–479. DOI: `10.1088/0004-637X/725/1/466`.

Dedner, A. et al. (2002). "Hyperbolic Divergence Cleaning for the MHD Equations". In: *Journal of Computational Physics* 175, pp. 645–673. DOI: `10.1006/jcph.2001.6961`.

Dewangan, L. K. et al. (2016). "A Multi-wavelength Study of Star Formation Activity in the S235 Complex". In: *ApJ* 819, 66, p. 66. DOI: `10.3847/0004-637X/819/1/66`.

Dobbs, C. L., J. E. Pringle, and A. Duarte-Cabral (2015). "The frequency and nature of 'cloud-cloud collisions' in galaxies". In: *MNRAS* 446.4, pp. 3608–3620. DOI: `10.1093/mnras/stu2319`.

Dobbs, C. L. and J. Wurster (2021). "The properties of clusters, and the orientation of magnetic fields relative to filaments, in magnetohydrodynamic simulations

of colliding clouds". In: *MNRAS* 502.2, pp. 2285–2295. DOI: `10.1093/mnras/stab150`.

Elmegreen, B. G. (1998). "Observations and Theory of Dynamical Triggers for Star Formation". In: *Origins*. Ed. by Charles E. Woodward, J. Michael Shull, and Jr. Thronson Harley A. Vol. 148. Astronomical Society of the Pacific Conference Series, p. 150.

Enokiya, Rei, Kazufumi Torii, and Yasuo Fukui (2021). "Cloud-cloud collisions in the common foot point of molecular loops 1 and 2 in the Galactic Center". In: *PASJ* 73, S75–S90. DOI: `10.1093/pasj/psz119`.

Federrath, C. et al. (2010). "Modeling Collapse and Accretion in Turbulent Gas Clouds: Implementation and Comparison of Sink Particles in AMR and SPH". In: *ApJ* 713, pp. 269–290. DOI: `10.1088/0004-637X/713/1/269`.

Federrath, Christoph and Ralf S. Klessen (2012). "The Star Formation Rate of Turbulent Magnetized Clouds: Comparing Theory, Simulations, and Observations". In: *ApJ* 761.2, 156, p. 156. DOI: `10.1088/0004-637X/761/2/156`.

Federrath, Christoph et al. (2011). "A New Jeans Resolution Criterion for (M)HD Simulations of Self-gravitating Gas: Application to Magnetic Field Amplification by Gravity-driven Turbulence". In: *ApJ* 731.1, 62, p. 62. DOI: `10.1088/0004-637X/731/1/62`.

Ferlandf, G. J. et al. (1998). "CLOUDY 90: Numerical Simulation of Plasmas and Their Spectra". In: *PASP* 110, pp. 761–778. DOI: `10.1086/316190`.

Fujimoto, Y., E. J. Tasker, and A. Habe (2014). "Environmental dependence of star formation induced by cloud collisions in a barred galaxy." In: *MNRAS* 445, pp. L65–L69. DOI: `10.1093/mnrasl/slu138`.

Fujimoto, Yusuke et al. (2020). "Fast cloud-cloud collisions in a strongly barred galaxy: suppression of massive star formation". In: *MNRAS* 494.2, pp. 2131–2146. DOI: `10.1093/mnras/staa840`.

Fujita, Shinji et al. (2021). "High-mass star formation in Orion possibly triggered by cloud-cloud collision. III. NGC 2068 and NGC 2071". In: *PASJ* 73, S273–S284. DOI: `10.1093/pasj/psaa005`.

Fukui, Y. et al. (2018a). "A New Look at the Molecular Gas in M42 and M43: Possible Evidence for Cloud-Cloud Collision that Triggered Formation of the OB Stars in the Orion Nebula Cluster". In: *ApJ* 859, 166, p. 166. DOI: `10.3847/1538-4357/aac217`.

Fukui, Yasuo et al. (2018b). "Molecular clouds toward three Spitzer bubbles S116, S117, and S118: Evidence for a cloud-cloud collision which formed the three H II regions and a 10 pc scale molecular cavity". In: *PASJ* 70, S46, S46. DOI: `10.1093/pasj/psy005`.

Fukui, Yasuo et al. (2021). "Cloud-cloud collisions and triggered star formation". In: *PASJ* 73, S1–S34. DOI: `10.1093/pasj/psaa103`.

Furukawa, N. et al. (2009). "Molecular Clouds Toward RCW49 and Westerlund 2: Evidence for Cluster Formation Triggered by Cloud-Cloud Collision". In: *ApJ* 696, pp. L115–L119. DOI: `10.1088/0004-637X/696/2/L115`.

Gilden, D. L. (1984). "Clump collisions in molecular clouds - Gravitational instability and coalescence". In: *ApJ* 279, pp. 335–349. DOI: 10.1086/161894.

Habe, Asao and Kanji Ohta (1992). "Gravitational Instability Induced by a Cloud-Cloud Collision: The Case of Head-on Collisions between Clouds with Different Sizes and Densities". In: *PASJ* 44, pp. 203–226.

Hasegawa, Tetsuo et al. (1994). "A Large-Scale Cloud Collision in the Galactic Center Molecular Cloud Near Sagittarius B2". In: *ApJ* 429, p. L77. DOI: 10.1086/187417.

Heitsch, Fabian et al. (2007). "Magnetized Nonlinear Thin-Shell Instability: Numerical Studies in Two Dimensions". In: *ApJ* 665, pp. 445–456. DOI: 10.1086/519513.

Heyer, M. et al. (2009). "Re-Examining Larson's Scaling Relationships in Galactic Molecular Clouds". In: *ApJ* 699, pp. 1092–1103. DOI: 10.1088/0004-637X/699/2/1092.

Ikeda, Norio, Kazuyoshi Sunada, and Yoshimi Kitamura (2007). "A Survey of Dense Cores in the Orion A Cloud". In: *ApJ* 665.2, pp. 1194–1219. DOI: 10.1086/519484.

Inoue, Tsuyoshi and Yasuo Fukui (2013). "Formation of Massive Molecular Cloud Cores by Cloud-Cloud Collision". In: *ApJ* 774, L31, p. L31. DOI: 10.1088/2041-8205/774/2/L31.

Inoue, Tsuyoshi and Shu-ichiro Inutsuka (2012). "Formation of Turbulent and Magnetized Molecular Clouds via Accretion Flows of H I Clouds". In: *ApJ* 759.1, 35, p. 35. DOI: 10.1088/0004-637X/759/1/35.

Inoue, Tsuyoshi, Ryo Yamazaki, and Shu ichiro Inutsuka (2009). "Turbulence and magnetic field amplification in supernova remnants: Interactions between a strong shock wave and multiphase interstellar medium". In: *ApJ* 695.2, pp. 825–833. DOI: 10.1088/0004-637x/695/2/825.

Inoue, Tsuyoshi et al. (2018). "The formation of massive molecular filaments and massive stars triggered by a magnetohydrodynamic shock wave". In: *PASJ* 70, S53, S53. DOI: 10.1093/pasj/psx089.

Kritsuk, A. G., M. L. Norman, and R. Wagner (2011). "On the Density Distribution in Star-forming Interstellar Clouds". In: *ApJ* 727, L20, p. L20. DOI: 10.1088/2041-8205/727/1/L20.

Lada, Charles J. (1999). "The Formation of Low Mass Stars: An Observational Overview". In: *The Origin of Stars and Planetary Systems*. Ed. by Charles J. Lada and Nikolaos D. Kylafis. Vol. 540. NATO Advanced Study Institute (ASI) Series C, p. 143.

Larson, R. B. (1981). "Turbulence and star formation in molecular clouds." In: *MNRAS* 194, pp. 809–826. DOI: 10.1093/mnras/194.4.809.

Machacek, Marie E., Greg L. Bryan, and Tom Abel (2001). "Simulations of Pregalactic Structure Formation with Radiative Feedback". In: *ApJ* 548.2, pp. 509–521. DOI: 10.1086/319014.

Maeda, Fumiya et al. (2021). "Connection among environment, cloud-cloud collision speed, and star formation activity in the strongly barred galaxy NGC 1300". In: *MNRAS* 502.2, pp. 2238–2250. DOI: 10.1093/mnras/stab130.

Mangilli, A. et al. (2019). "The geometry of the magnetic field in the central molecular zone measured by PILOT". In: *A&A* 630, A74, A74. DOI: 10.1051/0004-6361/201935072.

McKee, C. F. and J. C. Tan (2002). "Massive star formation in 100,000 years from turbulent and pressurized molecular clouds". In: *Nature* 416, pp. 59–61. DOI: 10.1038/416059a.

McKee, Christopher F. and Jonathan C. Tan (2003). "The Formation of Massive Stars from Turbulent Cores". In: *ApJ* 585.2, pp. 850–871. DOI: 10.1086/346149.

McKee, Christopher F. and Ellen G. Zweibel (1992). "On the Virial Theorem for Turbulent Molecular Clouds". In: *ApJ* 399, p. 551. DOI: 10.1086/171946.

Mills, E. A. C. (2017). "The Milky Way's Central Molecular Zone". In: *arXiv e-prints*, arXiv:1705.05332, arXiv:1705.05332.

Mizuno, Yosuke et al. (2010). "Magnetic-field amplification by turbulence in a relativistic shock propagating through an inhomogeneous medium". In: *ApJ* 726.2, p. 62. DOI: 10.1088/0004-637x/726/2/62.

Momose, Rieko et al. (2010). "Star Formation Efficiency in the Barred Spiral Galaxy NGC 4303". In: *ApJ* 721.1, pp. 383–394. DOI: 10.1088/0004-637X/721/1/383.

Murray, N. (2011). "Star Formation Efficiencies and Lifetimes of Giant Molecular Clouds in the Milky Way". In: *ApJ* 729, 133, p. 133. DOI: 10.1088/0004-637X/729/2/133.

Nagai, Tomoya, Shu-ichiro Inutsuka, and Shoken M. Miyama (1998). "An Origin of Filamentary Structure in Molecular Clouds". In: *ApJ* 506.1, pp. 306–322. DOI: 10.1086/306249.

Nakano, T. and T. Nakamura (1978). "Gravitational Instability of Magnetized Gaseous Disks 6". In: *PASJ* 30, pp. 671–680.

Offner, S. S. R. et al. (2014). "The Origin and Universality of the Stellar Initial Mass Function". In: *Protostars and Planets VI*. DOI: 10.2458/azu_uapress_9780816531240-ch003.

Ohama, A. et al. (2010). "Temperature and Density Distribution in the Molecular Gas Toward Westerlund 2: Further Evidence for Physical Association". In: *ApJ* 709, pp. 975–982. DOI: 10.1088/0004-637X/709/2/975.

Oort, J. H. (1954). "Outline of a theory on the origin and acceleration of interstellar clouds and O associations". In: *Bull. Astron. Inst. Netherlands* 12, p. 177.

Padoan, P. and Å. Nordlund (2011). "The Star Formation Rate of Supersonic Magnetohydrodynamic Turbulence". In: *ApJ* 730, 40, p. 40. DOI: 10.1088/0004-637X/730/1/40.

Padoan, Paolo and Åke Nordlund (2002). "The Stellar Initial Mass Function from Turbulent Fragmentation". In: *ApJ* 576.2, pp. 870–879. DOI: 10.1086/341790.

Passot, Thierry and Enrique Vázquez-Semadeni (1998). "Density probability distribution in one-dimensional polytropic gas dynamics". In: *Phys. Rev. E* 58.4, pp. 4501–4510. DOI: 10.1103/PhysRevE.58.4501.

Sakre, Nirmit et al. (2021). "Massive core/star formation triggered by cloud-cloud collision: Effect of magnetic field". In: *PASJ* 73, S385–S404. DOI: 10.1093/pasj/psaa059.

Salpeter, Edwin E. (1955). "The Luminosity Function and Stellar Evolution." In: *ApJ* 121, p. 161. DOI: 10.1086/145971.

Shima, K. et al. (2018). "The effect of photoionizing feedback on star formation in isolated and colliding clouds". In: *PASJ* 70, S54, S54. DOI: 10.1093/pasj/psx124.

Shu, F. H. (1977). "Self-similar collapse of isothermal spheres and star formation." In: *ApJ* 214, pp. 488–497. DOI: 10.1086/155274.

Slavin, J. A. et al. (1984). "Planetary Mach cones - Theory and observation". In: *Journal of Geophysical Research* 89, pp. 2708–2714. DOI: 10.1029/JA089iA05p02708.

Smith, J. (1980). "Cloud-cloud collisions in the interstellar medium". In: *ApJ* 238, pp. 842–852. DOI: 10.1086/158045.

Spitzer, Lyman (1978). *Physical processes in the interstellar medium*. DOI: 10.1002/9783527617722.

Stone, M. E. (1970). "Collisions Between H i Clouds. I. One-Dimensional Model". In: *ApJ* 159, p. 277. DOI: 10.1086/150309.

Takahira, Ken, Elizabeth J. Tasker, and Asao Habe (2014). "Do Cloud-Cloud Collisions Trigger High-mass Star Formation? I. Small Cloud Collisions". In: *ApJ* 792, 63, p. 63. DOI: 10.1088/0004-637X/792/1/63.

Takahira, Ken et al. (2018). "Formation of massive, dense cores by cloud-cloud collisions". In: *PASJ* 70, S58, S58. DOI: 10.1093/pasj/psy011.

Tanaka, Kei E. I., Jonathan C. Tan, and Yichen Zhang (2017). "The Impact of Feedback During Massive Star Formation by Core Accretion". In: *ApJ* 835.1, 32, p. 32. DOI: 10.3847/1538-4357/835/1/32.

Tasker, E. J. and G. L. Bryan (2008). "The Effect of the Interstellar Model on Star Formation Properties in Galactic Disks". In: *ApJ* 673, pp. 810–831. DOI: 10.1086/523889.

Tasker, Elizabeth J. and Jonathan C. Tan (2009). "Star Formation in Disk Galaxies. I. Formation and Evolution of Giant Molecular Clouds via Gravitational Instability and Cloud Collisions". In: *ApJ* 700, pp. 358–375. DOI: 10.1088/0004-637X/700/1/358.

Tomisaka, K. and S. Ikeuchi (1983). "Gravitational instability of isothermal gas layers - Effect of curvature and magnetic field". In: *PASJ* 35.2, pp. 187–208.

Tomisaka, Kohji (1998). "Collapse-Driven Outflow in Star-Forming Molecular Cores". In: *ApJ* 502.2, pp. L163–L167. DOI: 10.1086/311504.

— (2014). "Magnetohydrostatic Equilibrium Structure and Mass of Filamentary Isothermal Cloud Threaded by Lateral Magnetic Field". In: *ApJ* 785.1, 24, p. 24. DOI: 10.1088/0004-637X/785/1/24.

Torii, K. et al. (2017). "Triggered O Star Formation in M20 via Cloud-Cloud Collision: Comparisons between High-resolution CO Observations and Simulations". In: *ApJ* 835.2, 142, p. 142. DOI: `10.3847/1538-4357/835/2/142`.

Turk, M. J. et al. (2011). "yt: A Multi-code Analysis Toolkit for Astrophysical Simulation Data". In: *ApJS* 192, 9, p. 9. DOI: `10.1088/0067-0049/192/1/9`.

Uehara, Kenta et al. (2019). "Molecular Cloud Cores in the Galactic Center 50 km s^{-1} Molecular Cloud". In: *ApJ* 872.2, 121, p. 121. DOI: `10.3847/1538-4357/aafee7`.

Vazquez-Semadeni, Enrique (1994). "Hierarchical Structure in Nearly Pressureless Flows as a Consequence of Self-similar Statistics". In: *ApJ* 423, p. 681. DOI: `10.1086/173847`.

Vishniac, E. T. (1994). "Nonlinear instabilities in shock-bounded slabs". In: *ApJ* 428, pp. 186–208. DOI: `10.1086/174231`.

Wise, John H. and Tom Abel (2011). "ENZO+MORAY: radiation hydrodynamics adaptive mesh refinement simulations with adaptive ray tracing". In: *MNRAS* 414.4, pp. 3458–3491. DOI: `10.1111/j.1365-2966.2011.18646.x`.

Wolfire, M. G. and J. P. Cassinelli (1987). "Conditions for the formation of massive stars". In: *ApJ* 319, pp. 850–867. DOI: `10.1086/165503`.

Wu, Benjamin et al. (2017a). "GMC Collisions as Triggers of Star Formation. II. 3D Turbulent, Magnetized Simulations". In: *ApJ* 835, 137, p. 137. DOI: `10.3847/1538-4357/835/2/137`.

Wu, Benjamin et al. (2017b). "GMC Collisions as Triggers of Star Formation. III. Density and Magnetically Regulated Star Formation". In: *ApJ* 841, 88, p. 88. DOI: `10.3847/1538-4357/aa6ffa`.

Wu, Benjamin et al. (2020). "GMC Collisions as Triggers of Star Formation. VII. The Effect of Magnetic Field Strength on Star Formation". In: *ApJ* 891.2, 168, p. 168. DOI: `10.3847/1538-4357/ab77b5`.

Zinnecker, Hans and Harold W. Yorke (2007). "Toward Understanding Massive Star Formation". In: *ARA&A* 45.1, pp. 481–563. DOI: `10.1146/annurev.astro.44.051905.092549`.